

Spring 2005

Development of a novel microreactor for improved chemical reaction conversion

Yu Liang
Louisiana Tech University

Follow this and additional works at: <https://digitalcommons.latech.edu/dissertations>

 Part of the [Chemical Engineering Commons](#), and the [Mechanical Engineering Commons](#)

Recommended Citation

Liang, Yu, "" (2005). *Dissertation*. 602.
<https://digitalcommons.latech.edu/dissertations/602>

This Dissertation is brought to you for free and open access by the Graduate School at Louisiana Tech Digital Commons. It has been accepted for inclusion in Doctoral Dissertations by an authorized administrator of Louisiana Tech Digital Commons. For more information, please contact digitalcommons@latech.edu.

DEVELOPMENT OF A NOVEL MICROREACTOR FOR IMPROVED
CHEMICAL REACTION CONVERSION

by

Yu Liang, M.S.

A Dissertation Presented in Partial Fulfillment
of the Requirements for the Degree of
Ph.D in Engineering

COLLEGE OF ENGINEERING AND SCIENCE
LOUISIANA TECH UNIVERSITY

May 2005

UMI Number: 3170183

INFORMATION TO USERS

The quality of this reproduction is dependent upon the quality of the copy submitted. Broken or indistinct print, colored or poor quality illustrations and photographs, print bleed-through, substandard margins, and improper alignment can adversely affect reproduction.

In the unlikely event that the author did not send a complete manuscript and there are missing pages, these will be noted. Also, if unauthorized copyright material had to be removed, a note will indicate the deletion.

UMI[®]

UMI Microform 3170183

Copyright 2005 by ProQuest Information and Learning Company.

All rights reserved. This microform edition is protected against unauthorized copying under Title 17, United States Code.

ProQuest Information and Learning Company
300 North Zeeb Road
P.O. Box 1346
Ann Arbor, MI 48106-1346

LOUISIANA TECH UNIVERSITY

THE GRADUATE SCHOOL

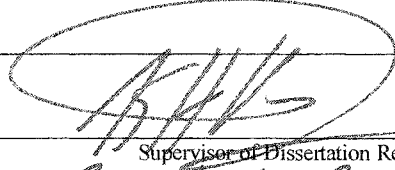
May 21st, 2005

Date

We hereby recommend that the dissertation prepared under our supervision
by LIANG, YU

entitled DEVELOPMENT OF A NOVEL MICROREACTOR FOR IMPROVED
CHEMICAL REACTION CONVERSION

be accepted in partial fulfillment of the requirements for the Degree of
Ph.D in Engineering



Supervisor of Dissertation Research

Ray T. Worley

Head of Department

Ph.D. in Engineering

Department

Recommendation concurred in:

Kaya Hassan

Sanjiv

Deborah Krick

Y. Su

Advisory Committee

Approved:

Pada Ramachandran

Director of Graduate Studies

Steve Nepper

Dean of the College

Approved:

Terry M. McCarthy

Dean of the Graduate School

ABSTRACT

Microreactors have been widely studied over the past two decades for different chemical reactions, to develop new analytical capabilities, and to obtain high mixing performance in the reactors. The main objectives of this work are to investigate the effect of different microchannel structures on the fluid properties and mixing behavior in microreactors, and to design, fabricate, and test a novel microreactor for higher conversion in a chemical reaction. The development of this novel microreactor is intended to provide a valuable guideline in achieving enhanced chemical mixing and to make available a solid research base for optimization of the yield of chemical reactions in microchannels.

Most of the current microreactors are designed with straight or zigzag microchannels [3]. In this research work, we have developed a novel omega-shaped microreactor, which yields higher conversion through mixing enhancement. It offers the advantages of reducing the mixing distance of the reactant species, stretching and folding the flow, generating vorticities which overcome any uneven distribution of the reactant, and consequently improve conversion efficiency in a typical reaction.

Fluid properties of the omega channel reactor have been investigated by means of computational fluid dynamic (CFD) simulation to validate the criteria of the omega

channel design. A stochastic Markov chain process has been used to study fluid flow, and to describe the residence time distribution functions for the microreactors considered in this work.

Based on theoretical predictions, three kinds of microreactors with straight, zigzag, and omega-shaped microchannels, have been designed and fabricated using optical lithography and dry etching methods. To compare the efficacy of the microreactors, Fischer-Tropsch reactions have been carried out using sol-gel encapsulated iron and cobalt catalysts in the microchannels. The experimental results show that the conversion efficiency for an omega-shaped reactor is 17 % greater than that for a conventional straight channel microreactor, and is 12 % greater than that for the zigzag-shaped channel microreactor. The data is consistent with the CFD simulation and stochastic modeling results.

The novel omega-shaped microreactor offers a better alternative to straight and zigzag channel microreactors and provides a better micro-fluidic system for microscale total analysis applications.

APPROVAL FOR SCHOLARLY DISSEMINATION

The author grants to the Prescott Memorial Library of Louisiana Tech University the right to reproduce, by appropriate methods, upon request, any or all portions of this Dissertation. It is understood that "proper request" consists of the agreement, on the part of the requesting party, that said reproduction is for his personal use and that subsequent reproduction will not occur without written approval of the author of this Dissertation. Further, any portions of the Dissertation used in books, papers, and other works must be appropriately referenced to this Dissertation.

Finally, the author of this Dissertation reserves the right to publish freely, in the literature, at any time, any or all portions of this Dissertation.

Author Liung Tu

Date May 17th, 2005

DEDICATION

To my parents, my husband, and my son, Kevin.

TABLE OF CONTENTS

	Page
ABSTRACT.....	iii
DEDICATION.....	v
LIST OF TABLES.....	ix
LIST OF FIGURES.....	x
ACKNOWLEDGMENTS.....	xiii
CHAPTER 1 INTRODUCTION.....	1
1.1 Microreactor Research Background and Literature Review.....	1
1.2 Objectives.....	5
1.3 Microreactor Application Reactions.....	7
1.3.1 Hydrogenation and Dehydrogenation of Cyclohexence.....	8
1.3.2 Preferential Oxidation for CO Ameliorationin Hydrogen Fuel Cell Feeds.....	9
1.3.3 Fischer-Tropsch Synthesis.....	10
1.4 Fabrication Methods.....	11
1.4.1 Optical Lithography.....	11
1.4.2 Electron Beam Lithography.....	12
1.4.3 Dry Etching Process.....	15
CHAPTER 2 THEORETICAL CONSIDERATION.....	18
2.1 Reaction Background.....	18
2.2 Fluid Dynamic Background.....	18
2.2.1 Flow Regimes.....	19
2.2.2 Flows in Microscale.....	20

2.3 Governing Equations for Fluid Motion.....	23
2.4 Derivation of Flow Rate in Microchannels.....	26
2.4.1 Flow in a Straight Channel.....	27
2.4.2 Flow in a Zigzag Channel.....	28
2.4.3 Flow in a Omega Channel.....	29
2.4.4 Mixing of Fluids.....	32
CHAPTER 3 FLUIDIC SIMULATIONS.....	34
3.1 Introduction to the Simulation Tool.....	36
3.2 Simulation of Fluid Flow in Microreactors.....	38
3.3 Mixing of Fluids.....	45
3.3.1 Flow Vorticity.....	46
3.3.2 Unsymmetry and Recirculation of the Flows.....	48
3.3.3 Discussion of Results.....	51
CHAPTER 4 STOCHASTIC MODELING.....	53
4.1 Markov Chain Approach.....	53
4.2 Model Formulation and Probability Transition Matrix.....	56
4.3 Cumulative Probability Computation.....	61
4.4 Mean and Variance of Time Until Exit.....	62
4.5 Markov Chain Simulation Results.....	63
CHAPTER 5 MICROREACTOR FABRICATION, CATALYST PREPARATION, AND REACTION TESTING SYSTEM.....	68
5.1 Fabrication Process.....	68
5.1.1 Photolithography.....	68
5.1.2 Etching Processes.....	76
5.2 Catalyst Preparation.....	80
5.3 Bonding.....	84
5.4 Testing System.....	86

CHAPTER 6 RESULTS AND DISCUSSION.....	88
6.1 Catalyst in Syn-Gas Reaction.....	88
6.2 Catalyst and Conversion Study in Syn-Gas Conversion.....	91
6.3 Comparison with Modeling Results.....	99
CHAPTER 7 CONCLUSION AND FUTURE WORK.....	106
7.1 Conclusion.....	106
7.2 Future Work.....	107
APPENDIX A.....	109
APPENDIX B.....	115
APPENDIX C.....	124
APPENDIX D.....	134
REFERENCES.....	147

LIST OF TABLES

Table	Page
Table 1. 1 The range and the application of the optical lithography.....	12
Table 4.1 Parameters Used in the Simulation of Results.....	64
Table 4. 2 Mean and variance of time till exit for different compartments with 3 sets of microreactors.....	66
Table 5. 1 Sol-gel solution ratio.....	81
Table 5. 2 Sol-gel precursors and ion impregnation.....	82
Table 5. 3 Mechanical Properties of Fluoroelastomer.....	86
Table 6. 1 Baseline reaction partial pressure of CO.....	94
Table 6. 2 Real reaction partial pressure of CO with 12% Fe +12% Co catalyst.....	94
Table 6. 3 Conversion of syn-gas to higher alkanes with 12% Fe +12% Co catalyst.....	94
Table 6. 4 Baseline reaction partial pressure of CO.....	96
Table 6. 5 Real reaction partial pressure of CO with an intended 12% Fe +12% Co catalyst loading.....	97
Table 6. 6 Conversion of syn-gas to higher alkanes with an intended 12% Fe +12% Co catalyst loading.....	97

LIST OF FIGURES

Figure	Page
Figure1.1 Microreactors used for chemical study.....	5
Figure1.2 Schematic drawing of electron beam projection system.....	13
Figure1.3 Electron scattering in electron beam resist exposure.....	15
Figure1.4 Schematic of DRIE principle.....	17
Figure 2.1 Knudsen Number and the Flow Regimes.....	21
Figure 2. 2 Omega channel.....	30
Figure 2.3 Mean residence time of reactor.....	33
Figure 3. 1 2-D Top View Velocity contour of the straight channel reactor.....	39
Figure 3. 2 Velocity extracted at $x=450\mu\text{m}$ from the straight channel (a)Velocity_x across channel width; (b)Velocity_y across channel width.....	39
Figure 3.3 2-D Top View Velocity contour of the zigzag channel reactor.....	40
Figure 3. 4 Velocity extracted at $x=450\mu\text{m}$ from the zigzag channel. (a)Velocity_x across the channel width; (b)Velocity_y across the channel width.....	40
Figure 3. 5 2-D top view velocity contour of the omega channel reactor.....	41
Figure 3. 6 Flow regions of the omega channel.....	42
Figure 3. 7 Velocity extracted at $x=340\mu\text{m}$ from the omega channel (a)Velocity-x of maximum velocity region (b) Velocity-y of maximum velocity region.....	42
Figure 3. 8 Velocity extracted at $x=340\mu\text{m}$ from the omega channel. (a) Velocity-x of Minimum velocity region of omega channel (b) Velocity-y of Minimum velocity region of omega channel.....	43
Figure 3. 9 Velocity in X direction for 3 sets of channels.....	43

Figure 3. 10 2-D Cross-sectional view of velocities magnitude in Y direction for 3 sets of channels (a) Straight channel reactor (b) Zigzag channel reactor (c) Omega channel reactor.....	44
Figure 3.11 2-D Cross-sectional view of vorticities of 3 set of reactors (a) Straight channel reactor (b) Zigzag channel reactor (c) Omega channel reactor.....	47
Figure 3.12 Flow in omega channel at the Reynolds number=1.27 (a) Velocity distribution (b) Pressure distribution across omega channel entrance.....	49
Figure 3.13 Flow in omega channel the Reynolds number=70 (a) Velocity distribution (b) Pressure distribution across omega channel entrance.....	49
Figure 3.14 Flow in omega channel the Reynolds number>>100 (a) Velocity distribution (b) Pressure distribution across omega channel entrance.....	50
Figure 3.15 Flow in mega channel (a) Symmetrical flow (b) Unsymmetrical recirculation.....	51
Figure 4. 1 (a) Velocity contour for compartment 1x1 omega channel. (b) Schematic diagram of all states and transitions between states for the Markov chain for compartment 1x1 omega Channel.....	58
Figure 4. 2 Cumulative probability of a molecule exiting the three microreactors with compartment 1x1.....	65
Figure 4. 3 Residence time sistribution of the three microreactors with compartment 1x1.....	65
Figure 5. 1 Pattern for Ω shaped channel microreactor.....	69
Figure 5. 2 Parameter of photoresist coating.....	71
Figure 5. 3 Aligners used in photolithography process.....	73
Figure 5. 4 SEM photos (a) cross-section of zigzag channels (b) straight channels (c) zigzag channels side view (d) omega channels (e) microreactor inlet via.....	79
Figure 5. 5 Microreactor before and after dicing.....	79
Figure 5. 6 Schematic drawing of metal reduction apparatus.....	84
Figure 5. 7 Anode bonding.....	85
Figure 5. 8 Heating Block for System Setup.....	86
Figure 5.9 Microreaction setup system.....	87
Figure 6. 1 SEM picture of sol-gel coated omega channel.....	89

Figure 6. 2 Energy dispersive X-ray analysis of an intended composition of 12% Fe+12% Co catalyst.....	90
Figure 6. 3 EDX fast map on density of catalyst (a) Fe density from EDX fast map (b) Co density from EDX fast map (c) 3D views of metal density.....	91
Figure 6. 4 Conversion of straight, zigzag and omega microreactors with different reactant gas ratios at H ₂ /CO flow rate of 0.6/0.4. 0.6/0.3 and 0.6/0.2 sccm.....	95
Figure 6. 5 Conversion of straight, zigzag and omega microreactors with different reactant gas ratios at H ₂ /CO flow rate of 0.3/0.2. 0.2/0.1 and 0.3/0.1 sccm.....	97
Figure 6. 6 Velocity contour for compartments 1x3.....	100
Figure 6. 7 Cumulative probability of a molecule exiting the three microreactors for compartments 1x3.....	100
Figure 6. 8 Velocity contour for compartments 2x2.....	101
Figure 6. 9 Cumulative probability of a molecule exiting the three microreactors for compartments 2x2.....	101
Figure 6. 10 Velocity contour for compartments 2x3.....	102
Figure 6. 11 Cumulative probability of a molecule exiting the three microreactors for compartments 2x3.....	102
Figure 6. 12 Residence time distributions of the three microreactors for compartments 1x3.....	103
Figure 6.13 Residence time distributions of the three microreactors for compartments 2x2.....	103
Figure 6.14 Residence time distribution of the three microreactors for compartments 2x3.....	104

ACKNOWLEDGMENTS

I would like to extend my appreciation to Dr. Kody Varahramyan, Dr. Raja Nassar, Mr. Ji Fang, Dr. Debasish Kuila and Dr. Yi Su for their instruction and advice during my research. I would like to thank the Institute for Micromanufacturing for offering me financial support and use of the cleanroom equipment and metrology lab.

I would give special thanks to all the staff members who have provided much helpful support, including Mr. Philip Coane, Dr. Xiaohe Xu, Mr. Dee Tatum, Mr. John McDonald Mr. Scott Williams and Ms. Deborah Wood. I would give special thanks Dr. Carey Cox for his advice on computational fluid dynamic simulation.

I would give my thanks to Dr. Shihui Zhao and Mr. Venkata Satish Nagineni for their help in chemical reaction preparation. I also would like to thank Dr. Xiaohe Xu, Mr. Dee Tatum, Mr. John McDonald Mr. Scott Williams, and Ms. Deborah Wood for their help in the development of fabrication processes related to my research which included both metrology instrumentation and in key cleanroom equipment. I would also give thanks to all of my group members, Wei Cao, Weisong Wang, Jackie Chen and Difei Qi for their help.

CHAPTER 1

INTRODUCTION

1.1 Microreactor Research Background and Literature Review

A microchemical reactor, or microreactor, is one of several chemical engineering unit process devices that are now being designed on the micrometer (μm) scale. Microreactors are miniaturized reaction systems containing one or more reaction channels with microscale dimensions. The use of microdevices made by advanced micromachining technologies makes it possible to handle very small quantities or very low flow rates of liquids and gases. This provides new opportunities in the chemical catalyst study area, the pharmaceutical industry, medical instrumentation area, and in many other fields.

Microreactors are micro structured apparatuses for effectively controlling chemical processes. And they offer many advantages. The small amounts of chemicals used in microreactors are environmentally friendly because less waste is produced. Scale-up to production by replication of laboratory scale microreactors would eliminate costly designs since only one engineering cycle would be needed, and offers the avoidance of the transport and long-term storage of dangerous chemicals. Besides the safety advantages, and in keeping with the idea of a process on a chip, heaters, heat exchangers, flow and temperature sensors, as well as other micro sensors and devices can be reduced

in size to integrate with the reactor, microreactors provide the opportunity for the best temperature control.

With small dimensions and correspondingly small internal volumes, microreactors have very high surface-to-volume ratios, hence the higher efficiency of heat transfer. Additionally, the molecules in the microreactor have shorter distances to travel, thus resulting in more rapid heat and mass transfer and an increased conversion reaction in comparison to traditional reactors.

Because of advantageous geometries, larger exchange rate, and larger surface contact area for microreactors, a higher degree of conversion is expected. As a result, the basic goals of any microreactor study are to develop methods to enhance fluid mixing, mass transfer and conversion of the reactions that applied to microreactors. Potential chemical process industry applications for microreactors range across the spectrum, from becoming the newest 'lab scale' experimental reactor to generating chemicals as needed at the site of their consumption to new iterations of smaller, faster, and better analytical devices.

Various research groups have successively developed microreactors and microfluidic devices for obtaining new analytical capabilities, point-of-use synthesis, and high mixing performance. For example, Jensen et al [1] fabricated a microreactor with cross flow geometry for the testing of porous supported catalysts. Pattekar et al [6] designed and tested a microreactor for increasing reaction conversion, and Stroock et al.[2] achieved effective and rapid mixing with a staggered herringbone mixer in which staggered and asymmetric grooves are placed on the floor of a straight channel. Ajmera et al.[3] demonstrated the use of a microreactor for on-demand production of phosgene

from chlorine and carbon monoxide with an activated carbon catalyst. These researchers etched a 625 μm wide, 300 μm deep, 20mm long reactor channel along with two perpendicular 400 μm wide catalyst-loading channels (at the reactor entrance) in silicon. The reactor entrance and exit consists of 10 parallel 25 μm wide channels. De Mas et al. [4] carried out the direct two-phase fluorination of toluene in a 2-parallel-channel (435 μm wide, 305 μm deep isosceles triangles, 2cm long) microreactor etched out of silicon and protected by silicon dioxide and nickel films. Yeong et al.[5] used a falling-film microreactor and explored four types of palladium catalyst for the hydrogenation of nitrobenzene to aniline. The reactor consisted of 64 parallel channels (300 μm wide, 100 μm deep, 78mm long, separated by 100 μm walls) machined and etched into a stainless steel plate and covered with Teflon and stainless steel. The purpose of our work is meant to design a microreactor generating higher conversion through mixing enhancement.

Microfluidics is a collection of processes for moving bulk fluid mass or controlling the paths of selected embedded particles, cells or molecules, in flows. Length scale matching between the flow and the device is the key for efficient momentum and energy transfers of the desired fluid motions. Microelectromechanical Systems (MEMS) enables us to handle minute amount of fluid in the nano or pico liter range [9]. With properly designed micro fluidic devices, molecules can be directly manipulated by the flow patterns inside the device, which provides a pathway to exploit the micro and nano world.

The microreactor is a high throughput microfluidics component. The study of microfluidics plays an important role in microreactor study. The term microfluidic device

generally refers to a set of technologies used for controlling the flow and reaction of minute amounts of liquids or gases in a miniaturized system. In the chemical processing industry, for example, reactors, mixers, heat exchangers, separators and analysis functions are fundamental “unit operations” that can be also realized at the microfluidic scale. Chemical process industrial applications cover the following areas: industrial automation (pneumatics, flow control sensors); dispensers (glue, solder, lubricants, and scents); power systems (fuel cells, micro-combustors, fluidic microthrusters); high throughput screening (miniaturised microtitre plates, dispenser components); drug discovery; genomics/proteomics (amplification, separation, hybridisation & sequencing); cell analysis (screening, counting, sorting); as well as biochemical monitoring of food, soil, water, air, for pesticides and biological applications[10].

Microreactors are typically made out of glass, quartz, plastic, silicon, and metals such as stainless steel. A microreactor system has been developed at the Institute for Micromanufacturing (IfM) for the study of the hydrogenation and dehydrogenation of aromatic compounds. Photolithography was used to create built-in devices that include an inlet, reactor chamber and an outlet. Built-in heaters and temperature sensors are integrated onto the backside of the reactor while the fluid channels were photo etched in the front side of the silicon substrate. The channels range from 5 to 100 microns wide by 100 microns deep.

Figure 1.1 shows a picture of microreactors that has been used for chemical study by the previous researchers at IfM. A four-inch diameter silicon wafer was used to fabricate eight of these reactors.

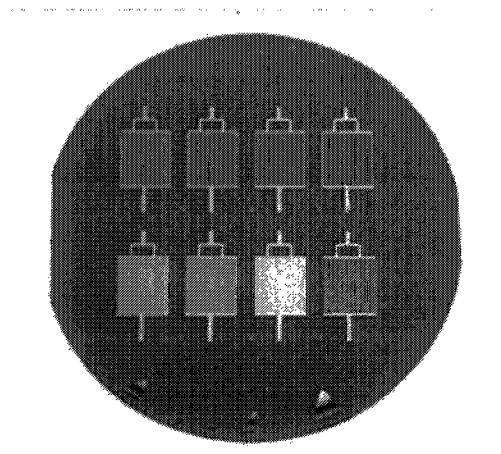


Figure 1.1 Microreactors used for chemical study

Although miniaturized reaction techniques offer many advantages in the chemical engineering, pharmacy, medical, and biotechnology industries, further research is necessary for a better understanding of these compact reaction vessels. In our research work, the understanding of fluid motion in the microchannels, of how different structures affect the mixing efficiency of the species, and the mixing phenomena in the structures are the driving force and purpose of this research.

1.2 Objectives

The Silicon microreactor is a useful tool for catalyst study and chemical process optimization. An accurate and precise quantitative prediction of fluid properties in the different microreactor configurations plays a very important role in conducting high conversion chemical reactions. The objectives of this research are to study the flow properties in differently structured microchannels, apply theoretical considerations to the real microreactor design, and thereby introduce a novel nested microchannel design- a microreactor with omega shaped microchannels.

The second objective of this research is to compare the fluid flow in the traditional straight, and zigzag channel designs with the novel omega channel, and use Computational Fluid Dynamics (CFD) simulation tool to further study the fluid flow and mixing phenomena in these three sets of microreactors.

Residence time distribution (RTD) of a microreactor is a reflection of the mixing of different reactant species inside the microreactor. Therefore, the residence time distribution exhibited by a certain type of microreactor is one of the most informative characterizations concerned with its performance and conversion efficiency. The third objective of this research is, therefore, to use Markov chain techniques to characterize the differences in the structural microreactors, and exhibit the molecules' residence time distribution in the novel microreactor, and then compare it with those of the straight, and zigzag channel microreactors, and predict the reaction conversion efficiency.

The fourth objective of this research is to apply the CFD simulation and Markov chain model to the microreactor design and predict the resident time distribution function for the micoreactors in order to allow the microreactor with better performance to stand out. Once the designs are determined, micromaching technology and dry etching processes are to be used for microreactor fabrication.

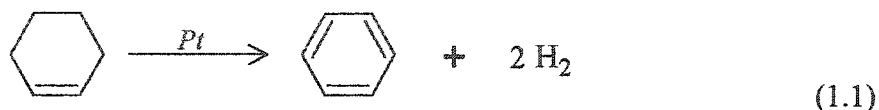
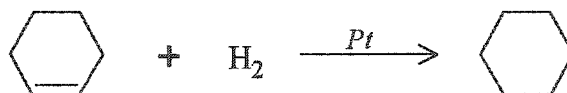
The fifth objective of this research is to carry out Fischer-Tropsch reactions in straight, zigzag, and omega-shape channel silicon microreactors at atmospheric pressure, controlled temperature and inlet outlet flow rates to study and contrast the conversions in the three different types of microreactors.

The last objective of this research is to compare the conversion results with the CFD and Markov chain model, and determine which prototype has the better performance. The objective is expected to provide a precursory research and solid base for a Fischer-Tropsch reaction evaluation. The knowledge we obtained from these studies will set valuable guidelines for designing and configuring different microfluidic devices to support the development of a μ Total analysis system [11].

1.3 Microreactor Application Reactions

Microreactors are miniaturized devices that need less space, materials, and energy, often having shorter response times and providing inherent safety of operation as mentioned previously. The microreactor technology is no longer in its infancy. Many researchers[3][4][5][8] have successfully applied this technology to chemical, biochemistry, biomedicine and medical diagnosis. Chemical microsystems are gaining an important position in the fields of analysis and synthesis due to their high surface area to volume ratio, low transport resistance, robust construction and so on. Those characteristics result in better heat and mass transfer properties [10][12]. Microreactor synthesis shows great promise for its unique advantages, such as inherent safety of operation, low consumption of reactants, and higher speed catalyst characterization. Three application reactions have been applied in previous research efforts [14].

1.3.1 Hydrogenation and Dehydrogenation of Cyclohexene



There are two classes of reaction in the area of heterogeneous catalysis, they are hydrogenation and dehydrogenation of aromatic compounds, which are particularly important to the petroleum refining industry. These reactions require a metal catalyst, usually Pt, Pd or Ni, and the mechanism involves adsorption of hydrogen to the metal surface. In the prototype experiment, a setup used has been developed by previous researchers [15]. They designed and fabricated microreactors deposited with a Pt catalyst in the microchannels to investigate different model reactions for conversion and selectivity of desired products. The reactor in this experiment is based on the reactions of cyclohexene (C_6H_{10}) and hydrogen over a platinum catalyst. The previous and proceeding researches have studied the reactions of cyclohexene (C_6H_{10}) and hydrogen over a platinum catalyst, a model for many similar systems ubiquitous to the chemical process and petroleum refining industries. The reacting system permitted the study of the effects leading to the selectivity of one or the other of the primary products cyclohexane (C_6H_{12}) and benzene (C_6H_6) through the reactions as shown in equation 1.1 [15].

Transport processes can be enhanced so that the underlying chemistry can be analyzed while minimizing any interfering effects due to the small linear dimensions. Under some situations, nearly ideal reactor behavior may be realized, being characterized

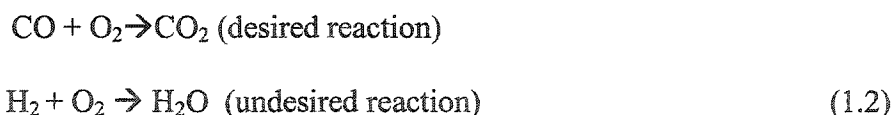
by spatially independent values of concentration and temperature and a well-defined residence time [15].

1.3.2 Preferential Oxidation for CO Amelioration in Hydrogen Fuel Cell Feeds

A fuel cell is a battery in which a fuel, normally hydrogen or methanol, reacts at the anode and oxygen reacts at the cathode. However, unlike in a normal battery, fuel cell electrodes are not consumed - only the fuel is consumed [16]. In most cases, hydrogen is the preferred fuel for use in the present generation of fuel cells being developed for commercial applications [16][17]. When generating hydrogen from natural gas, methane, or methanol, one of the by-products is carbon monoxide. The presence of carbon monoxide in the hydrogen rich feed gas to fuel cells can poison the platinum anode electrode and dramatically reduce the power output. Therefore, carbon monoxide clean-up and amelioration is very important for fuel cell technology development.

Researchers have developed a compact CO selective oxidation unit based on two coated aluminum heat exchangers [12][19]. Experimental results show that the selective oxidation unit can reduce the CO from 2% to less than 15 ppm and is suitable for a vehicle fuel cell power plant of 20 kWe . In 2001, the same group reported a metal based catalytic CO oxidation reactor which makes CO concentrations from a typical steam reformer output of 7000 ppm input to less than or equal 15 ppm in the presence of approximately 75% hydrogen [18][19]. The reactor design was based upon the catalyst coating of high surface area heat transfer technology. Catalyst screening studies have revealed a mixed transition metal oxide promoted platinum-ruthenium formulation to be suitable for the particular reactor application, i.e. acceptable CO oxidation activity and selectivity within a temperature range of 130-200 °C.

In previous studies [15][18], the researchers have focused on preferential oxidation of CO using a microreactor. The reactions are shown below:



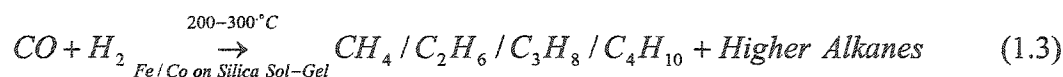
A high conversion is required to reduce the CO concentration to a level that is not detrimental to a Proton Exchange Membrane (PEM)-based fuel cell. High selectivity to O₂ is necessary because hydrogen is used to generate electricity in the fuel cell [18][19].

1.3.3 Fischer-Tropsch Synthesis

Fischer-Tropsch Synthesis is also called syn-gas conversion. Currently there is an abundance of research on syn-gas. Several corporations like Exxon-Mobil, Shell, and Rentech are involved in liquefying natural gas and a few of them had already commercialized the product. In general, the product range includes the light hydrocarbons methane (CH₄) and ethane (C₂H₆), LPG (C₃-C₄), gasoline (C₅-C₁₂), diesel(C₁₃-C₂₂), and light and waxes (C₂₃-C₃₂ and >C₃₃, respectively) [17].

The distribution of the products depends on the catalyst and the process operation conditions such as temperature, pressure, and residence time. Out targeted reactors will apply on syn-gas conversion for conversion testing.

Presently our research is primarily focused on the synthesis of higher alkanes in a microreactor fabricated with a sol-gel encapsulated iron and cobalt catalyst. The reaction is expressed as the following:



Several types of catalysts can be used for the syn-gas conversion, the most important are based on iron (Fe) or cobalt (Co). The Cobalt catalyst has the advantage of

a higher conversion and a longer life. The Co catalyst is, in general, more reactive for hydrogenation and therefore produces less unsaturated hydrocarbons and alcohols as compared to an iron catalyst. The iron catalyst, however, has a higher tolerance for sulphur, is cheaper, and produces more olefin products and alcohols. The lifetime of the Fe catalyst is short, and in commercial installations, generally limited to eight weeks [17].

1.4 Fabrication Methods

Fabrication of MEMS devices involves processes used in the IC industry, and they include optical lithography, surface micromachining, bulk micromachining, lift-off, etc. We will focus on optical lithography, nano lithography, and Inductively Coupled Plasma (ICP) etching processes, that served as research approaches for this entire research effort.

1.4.1 Optical Lithography

The process of optical lithography involves a series of photomasks that have been developed from a series of templates from the general design chart, and each lower level template must be designed coherently with each upper level template in order to fulfill the total concept of the three-dimensional MEMS structure. A lithographic system includes exposure tool, mask, resist, and all of the processing steps to accomplish pattern transfer from a mask to a resist and then to devices. It is typically the process of transferring geometric shapes on a mask to the surface of a silicon wafer. The steps involved in the photolithographic process are wafer cleaning; barrier layer formation; photoresist application; soft baking; mask alignment; exposure and development; and hard-baking[21][22]. Although lithography system costs increase as minimum feature size on a semiconductor chip decreases, optical lithography remains attractive because of

its high wafer throughput. The range and the application of the optical lithography were summarized and shown in Table 1. 1 [23][24].

Table 1. 1 The range and the application of the optical lithography

Optical Lithography Sources	i-line mercury lamp	KrF excimer laser	Ar F excimer laser	F ₂ excimer laser
Wavelength	365 nm	248 nm	193 nm	157 nm
Numerical Aperture	0.65	0.63~0.80	0.63~0.85	0.70~0.85
Node Feature Size	> 120 nm	90~120 nm	70~90 nm	55~70 nm
Minimum Feature Size	140 nm	75~100 nm	55~75 nm	45~55 nm

1.4.2 Electron Beam Lithography

The shrinking of feature size has led to a boom in the IC and telecommunication industry because of the achieved reduction in device cost and improved performance. However, as dimensions are scaled down, optical lithography will approach its physical limit. Optical lithography is now facing serious obstacles due to limitations in wavelength. It has also been shown that even when all possible enhancement technologies are applied, we are close to the physical limits of optical lithography.

Electron-beam and X-ray lithographies, have been considered as alternatives to optical lithography. However, wafer throughput with Electron-Beam lithography (EBL) is too slow to use in current semiconductor wafer production. Currently, EBL is regarded as complementary to optical lithography in exploring nanolithography.

Electron beam lithography scans a finely focused beam of high energy (10 to 100 keV) electrons across the sample under computer control. The wavelength of an electron at typical EBL beam energy levels is on the order of 1 Å and therefore, the diffraction

effects are negligible. Features as small as 10 nm have been written in resist with EBL [25]. Figure 1.2 shows a schematic drawing of an electron beam projection system [25].

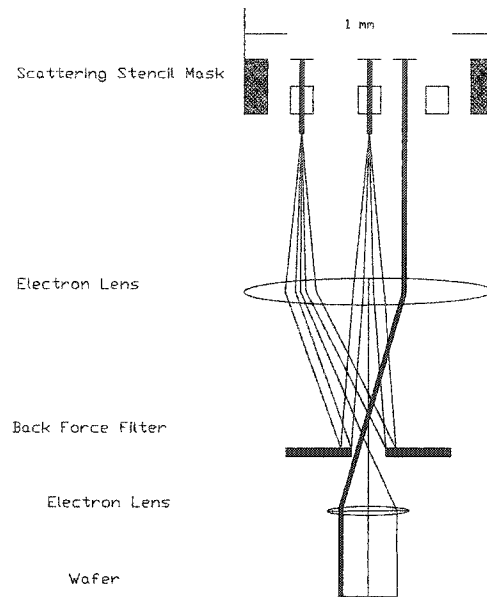


Figure 1.2 Schematic drawing of electron beam projection system

Electron beam exposure systems have four main subsystems: (1) electron source (gun), (2) electron optical column (the beam-forming system), (3) mechanical stage, and (4) the computer used to control the various machine subsystems and transfer pattern information to the beam deflection coils [25].

E-Beam Resists: Electron beam sensitive resists are the recording and transfer media for EBL. The common resists are polymers that are dissolved in a liquid solvent. After baking out to drive off the casting solvent, electron exposure is used to modify the resist. As in optical lithography, there are two types of EBL resists: positive tone and negative tone. Positive tone resists develop away at the exposed regions whereas in the case of negative tone resists the exposed regions remain after development.

Some of the positive tone EBL resists are: PMMA (Poly methyl methacrylate), EBR-9 (an acrylate based resist), PBS (Poly butene-1-sulphone), ZEP (a copolymer of a -chloromethacrylate and a -methylstyrene). On the other hand, negative e-beam resists function on the basis of radiation-initiated cross-linking reactions that result in the formation of interchain linkages, which generate a cross-linked, three-dimensional network, which is insoluble in developer. A negative tone EBL resist is Shipley SAL (has 3 components, a base polymer, an acid generator, and a crosslinking agent.)

Electron solid interactions: As the electrons penetrate into the resist material some of them experience small angle forward scattering and many of them experience large angle scattering events leading to backscattering. This causes additional exposure in the resist leading to what is called the electron beam proximity effect. Figure 1.3 shows the effects of electron scattering in electron beam resist exposure. As the primary electrons slow down, most of their energy is dissipated in the form of secondary electrons with energies from 2 to 50 eV. These are responsible for the bulk of the actual resist exposure process. Since their range in resist is only a few nanometers, they contribute little to the proximity effect. A small fraction of secondary electrons may have significant energies, on the order of 1 keV. These so-called high energy secondary electrons can contribute to the proximity effect in the range of few tenths of a micron [26] [27].

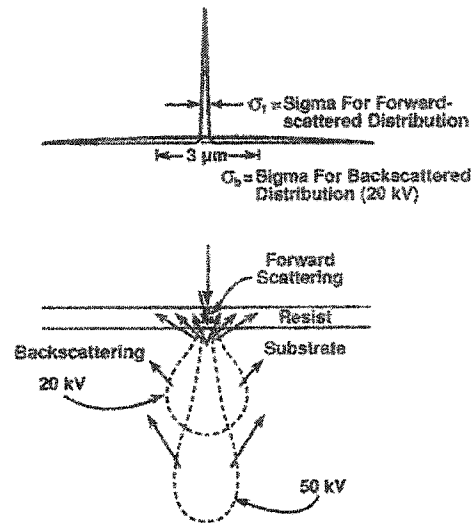


Figure 1.3 Electron scattering in electron beam resist exposure

Nanotechnology provides the exciting possibility of testing metrology with nanofeatures long before these feature sizes are available from advanced lithography. Electron-beam lithography can be used to fabricate some nanofeatures, the AFM tip for example. The biggest drawback is the need for controlling micro-roughness. Sidewall roughness can come from both printing geometries in resist and etching these structures.

1.4.3 Dry Etching Process

Dry etching technology can be separated into in three separate classes called reactive ion etching (RIE) , sputter etching, and vapor phase etching.

In RIE, the substrate is placed inside a reactor in which one or more gases are introduced. A plasma is struck in the gas mixture using an RF power source, breaking the gas molecules into ions. The ions are accelerated towards and react at the surface of the material being etched, forming a gaseous by product. This is known as the chemical part of reactive ion etching. There is also a physical part which is similar in nature to the

sputtering deposition process. If the ions have high enough energy, they can knock atoms out of the material to be etched without a chemical reaction. It is a very complex task to develop a dry etching process that balances both chemical and physical etching, since there are many parameters to adjust. By changing this balance it is possible to influence the anisotropy of the etching process. The combination of the chemical part and physical part can form sidewalls that have shapes varying from rounded to vertical due to the fact that the chemical part is isotropic and the physical part is highly anisotropic,

A special subclass of RIE, which continues to grow rapidly in popularity is deep RIE (DRIE). In this process, etch depths of hundreds of microns can be achieved with almost vertical sidewalls. There are several inductor coils around the top of the chamber, which are driven by RF power. The inductor produces an alternating magnetic field in vertical direction. This alternating magnetic field produces a circular alternating electric field in the horizontal direction. The silicon substrate is biased by RF power and the ion energy is controlled by the RF power at the plasma electrode. The etching aspect ratios from 1 to 50 can be achieved. The process can easily be used to etch completely through a silicon substrate, and etch rates are 3-4 times higher than wet etching. Figure 1.4 shows a schematic view of the DRIE working principle.

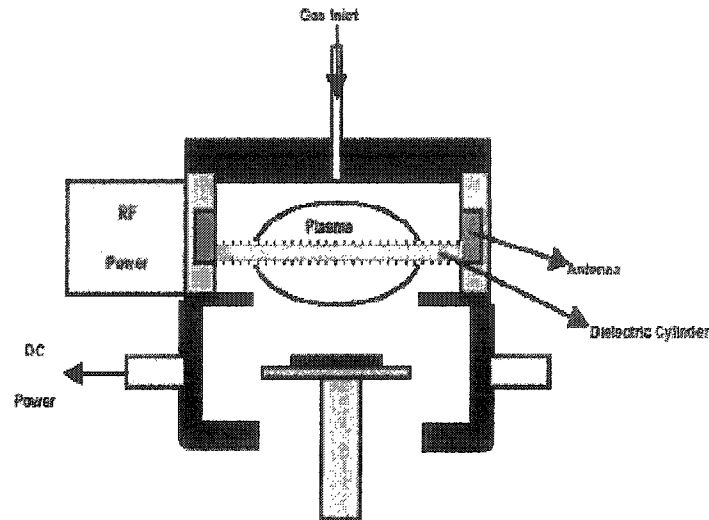


Figure 1.4 Schematic of DRIE principle

Discharge pulsing has recently been classified as a promising method to address a number of problems in plasma etching for semiconductor and MEMS fabrication. These include control of selectivity, particulate contamination, substrate heating or cooling problem, device damage and feature profiles. Increased attention has been given to exploring the applications for performing effective plasma etching in both academia and industry.

CHAPTER 2

THEORETICAL CONSIDERATION

2.1 Reaction Background

Synthesis in microreactor shows great promise for its unique advantages like inherent safety of operation, low consumption of reactants, and greater speed in catalyst development. The experiments using Fischer-Tropsch (F-T) synthesis will be carried out in this research for purpose of microreactor calibration. The exact mechanisms of the F-T reaction is very complex, not well defined, and still the subject of much debate. Basically, the F-T synthesis mechanism may be divided into at least 3 major steps: firstly, initiation or C compound formation by CO adsorption on the catalyst metal surface, and then the C – O bond is broken. Secondly, hydrogenation of -C to -CH₂ and hydrocarbon chain growth by successive insertion of the C building blocks. Thirdly, the chain is terminated by desorption of unsaturated surface species, and the hydrogenation and desorption of saturated species.

2.2 Fluid Dynamic Background

Micro/nano flows are very different from macro flows. Continuum flow is commonly assumed in macro flows. Molecular effects are represented by physical constants such as viscosity. In macro flows, the inertia of the fluid mass is usually much larger than the viscous force due to the large Reynolds number. The most interesting phenomena are the

manifestations of non-linear effects associated with the inertial forces. In micro devices, the typical Reynolds number is much less than one due to the small length scale, which results in a high velocity gradient and thus high viscous force.

When the fluid is air, the force due to drag is called aerodynamic drag or air resistance. When the fluid is water, the force due to drag is called hydrodynamic drag. The drag force depends on the way fluid flows around the object; therefore, the shape of the structure has a very large effect on the amount of drag produced, regardless of whether the fluid is air, water or something else, there are two types of flow: laminar and turbulent.

2.2.1 Flow Regimes

The Reynolds number is named after Osborne Reynolds who conducted an experimental study to see how and when laminar and turbulent flows occur through a pipe. The Reynolds number is a dimensionless parameter and is defined as:

$$R_e = \frac{\rho UL}{\mu} \quad (2.1)$$

where ρ is fluid density, μ is viscosity coefficient, U is average velocity and L is the characteristic length scale. L is defined as $\frac{4 * \text{cross section area}}{\text{wetted perimeter}}$ for a pipe or a rectangular channel. Reynolds number depends on material properties (density, viscosity), boundary conditions and critical velocity.

The Reynolds number is important in analyzing any type of flow when there is a substantial velocity gradient (i.e., shear). It indicates the relative significance of the viscous effect compared to the inertia effect. The Reynolds number is proportional to the inertial force divided by viscous force. When the layers of fluid slide over each other in a regular fashion, the flow is called laminar. For water, and $R < 2,100$, the flow in the pipe was laminar. When the Reynolds number is above 40,000, the flow was always turbulent. For air laminar flow occurs when the air stream around the object is smooth. Under these conditions, the aerodynamic drag is low. At low Reynolds numbers, the behavior of a fluid depends mostly on its viscosity and the flow is steady, smooth, viscous, or laminar. At turbulent flow regime, mixing occurs between adjacent layers and velocity vectors develop unpredictably.

The high surface area relative to the volume in the microreactor will dramatically affect the transfer of mass, momentum and energy. Inertial forces will be small while surface friction and viscous effects will increasingly dominate the fluid motion. As a consequence, most microfluidic systems operate in the laminar regime.

2.2.2 Flows in Microscale

Many early investigations of non-continuum flows in channels have been conducted by researchers[29]. The introduction of the concepts of mean free path and Knudsen number are used to define the flow regimes. The mean free path of the molecules (λ) can be related to temperature (T) and pressure (P) via the following relationship:

$$\lambda = \frac{K_B T}{\pi P \sigma^2 \sqrt{2}} \quad (2.2)$$

Where K_B is Boltzmann's constant ($=1.38 \times 10^{-23} \text{ JK}^{-1}$), σ is the molecule diameter in meters, (typical molecular diameters are 0.2 to 0.3 nm), T is temperature in Kelvin and P is pressure in Nm^{-2} , and L is the characteristic length scale of the flow geometry. This length scale should be chosen in order to include the gradients of density, velocity and temperature within the flow domain. The ratio between the mean free path, λ , and the characteristic dimension of the flow geometry, L , is commonly referred to as the Knudsen number:

$$Kn = \frac{\lambda}{L} \quad (2.3)$$

Several researchers have proposed models to describe those flow regimes. According to the Knudsen number for flow regimes, flows are divided into various regimes. They are: continuum, slip, transition and free-molecular flow. Figure 2.1 shows the governing equations for these flow regimes [30].

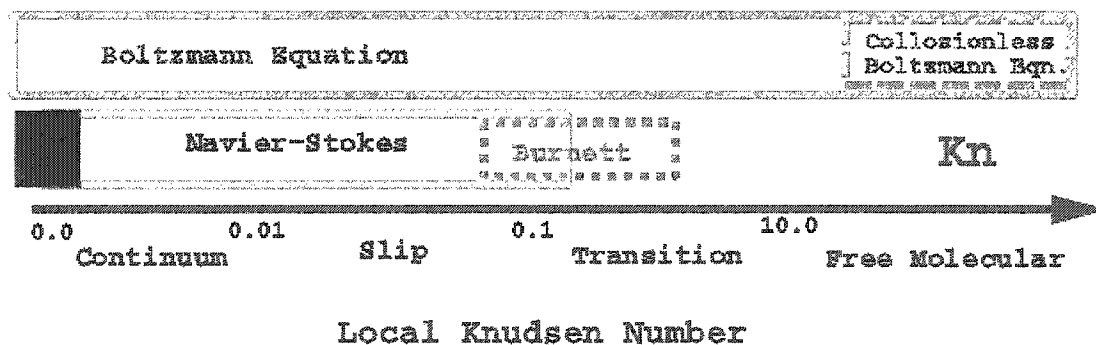


Figure 2.1 Knudsen Number and the Flow Regimes

Some researchers claimed that microflows are typically in the continuum flow, slip and early transitional flow regimes. Therefore, Navier-Stokes equations with appropriate slip boundary conditions govern these flows as illustrated in Figure 2.1.

Continuum Flow: gaseous flow is called continuum flow when the Knudsen number is in the range of 0 to 0.01. The Navier-Stokes equation describes continuum flow very well. The bulk of the gas flow maintains a parabolic velocity profile with zero velocity at the wall and maximum flow rate at the cross-sectional center of the flow. The Hagen-Poiseuille equation shows the mass flow rate in a circular tube.

$$V = \frac{\pi R^4 \Delta P}{8 \mu L} \quad (2.4)$$

where V is the volume flow rate in m³/s, R is the radius of a circular pipe in m, ΔP is the pressure drop between inlet and outlet in Pa, L is the pipe length, and μ is the fluid velocity.

Slip flow: When the Knudsen number is between 0.01 and 0.1, the flow is called slip flow. The gas close to the walls has a velocity greater than zero (like the gas is slipping along the wall with a certain velocity), while the gas flow maintains a parabolic velocity profile beside the wall.

The governing equations for building a slip flow model include the Navier-Stokes equation, the mass continuity equation, and the ideal equation of state. The slip velocity at the interface depends on flow properties and the tangential momentum accommodation between the gas and the channel wall. Applying the proper slip flow boundary conditions to the above equations will help us to study the flow in the microchannel.

And it is interesting to note that as the inlet to outlet pressure ratio decreases, the effects of slip becomes a more significant contribution to the entire flow. It can also be observed that the curvature in pressure distribution increases with an increasing inlet to

outlet pressure ratio. The mass flow rate is larger for slip flow than for non-slip flow (when $Kn_0 = 0$). Researchers believe that the mass flow rate increases due to the decrease in friction factor [29].

Transition Flow: When the Knudsen number is between 0.1 and three, the flow is called transitional flow. This regime is defined by a smaller velocity profile in the bulk of the gas flow than that of the slip flow, and an increasing field of slip at the channel walls. The slip and free molecular flow present distinct a pressure profile for gaseous flow along a microchannel and the transition flow provides a region in which the characteristics of gaseous flow undergoes a transformation. This transformation is the result of the competition between intermolecular collisions and collisions of the gas molecules and the wall surface [31]. It is a multiphase-fluid flow regime characterized by a chaotic mixture of liquid and gas, with neither phase appearing to be continuous.

Free Molecular Flow: When the Knudsen number is larger than three, the flow is called free molecular flow. In this regime, the intermolecular collisions can be assumed to be negligible. The mean free path of the gas is greater than the depth of the channel, therefore the gas is considered to be diffuse along the length of the channel.

2.3 Governing Equations for Fluid Motion

The flow of a fluid through a control volume is governed by the continuity equation and Navier-Stokes equations, which are formulated by applying the conservation of mass, momentum and energy in the control volume.

Conservation of mass tells us that the spatial integral over region is subject to :

$$\int_{\Omega_0} \rho(x,0) dx = \int_{\Omega_t} \rho(x,t) dx, \quad (2.5)$$

Therefore, time derivative of mass integrals in the transport theorem must vanish. Bearing in mind the following relation [32][33]:

$$\frac{d}{dt} \int_{\Omega_t} f(x,t) dx = \frac{d}{dt} \int_{\Omega_t} \left[\frac{\partial}{\partial t} f + \nabla \cdot (fv) \right] (x,t) dx, \quad (2.6)$$

which gives us the continuity equation for compressible fluids:

$$\frac{\partial}{\partial t} \rho + \nabla \cdot (\rho v) = 0 \quad (2.7)$$

where ρ is the density of the fluid, u , v , and w are the local fluid velocity in x , y , and z directions. For incompressible fluids, it becomes:

$$\nabla \cdot v = 0 \quad (2.8)$$

where v is the velocity vector and ∇ is used as the gradient operator. The equation implies that the rate of change of mass within the control volume is balanced by the mass entering and leaving the volume.

The Momentum Equation in vector form can be expressed as:

$$\frac{\partial \vec{V}}{\partial t} + \vec{V} \cdot \nabla \vec{V} = -\frac{1}{\rho} \nabla P + \mu \nabla^2 \vec{V} + \vec{f} \quad (2.9)$$

where \vec{V} is the velocity vector, P is pressure, term $\vec{V} \cdot \nabla \vec{V}$ is the flux moment of the flow, term $\nabla^2 \vec{V}$ is the stress tensor, \vec{f} is the vector of body force per unit mass acting on the fluid element [32]. The equation shows that the rate of change of momentum in a volume is equal to the sum of the forces on the volume. The left hand side corresponds to the material change of the momentum in the control volume, and the right hand side is the force balance, which includes pressure, shear stress, and the body force. This equation is also called the Navier-Stokes equation.

The Navier-Stokes equations are non-linear partial differential equations and no general solutions exist. Analytical solutions can be obtained under particular conditions, such as incompressible, irrotational flow, or fully developed flows where the acceleration term is zero [34]. In our study, we are interested in finding exact solutions for only fully developed laminar flow in a rectangular channel with length (L), and depth (D) formed by parallel walls that are at a distance of 2B apart. At low Reynolds numbers, the Navier-Stokes equation can be simplified as [35]:

$$\nabla P = \mu \nabla^2 \vec{v} \quad (2.10)$$

$$\frac{\partial}{\partial x} \frac{\partial v_x}{\partial x} = -\frac{P_1 - P_2}{\mu L} \quad (2.11)$$

Solving gives us: $\frac{\partial v}{\partial x} = -\frac{P_1 - P_2}{\mu L} x + C_1$ and $v = -\frac{P_1 - P_2}{\mu L} x^2 + C_1 x + C_2$

For the non-slip flow, the boundary condition is that the velocity is 0 at the channel wall.

Therefore we have: $v(-B) = v(B) = 0$. Substituting these values into the velocity

equation, we get $C_1 = 0$ $C_2 = \frac{P_1 - P_2}{2\mu L} B^2$, and therefore, $v = \frac{P_1 - P_2}{2\mu L} (B^2 - x^2)$.

The flow in such channel geometry is known as Poiseuille flow (or Hagen-Poiseuille flow for historical accuracy) and can be expressed as:

$$v_y = \frac{\Delta P B^2}{2\mu L} \left[1 - \left(\frac{x}{B} \right)^2 \right] \quad (2.12)$$

2.4 Derivation of Flow Rate in Microchannels

Our design focuses on obtaining sufficient number of collisions with the channel surface which depends on the cross section and the actual length of the channel, because the number of molecular collisions on surface will considerably affect the reaction conversion. Increasing the number of collisions between the reactant flow and the catalyst on the channel wall will increase the reaction conversion.

A turbulent flow regime is preferred to laminar flow, because it allows improved mixing and heat transfer normal to the flow. That is one of the driving forces for introducing and designing the zigzag channel and omega channel microreactor in this research.

The development of lab-on-a-chip devices requires some analytical task mixing strategies that need to be both efficient and simple fabrication-wise. Indeed, flows at such a small scale are laminar because of a low Reynolds number which leads to non-continuum effects as the feature size is reduced. One cannot rely solely on turbulence to achieve fast mixing. Again we use different shaped channels such as, zigzag and omega that form obstacles for the fluids and therefore, passively increase both the Reynolds number of the flow and mixing efficiency. This allows easier fabrication using common lithographic methods. An understanding of the behavior of mixing in the microscale counterpart can provide the tools to facilitate the design and optimization of innovative devices.

Several aspects of our observations will be discussed in this section: pressure drop, mass flow rate, and mixing behaviors in the introduced channels.

2.4.1 Flow in a Straight Channel

The fundamental reactor consists of an array of narrow straight channels. The flow regime in this straight microchannel reactor is laminar flow in a micro-scale channel of length L (Reynolds numbers much smaller than the threshold value of 4000) and depth D formed by parallel walls that are spaced at a distance of $2W$ apart. The velocity of flow in the microchannel has been expressed in equation (2.12).

It can be shown that the velocity distribution for laminar flow of a Newtonian fluid in a microchannel is parabolic. V_{\max} occurs when $\frac{dv_y}{dx} = 0$, and, therefore,

$$V_{\max} = \frac{\Delta P B^2}{2\mu L}.$$

Consequently, the volumetric flow rate and mass flow rate can be derived from the velocity function. The volumetric flow rate of a system is a measure of the volume of fluid passing a given cross sectional area in the system per unit time. The volumetric flow rate can be calculated as the product of the cross-sectional area for flow and the average velocity.

The average velocity is obtained by dividing the volumetric flow rate by the cross-sectional area [68]. Therefore,

$$V_{\text{average}} = \frac{\text{volumetric flow rate}}{2BD} = \frac{\int_{-w}^w v_y D dx}{2BD} = \frac{2}{3} V_{\max} \quad (2.13)$$

The mass rate of flow can be expressed as *mass flow rate* = $\rho \cdot \text{volumetric flow rate}$, where ρ is the density of the flow. Mass flow rate can also be obtained by integrating the velocity profile over the cross section of the channel as follows:

$$Q = \int_{-B}^B \rho v_y D dx = 2\rho B D v_y \quad (2.14)$$

The final expression for the mass flow rate is

$$Q = \frac{2\rho\Delta P B^3 D}{3\mu L} \quad (2.15)$$

It can be shown that the mass flow rate vs. pressure drop (Q vs. ΔP) expression in a fluid (of density ρ) in this laminar flow microchannel is a channel analog of the Hagen-Poiseuille equation shown in equation (2.12).

2.4.2 Flow in a Zigzag Channel

Flow in zigzag channel is much more complex than that of the straight channel. Analogously, for the zigzag channel, the velocity of flow in the stream wise direction is:

$$v_{streamwise} = \frac{\Delta P B^2}{2\mu L \cos \alpha} \left[1 - \left(\frac{x}{B} \right)^2 \right] \quad (2.16)$$

And the flow rate vs. pressure drop can be expressed as

$$Q = \frac{2\rho\Delta P B^3 D}{3\mu L / \cos \alpha} \quad (2.17)$$

where α is the inclination of the zigzag channel axis with the vertical axis. The above two equations are only partially valid for the straight segment of the channel part. For the angled segment of the channel, there is an area with a sudden increase of velocity that is caused by inertial effect, which can not be explained by the Equations 2.16 and 2.17. The average flow velocity, it still subject to the following relation: $V_{average} = \frac{2}{3} V_{max}$

As the Reynolds number increases, some hydrodynamic effect, such as laminar recirculations, at each angle of the zigzag channel will occur. The recirculation phenomena has been explained by Virginie Mengeaud [34] that it is caused by inertial effect. This inertial force caused by the high flow velocity, will lead to recirculation of local velocity and an inversion of pressure gradient and consequently improve mixing of the species.

2.4.3 Flow in a Omega Channel

Notice that in both the straight and zigzag channels, the flow goes forward with little or no disturbance. Besides the phenomena occurring in the zigzag channel angled segment discussed in the above section, the fluid is expected to generate more significant mixing phenomena. The obstacle formed by the omega channel will force the flow lines co-mingle from center to the boundary channel wall and from boundary channel wall to the center periodically. A channel unit consisting of continuous and discontinuous walls, stretching and tilting the flow species, is developed in this research and is called the omega channel, because its shape is analogous to the Greek alphabet character Ω . The omega channel unit is shown in Figure 2.2.

As we have mentioned previously about the drag force, we know that shape has a very large effect on the amount of drag produced. Drag is an aerodynamic force and therefore depends on the pressure variation of the air around the body as it moves through the air. The total aerodynamic force is equal to the pressure times the surface area around the body. Drag is the component of this force along the flight direction. Like the other aerodynamic force, lift, the drag is directly proportional to the area of the object. Doubling the area doubles the drag. If we think of drag as being caused by friction

between the air and the body, a logical choice of changing drag would be the total surface area of the body. If we think of drag as being a resistance to the flow, a more logical choice of changing drag would be the frontal area of the body which is perpendicular to the flow direction.

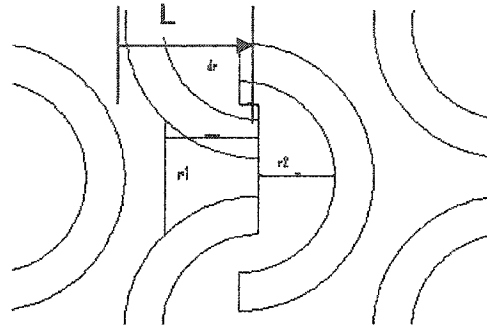


Figure 2.2 Omega channel

The relationship between mass flow rate and pressure drop in a Newtonian fluid in a rectangular channel of width $2B$, and depth D has been expressed in equation 2.15. It can be noted that the flow rate does not change with axial distance, when the channel walls are parallel. For region L in the omega channel, we can rewrite 2.15 as:

$$\frac{\Delta P}{L} = \frac{3Q\mu}{2\rho DB^3} \quad (2.18)$$

In order to derive the velocity of the flow at region L of an omega channel, the following assumptions are made:

- 1). That the flow in the omega channel is a quasi-one dimensional flow [36], which can be described by locally treating the flow between non-parallel walls as flow between parallel walls;
- 2). That equation 2.18 is approximately valid for a differential dx of the channel; and

3). That the width of the channel can be expressed as a function of x at region L, where x refers to the axial channel length.

Hence the above equation can be re-written as:

$$-\frac{dP}{dx} = \frac{3Q\mu}{2\rho DB(x)^3} \quad (2.19)$$

And Equation 2.19 can be integrated to get the pressure drop across the channel on substituting the width function $B(x)$.

$$\int_{P_{in}}^{P_{out}} -dP = \int_a^b \frac{3Q\mu}{2\rho DB(x)^3} dx \quad (2.20)$$

Therefore the pressure drop is expressed as $(P_{in} - P_{out}) = \frac{3Q\mu}{2\rho D} \int_a^b \frac{dx}{B(x)^3}$. The mass flow

rate for a channel width function $B(x)$ can be expressed in a standard form:

$$Q = \frac{2\rho\Delta PD}{3\mu \int_a^b \frac{dx}{B(x)^3}} \quad (2.21)$$

The $B(x)$ function for the omega channel at region L is expressed as:

$B(x) = -\sqrt{r^2 - (x-r)^2}$, when $x \in [0, L]$; Where r is the radius of the curve, $2a$ is the maximum distance between the channel walls, $2B$ is the minimum distance between the channel walls. We can get the volumetric flow rate from the relationship: *mass flow rate* = $\rho \cdot$ *volumetric flow rate*. Dividing the volumetric flow rate by the cross-sectional area, we get the following expression for the omega channel in the region L:

$$V_{\omega} = \frac{\text{volumetric flow rate}}{2BD} = \frac{\Delta P}{3\mu B(x) \int_a^b \frac{dx}{B(x)^3}} \quad (2.22)$$

It can be observed that if in the omega channel case, B was a constant that did not change with the channel length of the micro reactor, then equation 2.22 would provide a constant average velocity.

The average flow velocities in straight and zigzag channels follow the relationship of $V_{\text{average}} = \frac{2}{3}V_{\text{max}}$, and V_{average} of both the straight channel and zigzag channel are constants. This shows that the variance between velocity values in the straight and zigzag channel is small. On the other hand, the velocity of flow in the omega channel varies from point to point, and the variance between the velocity values in the omega channel is large. The detailed fluid flow in the three sets of microchannels will be studied in chapter three.

2.4.4 Mixing of Fluids

The performance of the static mixer can be judged on the basis of the criterion of mixing quality in order to quantify its efficiency.

Let's first look at the concept of residence time distribution of a reactor :residence time distribution is the exit age distribution of fluid molecules leaving a reactor. The residence time is the total time spent by the fluid molecules within the reactor. It can be expressed as:

$$t_m = \int_0^{\infty} tE(t)dt \quad (2.23)$$

Figure 2.3 gives us a clear picture of residence time distribution, where t_m is the mean residence time distribution, and $E(t)$ is the concentration of the species at any given time.

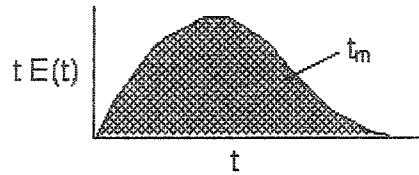


Figure 2.3 Mean residence time of reactor

From the calculation of the flow velocity in both straight and zigzag channel in equation 2.11 and equation 2.15, it can be observed that both of them have as a consequence the parabolic nature of the velocity field. Near the wall, the velocity field is linear with distance and thus a particle at distance d away from the wall takes a time $=L(r/d)$ to reach L . Flow near the wall will take a long time to exit, giving long tails in the residence time distribution as shown in Figure.2.3. Moreover, the fluid near the wall never co-mingles with fluid elements in the centre of the channel; therefore the mixing is poor.

The distributor is a device designed to ensure that the fluidizing gas is always evenly distributed across the cross-section of the reactor. It is a critical part of the design of a fluidized bed system. Good design is based on achieving a pressure drop which is a sufficient fraction of the reactor pressure drop [37]. Binomial, tree-shaped inlet/outlet geometries are also introduced into the microreactor design.

CHAPTER 3

FLUIDIC SIMULATIONS

Method of computational fluid dynamics is the use of computers to analyze problems in fluid dynamics. The usual method is to discretize the fluid domain into small cells to form a grid and then apply to solve the Navier-Stokes equations. The solution of the Navier-Stokes equation is sufficiently accurate alone for cases where the fluid flow is laminar. For turbulent flows special turbulence models must be used to introduce new terms into the equation. For many problems the solutions for the fluid equations are obtained at the same time as equations describing other properties of the system. These other equations can include those describing heat transfer, chemical reactions and radiation heat transfer. More advanced codes allow the simulation of more complex cases involving multiple fluids (“multi-phase”) or non-Newtonian fluids. The most widely used numerical methods are: finite difference method, finite element method, and finite volume method. Finite element method is a numerical approach for solving partial differential equations with fixed boundary conditions, either in steady state or transient systems and in two or three-dimensional space. The system is divided into a number of small geometrical areas (finite elements), whose edges constitute the nodes of a mesh.

The differential equations are solved at each node of the individual elements, modifying the PDE expression into a matrix form ($n \times n$ matrix for n nodes). The final formulation is decomposed into a matrix system that can be inverted with appropriate algorithms.

Similar to the finite difference method, in the finite volume method the values are calculated at discrete places on a meshed geometry. "Finite volume" refers to the small volume surrounding each node point on a mesh. In the finite volume method, volume integrals in a partial differential equation that contains a divergence term are converted to surface integrals, using the divergence theorem [38]. These terms are then evaluated as fluxes at the surfaces of each finite volume. The advantage of the finite volume method is that it is easily formulated to allow for unstructured meshes. The flow of a fluid through a control volume is governed by Navier-stokes equations, and these equations are formulated by applying conservation of mass, momentum and energy in an appropriate control volume [39].

When we consider a closed volume drawn within a finite region of the flow, this volume is defined as control volume V , which is a reasonably large, finite region of the flow. Therefore we could limit our attention to just the fluid in the finite region of the volume itself with the concept of control volume. The fluid flow equations that are directly obtained by applying the fundamental physical principles to a finite control volume are in integral form. These integral forms of the governing equations can be manipulated to indirectly obtain partial differential equations. The equations that are obtained from the finite control volume fixed in space are called the conservation form of the governing equations; the equations that are obtained from the finite control volume

moving with the fluid are called the nonconservation form of the governing equations. In all of these approaches the same basic procedures are followed.

- 1). The geometry (physical boundaries) of the problem is defined.
- 2). The space occupied by the fluid is divided into discrete cells (the mesh).
- 3). Boundary conditions are defined. This involves specifying the fluid behavior and properties at the boundaries of the problem.
- 4). The Partial differential equations are converted into algebraic equations and then transferred to matrix equations, and are solved iteratively, and
- 5). Analysis or visualization of the solution.

3.1 Introduction to the Simulation Tool

CoverntorWareTM developed by Coventor, Inc., [40] is a comprehensive MEMS design software. It integrates a suite of tools designed to produce accurately modeled MEMS designs, and enables users to design, specify and model MEMS structures. It includes several modules: MemCFD, Netflow, Reacsim, etc.

We use the MemCFD module to simulate different design models in this research. The MemCFD module supplies general CFD (Computational Fluid Dynamics) capabilities. It supports static and transient compressible and incompressible flows, with a wide range of standard and microfluidic boundary conditions. It is specific to the analysis of the microfluidic transport channels in chemical biological analysis systems. Moreover, important parameters for microfluidic characterization, such as interfacial areas in multiphase reactions, are either readily available or even predetermined by reactor geometry. Therefore, understanding of micro fluidic device mechanisms becomes more and more important. Microfluidic devices can be used to obtain a variety of useful

measurements including molecular diffusion coefficients, fluid viscosity, fluid velocity, chemical binding coefficients and enzyme reaction kinetics.

The governing equations for the MemCFD module are based on the Navier-Stokes equations. As mentioned in chapter two, these equations are formulated by applying conservation of mass, momentum and energy in an appropriate control volume. The continuum equation expressed in equation 2.7 is formulated by the conservation of mass in a control volume; the momentum equation expressed in equation 2.9 is formulated by the conservation of momentum in a control volume; and the energy equation expressed as :

$$\frac{\partial e}{\partial t} + v\nabla e = \nabla \cdot (k\nabla T) + H + \Phi \quad (3.1)$$

comes from the conservation of energy in a control volume. In equation 3.1, e is the internal energy of the system, H and Φ are the source and dissipation terms. The energy equation is a statement of the first law of thermodynamics which states that the increase in the energy within a volume is the result of work and heat transfer within the region. In the derivation of the continuum equation (equation 2.6), momentum equation (equation 2.8) and energy equation (equation 3.1), the fluid medium is assumed to be continuous. This implies that the energy in the system is transferred through molecular interaction. The validity of this assumption is governed by the Knudsen Number expressed in equation 2.3. The flow in the microreactor designed (channel thickness=50 μm , and depth=100 μm) is in continuous flow; with the same depth, if the channel thickness reaches to 1 μm or less, slip flow is generated. From Figure. 2.1, we can see that both continuum flow and slip flow are governed by Navier-Stokes equations. Consequently, MemCFD module is valid for modeling our cases.

3.2 Simulation of Fluid Flow in Microreactors

The study of fluid flow in different channel structures is presented in this section. The comparison is made to optimize the reactor structure. Such a design could find broad applications in enhancing the efficiency for the mixing of reagents, transport, and the reactive surface contact area for the device. Our goal is to increase the conversion of the reaction. To conserve memory in the whole simulation process, we first use single inlet and outlet in comparison with different channel structures.

The boundary condition used for the flow simulation was a constant flow rate at each inlet with the outlet being at atmospheric pressure, with no slip flow at the channel walls. The conditions are that all structures have the same input flow rate value; we will compare the steady state velocity distribution. 3-D structures for the three sets of microreactor are modeled by the MemCFD module of CoverntorWare™.

For the straight channels, the fluid is in gas phase and the inlet flow rate = 2.4×10^{-5} /s, and the meshing size is 3 μm . The velocity contour and sub-velocities across channel width in x and y direction are shown in Figure 3.1 and Figure 3.2. The laminar flow is very obvious in the straight channels ($Re \ll 1$). The line at $x = 450 \mu\text{m}$ was extracted and Figure 3.2 represents the velocity_x and velocity_y at $x = 450 \mu\text{m}$. The velocity in the x direction presents parabolic distribution which is in agreement with equation 2.11, with a maximum value of 250 $\mu\text{m/s}$. The velocity in y direction is almost 0.

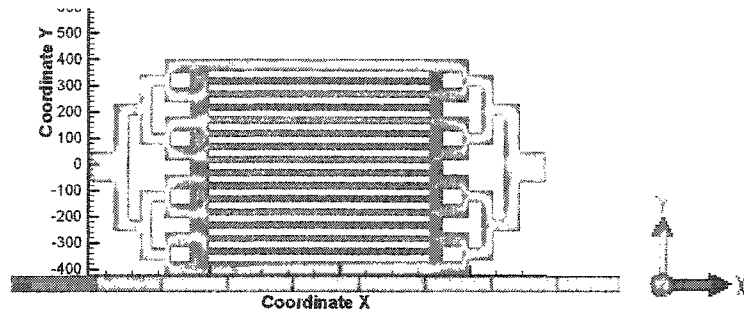


Figure 3.1 2-D Top View Velocity contour of the straight channel reactor

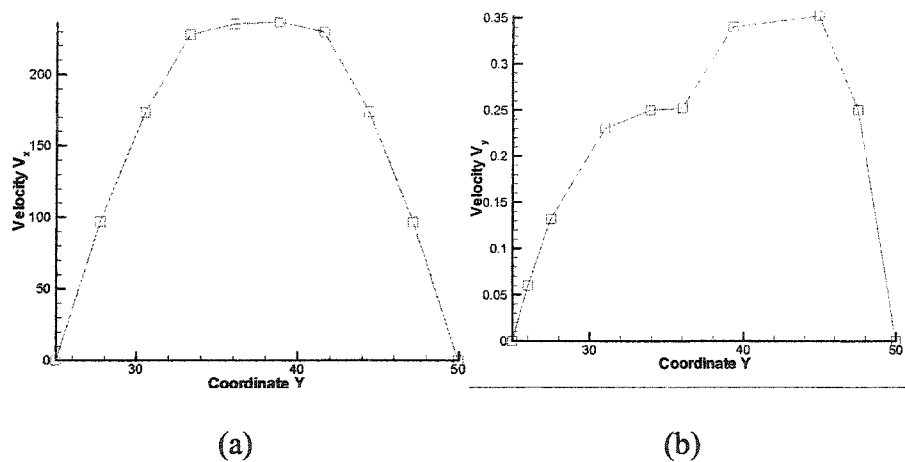


Figure 3.2 Velocity extracted at $x=450\mu\text{m}$ from the straight channel (a)Velocity_x across channel width; (b)Velocity_y across channel width

In order to create a turbulent flow effect, zigzag channels, with the same line width, same inlet flow rate, and same mesh size as that of straight channels, has been carried out in the software simulation. The vector contour and velocity of a zigzag channel are shown in Figure 3.3 and Figure 3.4, the channel steady state velocities in both x and y direction are in the range between $225 \mu\text{m/s}$ and $250 \mu\text{m/s}$. The flow is still in the laminar regime, however, in zigzag channels, the velocity in y direction is dramatically higher than that of the straight channels. Those changes encourage collisions

between the species of the flow, and residence time of the flows increase within the reactor and becomes longer because of the longer flow path of the zigzag channel. There is a sudden jump of velocity around the zigzag corner, which promotes the collisions between the flow species within the channel.

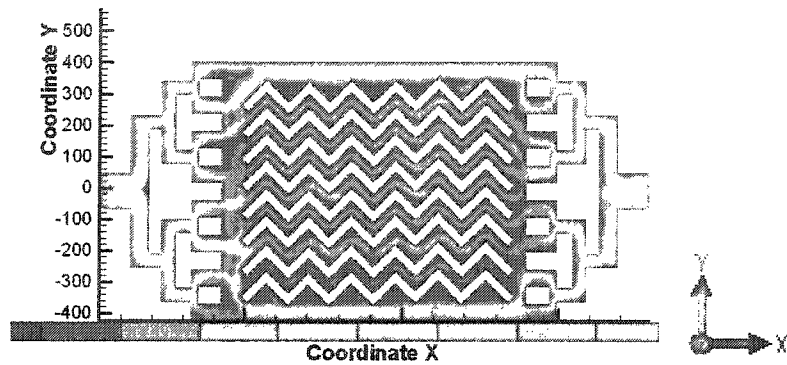


Figure 3.3 2-D Top View Velocity contour of the zigzag channel reactor

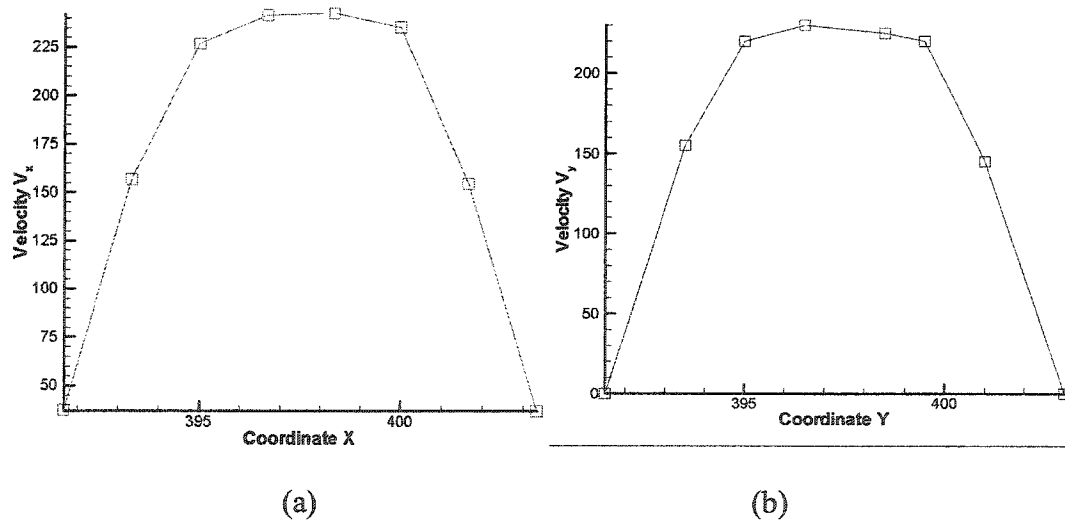


Figure 3.4 Velocity extracted at $x=450\mu\text{m}$ from the zigzag channel. (a)Velocity_x across the channel width; (b)Velocity_y across the channel width

To further improve mixing efficiency, a structure, which is called the omega channel, is created which stretches and tilts the flow in order to intensively increase both the residence time and mixing efficiency of the species in the reactor.

With same boundary condition (inlet flow rate and non-slip wall) and same mesh size as straight and zigzag channel, the flows in the omega channel experience a series of physical processes different from than that for the above circumstances.

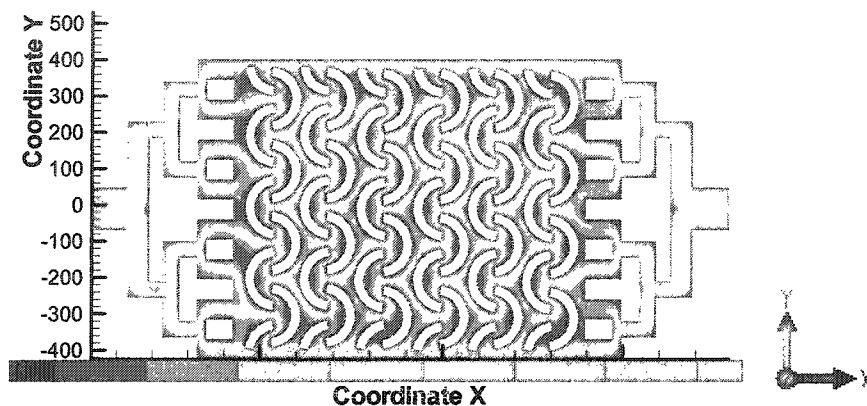


Figure 3.5 2-D top view velocity contour of the omega channel reactor

The omega channel generates dispersion and spreading of mixed fluids that lead to more turbulent collisions, and lower pressure drops than that of the zigzag channel and straight channel.

It can be seen that the flow is converged and split in the omega channels. When the flows are converged together, the flows reach the maximum velocity region. The maximum velocity in x direction is $600 \mu\text{m/s}$ as shown in Figure.3.7 (a), and the velocity in y direction is very low. When the velocity in y direction is low enough, the flows begins to split. Figure 3.7 (b) shows the velocity in the y direction in the maximum velocity (absolute value) region. It can be seen that flows begins to split when the velocity in the x direction reaches its peak.

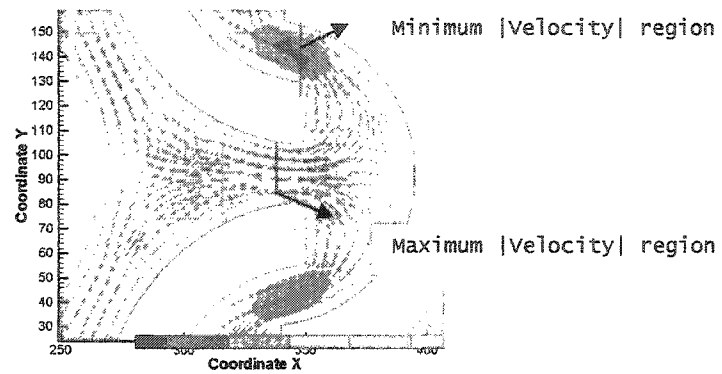


Figure 3.6 Flow regions of the omega channel

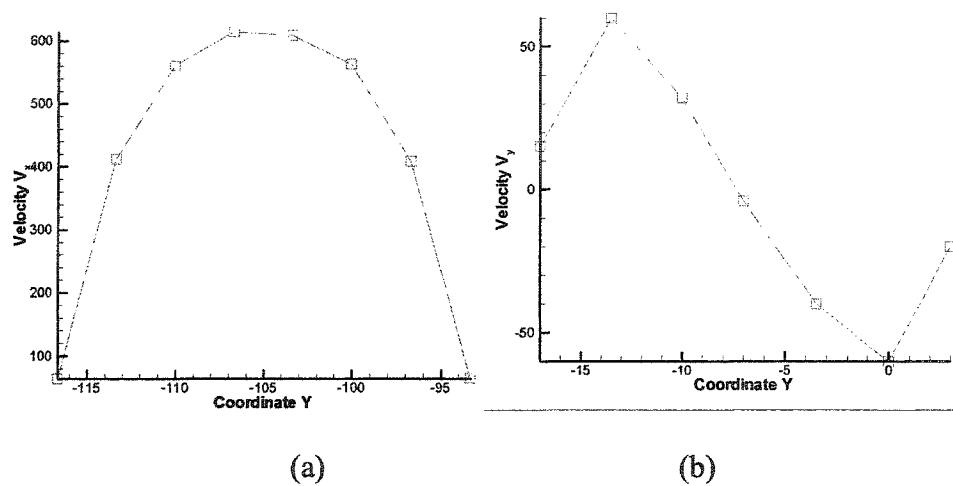


Figure 3.7 Velocity extracted at $x=340\mu\text{m}$ from the omega channel
 (a) Velocity-x of maximum velocity region (b) Velocity-y of maximum velocity region

After the split, the flows generate large back-flow which is led by the structure of the omega channel, this area of the flow reaches the minimum velocity (absolute value) region. Figure 3.8 (a) and (b) shows the velocity of this region. This makes the mean flow velocity comparably low, and therefore, contributes to increasing the resident time of the flows' in the omega channels. This periodical back-flow generates a pressure gradient opposing to the flow, therefore back-flow is the reason that the pressure drop across the omega channels is lower than that of the zigzag and straight channels.

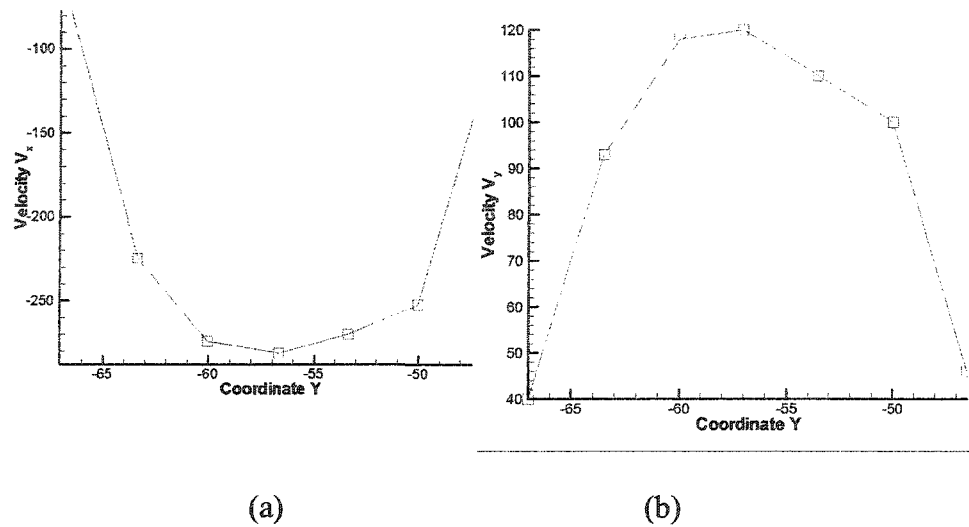


Figure 3.8 Velocity extracted at $x=340\mu\text{m}$ from the omega channel. (a) Velocity-x of Minimum velocity region of omega channel
(b) Velocity-y of Minimum velocity region of omega channel

Figure 3.9 shows the velocities in the x direction of the three sets of channels. It can be seen that the velocity of the zigzag channel in the x direction is almost the same as the straight channel streamwise velocity. This is in agreement with equation 2.12 and 2.16 derived in chapter two. Velocity of the omega channel in the x direction is higher than the other two, due to the obstacle features formed by the omega channel. This high velocity will contribute to the chaotic mixing of the flow species.

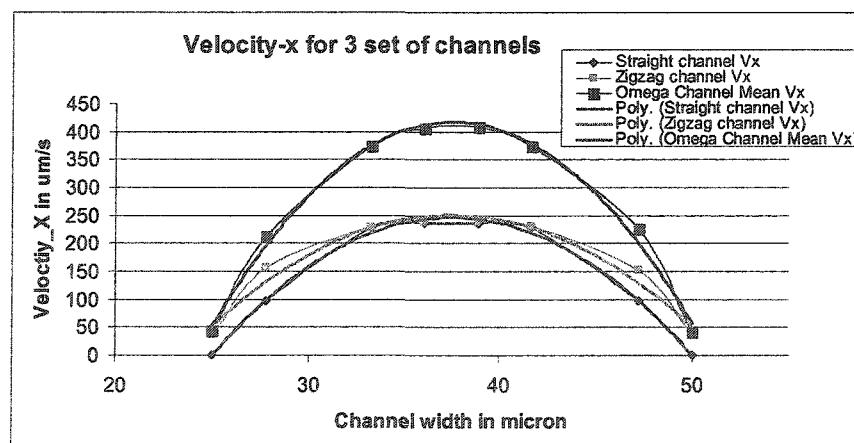


Figure 3.9 Velocity in X direction for 3 sets of channels

The velocities in the x direction are similar for the three sets of reactors. The velocity in the y direction across the three sets of reactors is shown in Figure 3.9. The microchannels are assumed to be low flow rate with no turbulent effect influencing the result. The straight channel part of Figure 3.10 (b) (c) that the obstacle walls of zigzag channel and the discontinuous obstacle walls of omega channel contribute large velocities in y direction.

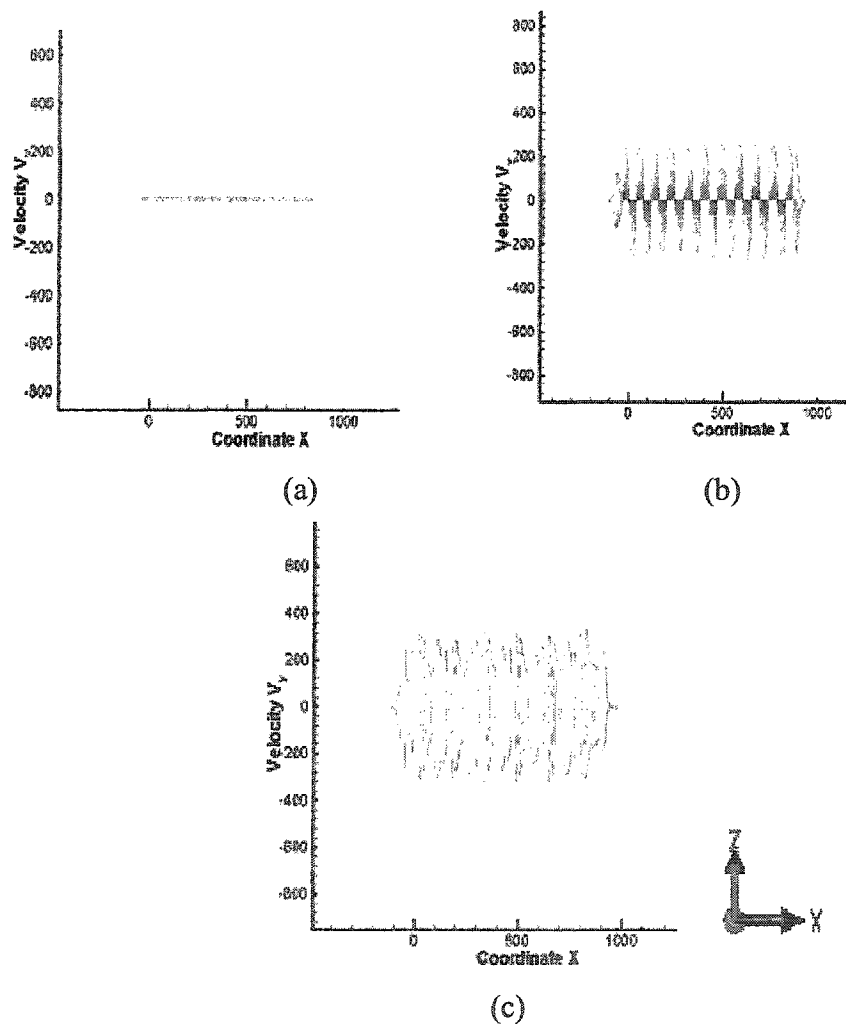


Figure 3.10 2-D Cross-sectional view of velocities magnitude in Y direction for 3 sets of channels (a) Straight channel reactor (b) Zigzag channel reactor (c) Omega channel reactor

The obstacle feature walls generate dispersion and spreading of mixed fluids that lead to more turbulent collisions than plain straight channels. The mean difference between Figure 3.10 (b) and Figure 3.10 (c) can be explained in that discontinuous obstacle feature walls in the omega channel force the fluid elements near the wall to mingle with fluid elements in the centre of the channel which is also the reason for the better mixing efficiency. Based on the above work, and by comparing the velocity profile of several features of the channels, the omega-shaped channels were selected due to the optimum residence time, turbulence phenomena, and better mixing than that of the others. Therefore, an omega channel reactor design is proposed which exhibits a more favorable velocity profile by guiding fluid streams over alternating, turbulence-generating obstacles.

3.3 Mixing of Fluids

A rapid and efficient mixing is an important step in both multicomponent analytical systems and microreaction technology. However, as discussed in chapter two, turbulent flows cannot be generated when the dimensions of the structure are less than hundreds of micrometers. In such dimensions, the flow is strictly laminar and the mixing is entirely driven by molecular diffusion between layers of different concentrations. Consequently, when the thickness of each fluid layer is larger than the characteristic diffusion length, an effective and rapid mixing is difficult to achieve. The diffusion length is often approximated by $\sqrt{4Dt}$ where D is the diffusion coefficient (diffusivity) of the species and t is the mean residence time.

In the laminar flow regime, the mixing chiefly depends on the diffusion process. The lamination mixer needs long enough path and wide space to ensure complete mixing or a complex geometry to raise, stretch, and tilt the fluid interfaces to ensure complete mixing based on chaotic advection. But in regions with high-turbulence levels, the eddy lifetime, k/ϵ , is short, mixing is fast, and, as a result, the reaction rate is not limited by small-scale mixing. In this limit, the kinetic rate usually has the smallest value. On the other hand, in regions with low turbulence levels, small-scale mixing may be slow and limit the reaction rate. In this limit, the mixing rates are more important.

3.3.1 Flow Vorticity

It has been studied that chaotic advection promotes the rapid changes (exponential) that arises either through unsteadiness in the flow, or within the device. We hereby introduce the concept of vorticity in a mixing flow. Vorticity is the curl of the fluid velocity. It is a measurement of the tendency of a vector field to rotate about a point. It indicates how much swirl or shear there is in the flow

It can also be considered as the circulation per unit area at a point in a fluid flow field. It is a vector quantity, whose direction is along the axis of the fluid's rotation. The incensement in vorticity is caused by production due to stretching and turning of the vortex lines [39] Figure. 3.10 (a), (b), and (c) show the vorticity contours of the three sets of reactors. They are analogous to the contours of the velocities in y direction of the three sets of reactors shown in Figure 3.10.

$$\frac{\partial \eta}{\partial t} = -V \cdot \nabla \eta + \eta \frac{\partial v}{\partial y} + \omega_H \cdot \nabla_H v \quad (3.1)$$

Equation 3.1 is the equation of vorticity, the left side term is the local change of vertical vorticity, the right side terms are advection, stretching and tilting terms correspondingly [32][33]. Consequently, It can be stated that vertical velocity differential contributes to the arising of stretching term, and the vertical velocity contributes to tilting term of vorticity. Which explain the analogy of the Figure 3.10 and Figure 3.11.

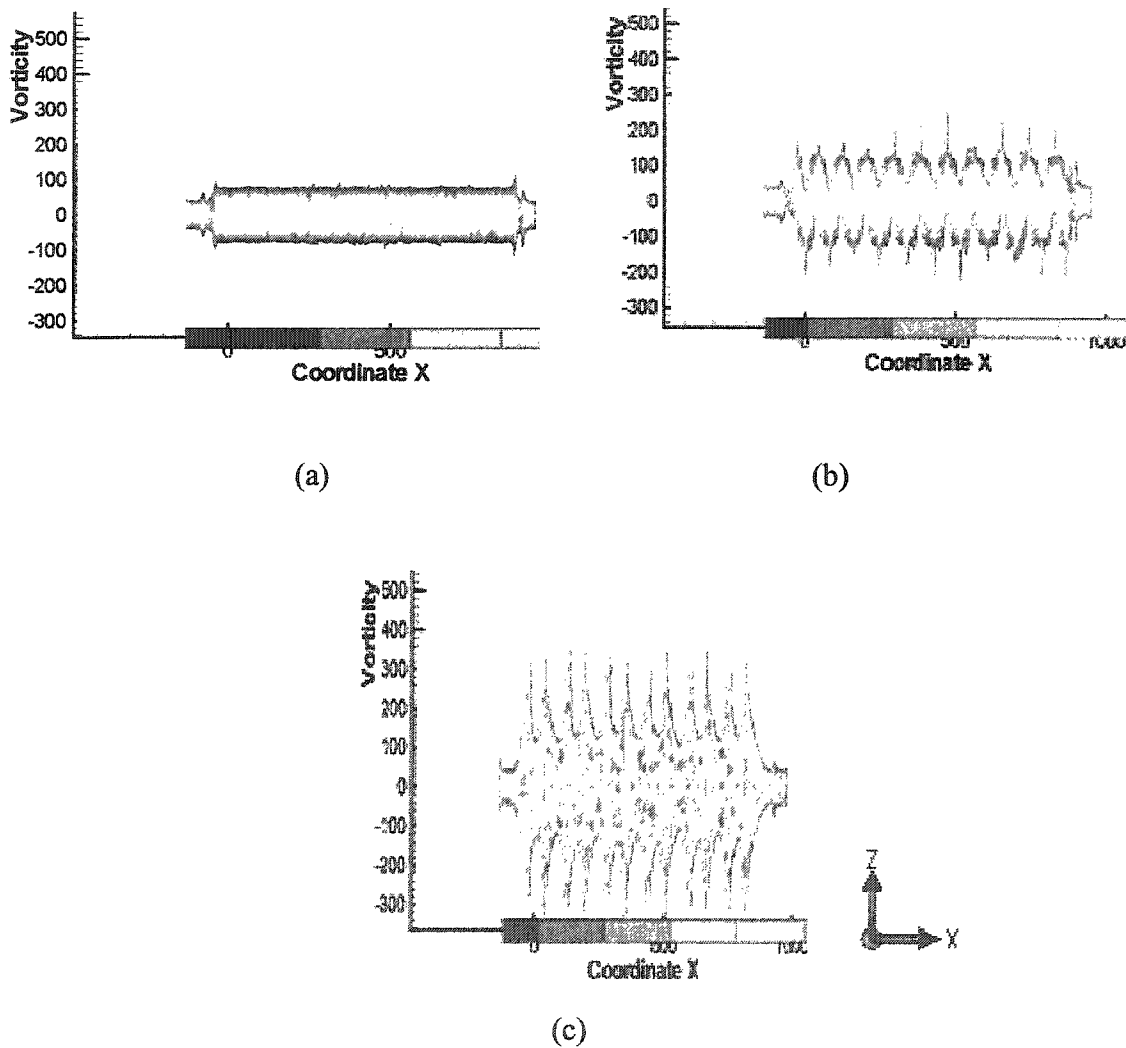


Figure 3.11 2-D Cross-sectional view of vorticities of 3 set of reactors (a) Straight channel reactor (b) Zigzag channel reactor (c) Omega channel reactor

On the other hand, comparing the boundary layers of omega channel, zigzag channel, and straight channel, it can be seen that there is a gradual increase of the separation of the boundary layers in the omega channel which increase the vortices of the flow, thus enhancing mixing performance. The vortices tend to break up the streams into layers and each layer curls in different manner. These breaking and curling actions and the co-mingling of the center streamline and the edge streamline reduce the diffusion between the molecules of two liquids in a mixing process. However, zigzag and straight channel do not have this advantage.

3.3.2 Unsymmetry and Recirculation of the Flows

In the omega channel, the fluids flowing through the channel were rotated as intended. There were critical differences between the low and high Reynolds number flows. As the Reynolds number became higher, fluids were more mixed and the interface of fluids became more distorted. As fluids passed through the omega channels with a helically rotational shape, the fluids were stretched and folded due to the inertial force. This convection widened the interfacial area, which induced rapid mixing of fluids at a higher Reynolds number. In the framework of continuum fluid mechanics, the Reynolds number plays an important role in analyzing the flow field. The degree of mixing arising solely from diffusion under pure laminar flow conditions (1D case) decreased rapidly with increasing velocity, as the residence time is reduced within the channel. As the Reynolds number becomes larger, recirculation occurs in the flow of the omega channel, the streamline turns unsymmetrical, and the pressure in the channel experiences a series of changes as well.

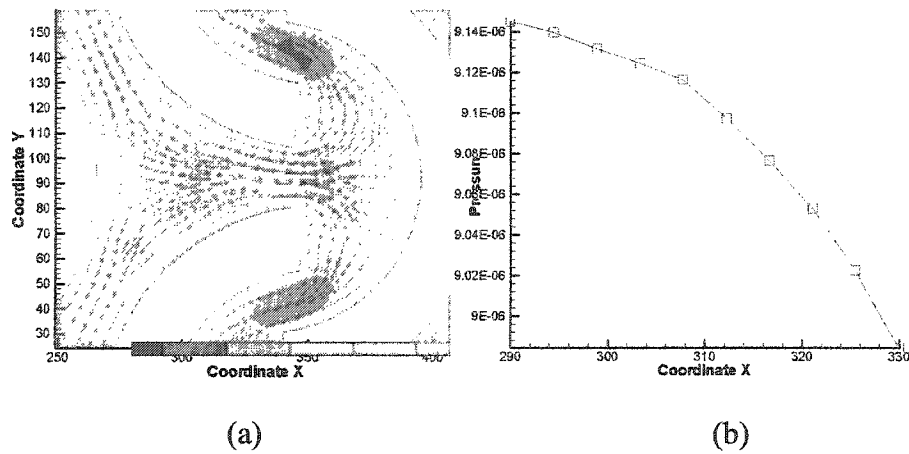


Figure 3.12 Flow in omega channel the Reynolds number=1.27
 (a) Velocity distribution (b) Pressure distribution across omega channel entrance

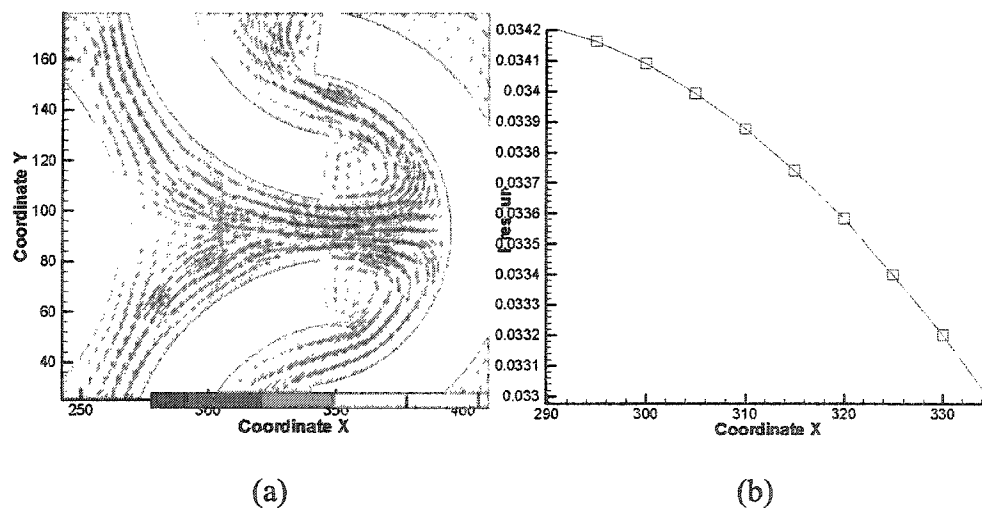


Figure 3.13 Flow in omega channel the Reynolds number=70
 (a) Velocity distribution (b) Pressure distribution across omega channel entrance

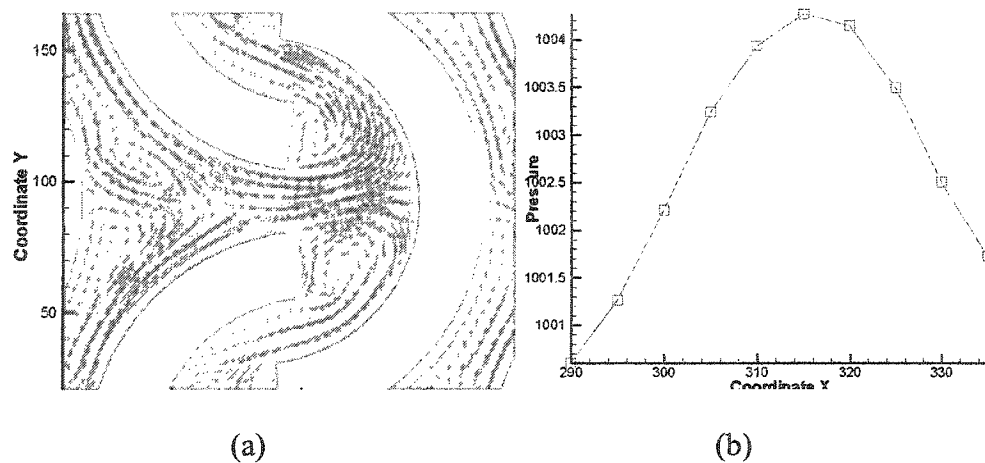
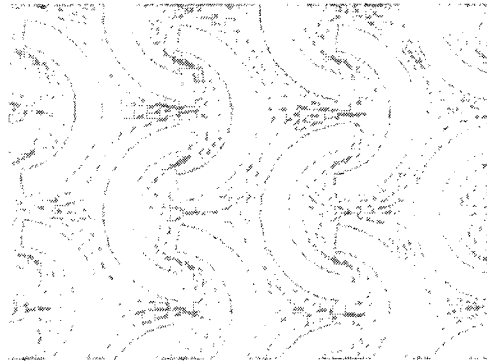
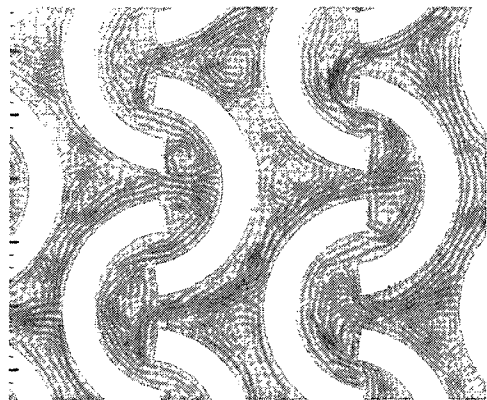


Figure 3.14 Flow in omega channel the Reynolds number $\gg 100$
 (a) Velocity distribution (b) Pressure distribution across omega channel entrance

In Figure 3.12 it can be seen that when the Reynolds number is low, diffusion is dominant in the mixing, and pressure drops nonlinearly as the fluid flows out. There is almost no chaotic mixing. As the Reynolds number increases, flow passes through the omega channels with a rotational shape, the flow becomes re-circulated, and this convection makes the flow streamline stretched and folded. Figure 3.13 suggests that there are some vertexes that appear in the omega channel. If the Reynolds number increases further, (ie $Re \gg 100$) the recirculation keeps accumulating to a point that some of the spots generate back-flow phenomena, as shown in Figure 3.14 (b). At the entrance of the omega channel, the pressure of the flow no longer drops as it flows out as shown in Figure 3.14 (b). Instead of the pressure decreasing, it increases, reaching a maximum value and then dropping to a value that is higher than the initial point, as shown in Figure 3.15 (b). The recirculation is the reason for the negative pressure gradient and is also the reason for the mixing improvement at high Reynolds number.



(a)



(b)

Figure 3.15 Flow in mega channel (a) Symmetrical flow
(b) Unsymmetrical recirculation

The enhancement of mixing efficiency can be further illustrated in Figure 3.15, where the flow streamlines are re-circulated and unsymmetrical. When mixing is effective, diffusion processes are greatly accelerated; material that is near the wall goes into the bulk and vice versa, thereby eliminating a slowdown due to diminishing concentration gradients.

3.3.3 Discussion of Results

Mathematical flow model of the omega channel derived in chapter two shows that the pressure distributions in the entrance of the omega channel are nonlinear. This nonlinear pressure distribution means a lower pressure drop than the linear pressure in the

straight and zigzag channels, which enable the species of the flows to utilize the mixing volume and superior dispersion of species with the lower pressure drop. The CFD simulation shows that the omega channel reactor produces a lower pressure drop across the reactor which is in agreement with the mathematical model and simulation.

In the omega channel, the fluid near the wall will co-mingle with fluid elements in the centre of the channel. This mingling of centre streamlines and boundary streamlines is periodically enforced by the omega channel in the reactor, therefore mixing is improved. A gradual increase of the separation of boundary layers in the omega channel helps generate more vortices. Those vortices tend to break up the streams into layers and each layer curls in different manner [42]. These breaking and curling actions and the co-mingle of center streamline and the edge streamline reduce the diffusion between the molecules of two liquids in a mixing process. However, zigzag and straight channel do not have this advantage.

At high Reynolds number, unsymmetrical and recirculation flow phenomena appears, which leads to a negative pressure gradient and, consequently, increases the mixing performance of the flow species. By eliminating the parabolic velocity profile characteristic of laminar flow in the omega channel, the vertical element of velocity promotes stirring in the mixing processes. The back-mixing provides uniform distribution and optimum residence time. The convection mixing action of the elements rapidly eliminates temperature gradients, reducing fouling and thermal degradation.

CHAPTER 4

STOCHASTIC MODELING

4.1 Markov Chain Approach

Stochastic approaches have been widely employed for simulating flow in reactors because of their probabilistic nature [43] [45]. In such approaches, fluid flow is considered as a Markov process with a continuous or discrete time parameter, and with countable states. Markov Chains have a wide range of applications. They can be applied to many physical phenomena, such as diffusion, chemical reactions, and flow systems among others. The main reason for predicting fluid flow properties using a stochastic approach is that flow is probabilistic and transient in nature. In this study, our modeling approach is to divide the microreactor into compartments or states and to treat it as a Markov chain with transitions between compartments or states.

A Markov chain is defined as a sequence of random variables $\{X_n, n=0,1,\dots\}$ in which, for every collection of integers $(n=0,1,\dots)$, the conditional distribution of X_{n+1} satisfies the relation :

$$\Pr\{X_{n+1}=i \mid X_0, X_1, \dots, X_n\} = \Pr\{X_{n+1}=i \mid X_n\} \quad (4.1)$$

Where $\Pr\{X_{n+1} = i \mid X_0, X_1, \dots, X_n\}$ represents the probability that the future state $X_{n+1} = i$ given all previous states (X_0, X_1, \dots, X_n) ; and $\Pr\{X_{n+1} = i \mid X_n\}$ represents the probability of the future state $X_{n+1} = i$ given the previous state (X_n) . Thus, given the knowledge of a present state (X_n) , the outcome in the future $(X_{n+1} = i)$ is no longer dependent upon the past $(X_0, X_1, \dots, X_{n-1})$ [46].

For each $X_\alpha, \alpha \in (0, 1, \dots)$, the probability that the system is in state i_α at time or step α , is denoted by:

$$\Pr\{X_\alpha = i_\alpha\} = p_{i_\alpha}, \quad (4.2)$$

is p_{i_α} . Also, for every pair of random variables $X_\alpha, X_\beta, \alpha, \beta \in (0, 1, \dots)$, the conditional probability is:

$$\Pr\{X_\beta = i_\beta \mid X_\alpha = i_\alpha\} = p_{i_\alpha i_\beta}, \quad (4.3)$$

with the condition that:

$$\sum_i \Pr\{X_\alpha = i_\alpha\} = \sum_{i_\alpha} p_{i_\alpha} = 1. \quad (4.4)$$

Therefore, we have that $\sum_{i_\beta} p_{i_\alpha i_\beta} = 1$. In using a Markov chain to describe a stochastic system, all possible values of the random variable, constitute the state space of the system. The conditional probability in (4.3) describes a transition from state i_α at time α to state i_β at time β . The direction of the transition from i_α to i_β in the chain is denoted by the order of the subscripts in $p_{i_\alpha i_\beta}$. Let $P(0)$ denote the initial distribution vector, $P(0) = [p_1(0) p_2(0) \dots p_l(0)]$. The distribution after one transition is given by

$p_j(1) = \sum_{i=1}^l p_i(0)p_{ij}(1)$. In matrix form it is expressed as $P(1) = P(0)P(1)$, similarly,

$P(2) = P(1)P(2) = P(0)P(1)P(2)$, In general, we have :

$$P(n) = P(0) \prod_i^n P(i) \quad (4.5)$$

Equation (4.5) indicates that each state of the Markov chain is completely determined by the initial probability distribution and the transition probabilities.

A Markov chain is said to be homogeneous with respect to time (the transition probabilities are not functions of time, α) if the transition probability can be expressed as:

$$\Pr\{X_{\alpha+1} = j | X_{\alpha} = i\} = p_{ij} \quad (4.6)$$

In any case, the transition probabilities p_{ij} can be arranged in the form of a matrix:

$$P = \begin{bmatrix} p_{11} & p_{12} & p_{13} & \dots \\ p_{21} & p_{22} & p_{23} & \dots \\ \cdot & \cdot & \cdot & \dots \end{bmatrix} \quad (4.7)$$

when the transition probabilities are homogeneous over time, the corresponding probability vector at any state n, $P(n)$ in equation (4.5) reduced to:

$$P(n) = P(0)P^n \quad (4.8)$$

The state space matrix P is known as a stochastic matrix (also called transition probability matrix) with the transition probabilities p_{ij} 's as their elements. Note that the elements in each row of the matrix sum to unity [46].

4.2 Model Formulation and Probability Transition Matrix

The mathematical formulation of the model is based on modeling the axial position of a molecule over time by means of a Markov chain. The probability distribution of the axial position of the molecule at a given time-step n depends only on its position at time-step $n-1$ and a set of transition probabilities. The transition probabilities are quantified in accordance with the molecule transport process.

Using the Markov chain approach, we model the residence time of fluid flow in the three sets of microreactors- omega channel, zigzag channel, and straight channel. Of particular interest is the omega channel, because the CFD simulation with Coventor from section 3.2 and 3.2 has shown a dominant mixing advantage of the omega channel over that of the other two. A Markov chain model is an analytical approach to predicting the residence time distribution in the three microreactors considered. This approach will not only characterize and compare the efficiency of the three microreactors, but will validate also the conclusions drawn from the CFD simulation.

The fluid flow in the microreactor contains a mixture of molecules, M_j , $j = 1, 2, \dots, n$. A molecule is regarded as an “entity” in the flow system. A molecule at position j is regarded as the “entity” at state j , and the motion of molecules in the flow is viewed as a transition of the “entities” from one state to another. Consequently, the collection of all transitions of the “entities” form a Markov chain. Let the states of the system at time $n\Delta t$ define the state space of the random variable $X(n)$ and let $p_{ij}(n, n+1)$ be the one-step transition probability that an “entity” at state i at time $n\Delta t$ will be at state j at time $(n+1)\Delta t$ inside a microreactor. Therefore, from (4.6), we have:

$$\Pr\{X(n+1) = j \mid X(n) = i\} = p_{ij}(n, n+1) \quad . \quad (4.9)$$

The one-step transition probabilities of this Markov chain can be expressed in the following matrix form:

$$P(n,n+1) = \begin{bmatrix} p_{11}(n,n+1) & p_{12}(n,n+1) & \cdots & p_{1l}(n,n+1) & p_{1d}(n,n+1) \\ p_{21}(n,n+1) & p_{22}(n,n+1) & \cdots & p_{2l}(n,n+1) & p_{2d}(n,n+1) \\ \vdots & \vdots & \vdots & \vdots & \vdots \\ p_{l1}(n,n+1) & p_{l2}(n,n+1) & \cdots & p_{ll}(n,n+1) & p_{ld}(n,n+1) \\ 0 & 0 & \cdots & 0 & 1 \end{bmatrix} \quad (4.10)$$

where l is the total number of transient states in the Markov chain and D is the exiting (or absorbing) state. Once a molecule enters state D at time n , it will not be able to return to the microreactor. Note that there are a finite number of states in this Markov chain [46][47].

In order to represent a microreactor by a Markov chain, one needs to divide the microreactor space into a set of nonoverlapping compartments and calculate the transition probabilities between any two compartments. If one considers the whole microreactor space, one would have a very large number of compartments which will make the computations prohibitive. Since the interest is in comparing the residence time of the three reactor types, this was accomplished by considering, without loss of generality, Markov chains for the three types that encompass a small number of states. For each microreactor type, four Markov chains were formulated. (1) 1x1 (one compartment in the axial direction and one in the radial direction), (2) 1x3 (three compartments in the axial direction and one in the radial direction), 2x2 (two compartments in each direction), and (4) 2x3 (three in the axial direction and two in the radial direction). Figure 4.1 presents a schematic diagram of all states and transitions between states for the Markov chain of the omega type.

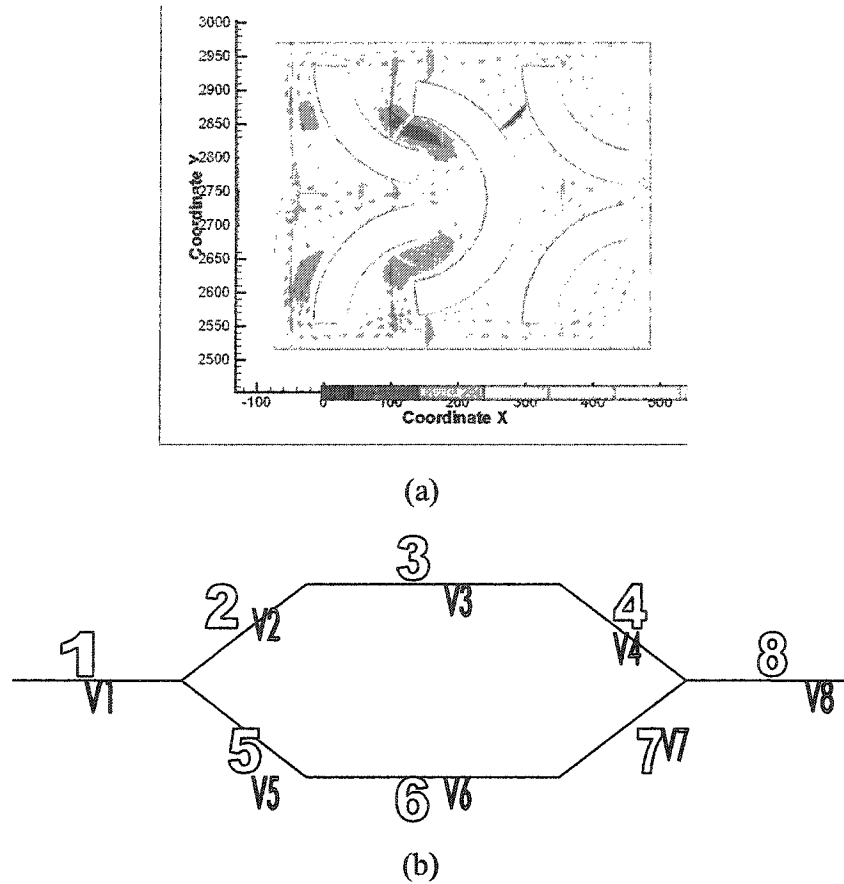


Figure 4.1 (a) Velocity contour for compartment 1x1 omega channel. (b) Schematic diagram of all states and transitions between states for the Markov chain for compartment 1x1 omega Channel

There are $l = 8$ states or compartments in a 1x1 omega channel microreactor, and $l = 6$ states in that of zigzag and straight channel microreactors.

The process of generation of the transition probability matrix for a 1x1 honeycomb (omega channel) microreactor was as follows:

The probabilities that a molecule in state 1 at time $n\Delta t$ will be in state 2 or state 5 at time $(n+1)\Delta t$ are $P_{12}(n+1) = \mu_{12}$ and $P_{15}(n+1) = \mu_{15}$, where $\mu_{12} = \frac{(V_1/l_1)\Delta t}{2}$ and

$$\mu_{15} = \frac{(V_1/l_1)\Delta t}{2}.$$

The probability that a molecule in state 2 at time $n\Delta t$ will be in state 3 at time $(n+1)\Delta t$ is: $P_{23}(n+1) = \mu_{23}$, where $\mu_{23} = (V_2/l_2)\Delta t$.

The probability that a molecule in state 3 at time $n\Delta t$ will be in state 4 at time $(n+1)\Delta t$ is: $P_{34}(n+1) = \mu_3$ where $\mu_{34} = (V_3/l_3)\Delta t$.

The probability that a molecule in state 5 at time $n\Delta t$ will be in state 6 at time $(n+1)\Delta t$ is: $P_{56}(n+1) = \mu_{56}$ where $\mu_{56} = (V_5/l_5)\Delta t$.

The probability that a molecule in state 6 at time $n\Delta t$ will be in state 7 at time $(n+1)\Delta t$ is: $P_{67}(n+1) = \mu_{67}$ where $\mu_{67} = (V_6/l_6)\Delta t$.

The probability that a molecule in state 4 or state 7 at time $n\Delta t$ will be in state 8 at time $(n+1)\Delta t$ are $P_{48}(n+1) = \mu_{48}$ and $P_{78}(n+1) = \mu_{78}$ where $\mu_{48} = (V_4/l_4)\Delta t$ and $\mu_{78} = (V_7/l_7)\Delta t$.

The probability that a molecule in state 8 at time $n\Delta t$ will be in the existing state at time $(n+1)\Delta t$ are $P_{8D}(n+1) = \mu_{8D}$, $\mu_{8D} = (V_8/l_8)\Delta t$

Having the volumetric flow rate = 0.1 sccm (which is the lowest flow rate we could monitor from the experimental system) as the initial condition, $V_1 \dots V_8$ correspond to average velocities at state 1...8, which was obtained from the CFD simulation of flow in the one compartment omega channel microreactor with the Microfluidic Analysis Module of CoventorWare software (Coventor, Inc.). $l_1 \dots l_8$ are the lengths corresponding to $V_1 \dots V_8$.

The probability that a molecule transits form one state to a non-adjacent state is zero. Once a molecule enters state D (which is the exit state outside the reactor) at time $n\Delta t$, it will not be able to return to the microreactor. Therefore, the probability that

molecules in state D at time $n\Delta t$ will be in any state i in the microreactor at time $(n+1)\Delta t$

is : $P_{di}(n\Delta t, (n+1)\Delta t) = 0, i = 1, 2, \dots, 8$.

The probabilities that a molecule at state i ($i = 1, 2, \dots, 8$) remains in the same state are:

$$\begin{aligned} P_{11}[(n+1)\Delta t] &= 1 - (P_{12} + P_{15}), P_{22}[(n+1)\Delta t] = 1 - P_{23}, P_{33}[(n+1)\Delta t] = 1 - P_{34}, \\ P_{44}[(n+1)\Delta t] &= 1 - P_{45}, P_{55}[(n+1)\Delta t] = 1 - P_{56}, P_{66}[(n+1)\Delta t] = 1 - P_{67}, \\ P_{77}[(n+1)\Delta t] &= 1 - P_{78}, \text{ and } P_{88}[(n+1)\Delta t] = 1 - P_{8d} \end{aligned}$$

Therefore the one-step transition probability matrix for the molecule in the one row by one column or 1x1 compartment omega channel can be expressed as:

$$P(n, n+1) = \begin{bmatrix} 1 - (\mu_{12} + \mu_{15}) & \mu_{12} & 0 & 0 & \mu_{15} & 0 & 0 & 0 & 0 \\ 0 & 1 - \mu_{23} & \mu_{23} & 0 & 0 & 0 & 0 & 0 & 0 \\ 0 & 0 & 1 - \mu_{34} & \mu_{34} & 0 & 0 & 0 & 0 & 0 \\ 0 & 0 & 0 & 1 - \mu_{45} & 0 & 0 & 0 & \mu_{48} & 0 \\ 0 & 0 & 0 & 0 & 1 - \mu_{56} & \mu_{56} & 0 & 0 & 0 \\ 0 & 0 & 0 & 0 & 0 & 1 - \mu_{67} & \mu_{67} & 0 & 0 \\ 0 & 0 & 0 & 0 & 0 & 0 & 1 - \mu_{78} & \mu_{78} & 0 \\ 0 & 0 & 0 & 0 & 0 & 0 & 0 & (1 - \mu_{8D}) & \mu_{8D} \\ 0 & 0 & 0 & 0 & 0 & 0 & 0 & 0 & 1 \end{bmatrix} \quad (4.11)$$

This is a so-called stochastic matrix: a square matrix with nonnegative entries giving transition probabilities, and row sums all equal to 1. Similarly, one can obtain the transition probability matrices for the 1x1 zigzag and straight channel reactors. Using the same approach, one can obtain transition probability matrices for the 1x3, 2x2, and 2x3 reactors within each type [46].

4.3 Cumulative Probability Computation

We use the Markov chain approach to study and compare different characteristics of the microreactors. In order to convert the time steps n ($n= 1,2,3,4\dots$) of a discrete time Markov chain into real time, we multiplied n by a small time increment Δt . A value of $\Delta t = 0.00319$ millisecond was chosen for these calculations. This value was taken to be 1/1000 of the average residence time, calculated approximately as the flow rate divided by the volume of the reactor. This was deemed accurate since taking a smaller Δt did not change the results.

As such, Δt is the step-size of the Markov chain and the real time is $t = n\Delta t$, where n is the number of steps. Therefore, the probability that a molecule is in any state i at step n can be calculated from Eq. (4.8). Of interest is $P_{ID}(t)$ or the probability that a molecule starting at state 1 at time 0 is in state D (or exits the reactor) at time t . Since state D is an absorbing state, the chain is transient, which means that $P_{ID}(t)$ approaches 1 as t approaches infinity [47]. The probability $P_{ID}(t)$ is then the cumulative probability of residence time calculated over the time interval $(0,t)$. Therefore, the probability density function for residence time can be expressed as:

$$f(t) = \frac{P_{ID}(t + \Delta t) - P_{ID}(t)}{\Delta t} \quad (4.12)$$

Where $t = 0, \Delta t, 2\Delta t, \dots, n\Delta t$, and Δt is the step-size. $f(t)\Delta t$ is the probability of a molecule exiting the reactor between t and $t + \Delta t$. One can plot the probability density function $f(t)$ vs t from equation (4.12).

The graphs of $P_{1D}(t)$ vs t for different compartments with 3 sets of microreactors are shown in section 4.5. The graphs of the density function $f(t)$ vs t for different compartments with 3 sets of microreactors are shown in section 4.5 as well.

4.4 Mean and Variance of Time Until Exit

In the Markov chains considered, state D is an absorbing state and the other states are classified as transient. A Markov chain that has one or more absorbing states is said to be an absorbing Markov chain. In a finite absorbing Markov chain, no matter where the process starts, the probability after n steps that the process is in the absorbing state tends to 1 as n tends to infinity.

Let the submatrix Q contain the transient states in the matrix form of equation (4.10) and let matrix I be the n -by- n identity matrix. We define the fundamental matrix to be $N=(I-Q)^{-1}$. Let n be the function giving the number of steps in which the process is in a transient state. Then, the expected values of n is expressed as:

$$\{M_i[n]\} = N\xi \quad (4.13)$$

Where ξ is the unity vector. Here, $N\xi$ gives the row sums of N . If we denote $N\xi$ by τ , then the variance of n is expressed as:

$$\{\text{Var}_i[n]\} = 2(N-I)\tau - \tau_{sq} \quad (4.14)$$

where τ_{sq} is the square of τ [47].

The mean and variance of the number of steps that a molecule stays in any compartment or transient state i in the reactor can be calculated from equation (4.13) and

(4.14). Since, a molecule starts in state 1 and exists in state D, The first value in the vector $\{M_i[n]\}$, noted as $M(n)$, is the mean number of steps until exit. When multiplied by Δt , this gives the mean residence time in the reactor. Likewise, the first value in the vector $\{\text{Var}_i[n]\}$ will be the variance of the number of steps until exit [47]. When multiplied by $(\Delta t)^2$ this gives the variance of time until exit or the residence time. As a consequence, the mean of the residence time is:

$$\text{Mean (resident time)} = M(n)\Delta t, \quad (4.15)$$

and the variance of residence time is:

$$\text{Variance (resident time)} = \text{Var}(n)\Delta t^2 \quad (4.16)$$

4.5 Markov Chain Simulation Results

Four different compartments, one row by one column(1x1), one row by three columns(1x3), two rows by two columns(2x2), and two rows by three columns(2x3) of the omega channel reactor, zigzag channel reactor, and straight channel reactor were investigated by the Markov chain approach in terms of probability of exit, mean and variance of residence time, and residence time distribution.

The number of iterations n , the step size Δt and time $t = n\Delta t$ used in the simulation results are presented in Table 4.1.

Table 4.1 Parameters Used in the Simulation of Results

Compartment Type	Time - t (msec)	Step size- Δt (msec)	Iteration Number-n
1x1	3.1941	0.0031941	1000
1x3	6.5793	0.0031941	2060
2x2	8.7648	0.0031941	2745
2x3	11.952	0.0031941	3741

From the Markov chain approach, series of cumulative probabilities $P_{1D}(t)$ for the reactors were calculated with Matlab. The graphs of $P_{1D}(t)$ vs t in Figure 4.2 represents one row by one column(1x1) compartments for different reactor types, omega channel, zigzag channel, and straight channel reactor.

Figure 4.2 exhibits the property of an absorbing Markov chain in the sense that $P_{1D}(t)$ approaches 1 as t approaches infinity. There are three different lines in the plot. From top to bottom, the three lines represent the cumulative probability curves, $P_{1D}(t)$, of a molecule exiting the straight channel compartment ($P_{1D}(t)_{straight}$), a molecule exiting the zigzag channel compartment ($P_{1D}(t)_{zigzag}$), and a molecule exiting the omega channel compartment ($P_{1D}(t)_{omega}$) at a corresponding time t . It can be seen from Figure 4.2 that at time t , $P_{1D}(t)_{straight} > P_{1D}(t)_{zigzag} > P_{1D}(t)_{omega}$. The corresponding omega channel is shown in Figure 4.1. As expected, a molecule in the omega channel will take on average the longest time to exit the reactor among the three sets of reactors. This reinforces the prediction we made in chapter three.

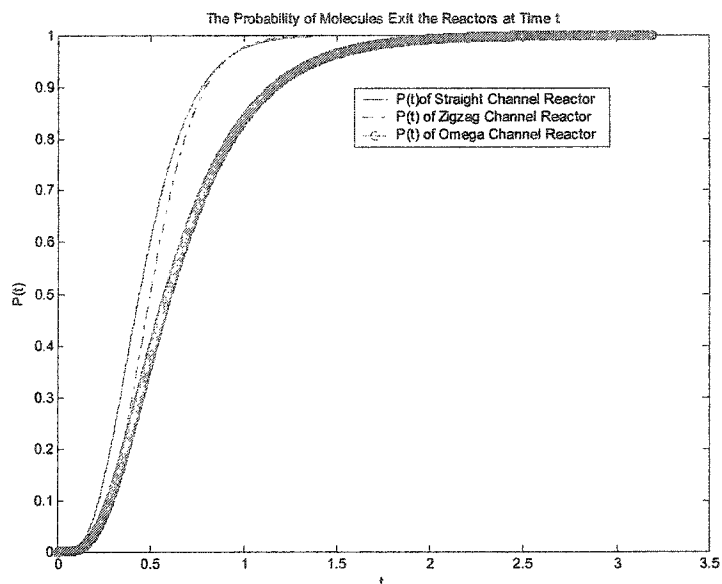


Figure 4.2 Cumulative probability of a molecule exiting the three microreactors with compartment 1x1

It can be seen that, in all three sets of microreactors, the probability curves shift to the right as the number of compartments increases. This shift increases as more compartments are introduced and is most pronounced in the case of the omega reactor. These results give a meaningful guide in designing the configuration of the microreactor.

The above results indicate that the omega channel reactor has a higher mean residence time than the other reactors. This tends to agree with the earlier observation in chapter three that the omega channel type has a much greater mixing efficiency than that of the other two types, suggesting that a higher reaction conversion can be obtained from this prototype microreactor.

Table 4. 2 Mean and variance of time till exit for different compartments with 3 sets of microreactors

Compartment Type	Straight		Zigzig		Omega	
	Mean (msec)	Variance (msec)	Mean (msec)	Variance (msec)	Mean (msec)	Variance (msec)
1x1	0.4848	0.04968	0.5339	0.0406	0.6822	0.1399
1x3	1.2393	0.12023	1.3919	0.1098	2.3374	0.4737
2x2	2.2229	0.56825	2.5333	0.57635	3.2888	1.5849
2x3	4.9257	2.11710	6.6790	2.0663	7.7009	6.4687

The mean and variance of the residence time until exit for the different types of microreactors with four different compartments are calculated from equations (4.15) and (4.16), and the results are listed in Table 4. 2.

From equation (4.12), $f(t)dt$ is the probability of a molecule exiting the reactor between t and $t + \Delta t$, which can be expressed as:

$$f(t)dt = \Pr[t \leq T \leq t + \Delta t] \quad (4.17)$$

where T is the random variable representing residence time. $f(t)$ is the residence time density function, and is expressed as:

$$f(t) = \frac{P_{1D}(t + \Delta t) - P_{1D}(t)}{\Delta t} \quad (4.18)$$

$f(t)$ has the property that the sum of all the probabilities of a molecule exiting the reactor at time t is one as n (the number of steps) tends to infinity, and can be expressed as:

$$\int_0^{\infty} f(t)dt = 1 \quad (4.19)$$

Figure 4.3 shows the simulation results (for 1x1 compartments) of the probability density function for the residence time as calculated from equation (4.12)

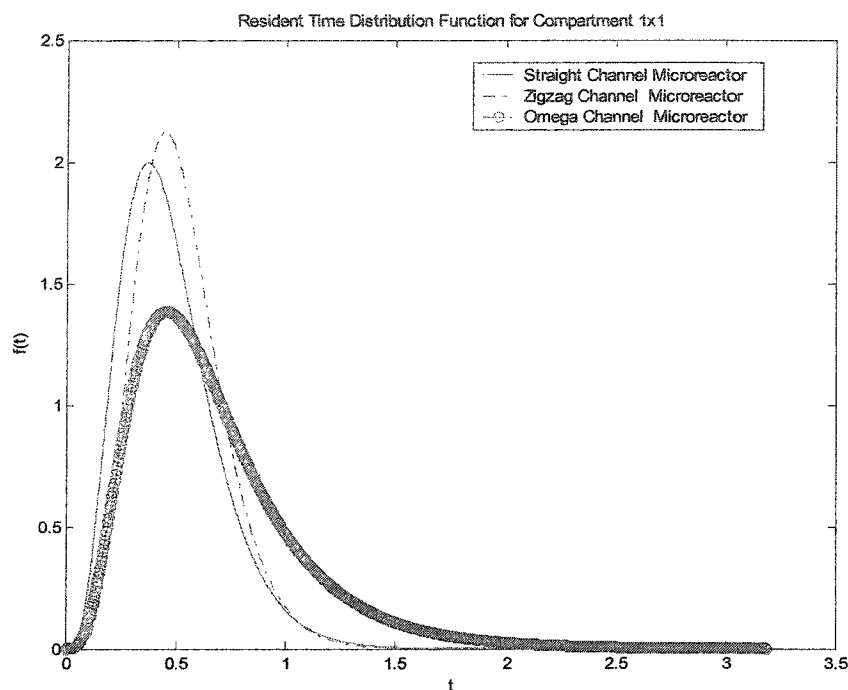


Figure 4.3 Residence time distribution of the three microreactors with compartment 1x1

From these Figures, it is easy to see that the omega channel microreactor has a higher mean residence time than the other two microreactors and also the largest variance of the residence time due to the fact that omega microreactors contain flows with turbulent tendency or back mixing.

It is clear from these results that the Markov chain modeling approach is a powerful method for characterizing the flow properties or residence time of different microreactors in order to study their efficiencies as related to conversion in a chemical reaction system.

CHAPTER 5

MICROREACTOR FABRICATION, CATALYST PREPARATION, AND REACTION TESTING SYSTEM

5.1 Fabrication Process

Advanced micromachining technologies are the foundation of the microreactor fabrication process. The process of optical lithography involves a series of photomasks that have been developed from a series of templates of the design chart, and each lower level template is designed coherently with the upper level one, in order to fulfill the total concept of the three-dimensional MEMS structure.

5.1.1 Photolithography

Pattern Design: Three types of microreactors have been used in this study: straight channel and zigzag channel, and Ω shaped channel. The out perimeter dimensions are 3.1 cm long and 1.6 cm wide.

According to the above simulation for the microreactor, we used the Ω shaped channel as the reactor channel, and also adopt a “binomial tree” inlet and outlet to maximize the reactant mixing result as discussed in chapter 3. The pattern for the Ω shaped channel reactor is designed in CAD file, and is shown in Figure 5. 1.

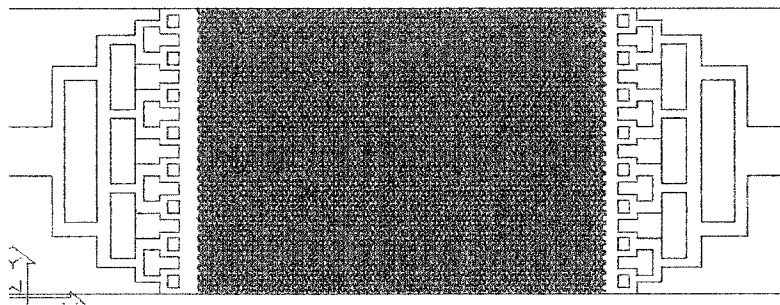


Figure 5. 1 Pattern for Ω shaped channel microreactor

Pattern Generation: Mask pattern generation systems use precision lasers or electron beams to "write" or "pattern" each layer of a semiconductor chip's design onto a plate of chrome-coated quartz glass (called a photomask). The completed mask allows light to pass through the open patterned areas.

After a series of masks is completed, microlithography equipment, such as an aligner or a stepper, projects light through each mask to transfer each layer of a chip's design onto the wafer. As many as 30 masks are needed to build a device in the semiconductor industry, with each new electronic design requiring a unique set of masks.

The process begins when a verified design is translated into GDSII format that is then given to a mask-maker. Mask data preparation software converts the GDSII design data into a format that describes the pattern to be written by a laser or electronic beam (e-beam).

The laser pattern generator uses a raster scan writing strategy. The stage moves at a constant speed along the X axis and a deflector deflects the laser beam along the Y axis creating sweeps. This is repeated until the end of the pattern in the X direction, creating a scan strip along the X axis. After completing a scan- stripe the stage retraces in X and moves to the next Y position for the next scan- stripe. This process is repeated until the entire pattern area has been covered. During the scan sweeps, the laser beam is modulated

according to the pattern data via a modulator. The modulator combines digital and analog modulation, which creates an address grid much finer than the distance between adjacent sweeps, boosting the effective data rate.

The laser or e-beam writes the pattern onto a layer of photosensitive resist that has been added over a chrome layer on top of a blank mask. After exposure, the exposed resist is developed, which clears away and uncovers the underlying chrome only where the pattern is desired. The bared chrome is then chemically etched through. After etching, the remaining resist is completely stripped away, leaving the image as transparent patterns in the otherwise opaque chrome film.

Photolithography Processes: The implementation of microreactor fabrication involves three chrome photomasks for pattern transfer: microchannels, inlets and outlets, and the remaining one for go-through vias. The patterns (with 8 reactors on each pattern) on the photomasks were then transferred onto <100> oriented 450 μ m thickness Si wafer by standard photolithographic techniques. A front side alignment and a backside alignment were performed with the mask aligner tool. Twice etching steps were performed using an Inductively Coupled Plasma etching facility. The channel widths were varied from 5 μ m to 50 μ m, and the depth from 50 μ m to 200 μ m. The channel shapes varied from straight, zigzag, column, sine, and omega. The front side alignment assured that the channels are well aligned with the inlets and outlets, and the backside alignment method assured that the go-through vias, which led the fluids in and out, were etching completely through to make the connections with the inlets and outlets of the microreactor. The front side and backside misalignment is within 1~2 microns. Fundamental optical lithography includes the following steps:

Photoresist Coating: In the first step, the wafers are chemically cleaned to remove particulate matter on the surface as well as any traces of organic, ionic, and metallic impurities. After cleaning, silicon dioxide, which serves as a barrier layer, is deposited on the surface of the wafer. After the formation of the SiO₂ layer, photoresist is applied to the surface of the wafer. High-speed centrifugal spinning of silicon wafer substrates is the standard method for applying photoresist coatings in IC manufacturing. This technique, known as "Spin Coating," produces a thin uniform layer of photoresist on the wafer surface. The spin coat parameters vary from photoresist to photoresist. Figure 5. 2 shows the coating parameters for photoresist Shipley1813.

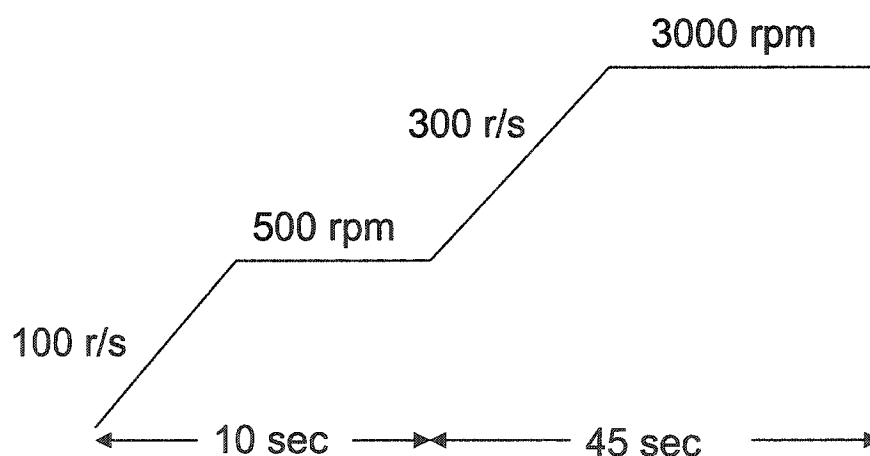


Figure 5. 2 Parameter of photoresist coating

Positive and Negative Photoresist: There are two types of photoresist: positive and negative. For positive resists, the resist is exposed with UV light wherever the underlying material is to be removed. In these resists, exposure to the UV light changes the chemical structure of the resist so that it becomes more soluble in the developer. The exposed resist is then washed away by the developer solution, leaving open regions

to the bare underlying material. The mask, therefore, contains an exact copy of the pattern which is to remain on the wafer [48].

Negative resists behave in just the opposite manner. Exposure to the UV light causes the negative resist to become cross-linked, and more difficult to dissolve. Therefore, the negative resist remains on the surface wherever it is exposed, and the developer solution removes only the unexposed portions. Masks used for negative photoresists, therefore, contain the inverse (or photographic "negative") of the pattern to be transferred.

Negative resists were popular in the early history of integrated circuit processing, but positive resists gradually became more widely used since they offer better process controllability for small geometry features. Positive resists are now the dominant type of resist used in VLSI fabrication processes.

Soft-Baking: Soft-baking is the step during which almost all of the solvents are removed from the photoresist coating. Soft-baking plays a very critical role in photo-imaging. The photoresist coatings become photosensitive, or imageable, only after softbaking. Over-softbaking will degrade the photosensitivity of the resists by either reducing the developer solubility or actually destroying a portion of the sensitizer. Under-softbaking will prevent light from reaching the sensitizer. Positive resists are incompletely exposed if considerable solvent remains in the coating. This under-softbaked positive resists is then readily attacked by the developer in both exposed and unexposed areas, causing less etching resistance.

Mask Alignment and Exposure: One of the most important steps in the photolithography process is mask alignment. A mask or "photomask" is a square glass

plate with a patterned emulsion of metal film on one side. The mask is aligned with the wafer, so that the pattern can be transferred onto the wafer surface. Each mask following the first one must be aligned to the previous pattern. The pattern will be transferred from the photoresist to the oxide layer and the resist will act as an etch masking layer. There are different methods available for back to front alignment of patterns on silicon wafers. The method used here will take advantage of the infrared transmission properties of the crystalline properties of silicon. A laminated wafer chuck will allow us to see through the wafer to the patterned metal with an unfiltered CCD camera. Figure 5. 3 shows the aligner used for fabrication.



Figure 5. 3 Aligners used in photolithography process

A design file for alignment marks designed in Tanner L-Edit format is drawn first. Three exposure modes, vacuum contact, projection, and proximity, can be selected. The lamp is calibrated at 15 mW/cm^2 at 365 nm. The basic procedures include:

1. Startup and loading of the mask, after the program has been selected load the mask.

The first mask is loaded, and no alignment is necessary. Place the mask with pattern

- side down, against the positioning pins. Cycle the mask into place, then the mask will be hold in position by vacuumed on the system.
2. Load wafer: Place the unexposed wafer on the wafer chuck. Two of the alignment pins are at the near edge and the third pin is at the left side. Press wafer vacuum on the touch-screen. Slide the mask holder all the way over the wafer chuck and press the start/stop button, align wafer with the alignment marks, set up proper focus, and exposure value.
 3. Alignment: Align the wafer to the mask by adjusting the X, Y, and theta manipulators.

Once the mask has been accurately aligned with the pattern on the wafer's surface, the photoresist is exposed through the pattern on the mask with a high intensity ultraviolet light. There are three primary exposure methods: contact, proximity, and projection.

Contact Printing: In contact printing, the resist-coated silicon wafer is brought into physical contact with the glass photomask. The wafer is held on a vacuum chuck, and the whole chuck assembly rises until the wafer and mask contact each other. The photoresist is exposed with UV light while the wafer is in contact position with the mask. Because of the contact between the resist and mask, very high resolution is possible in contact printing (e.g. 1-micron features in 0.5 microns of positive resist). The problem with contact printing is that debris, trapped between the resist and the mask, can damage the mask and cause defects in the pattern [48].

Proximity Printing: The proximity exposure method is similar to contact printing except that a small gap, 10 to 25 microns wide, is maintained between the wafer and the

mask during exposure. This gap minimizes (but may not eliminate) mask damage. Approximately 2- to 4-micron resolution is possible with proximity printing.

Projection Printing: Projection printing, avoids mask damage entirely. An image of the patterns on the mask is projected onto the resist-coated wafer, which is many centimeters away. In order to achieve high resolution, only a small portion of the mask is imaged. This small image field is scanned or stepped over the surface of the wafer. Projection printers that step the mask image over the wafer surface are called step-and-repeat systems. Step-and-repeat projection printers are capable of approximately 1-micron resolution, which depends on the wavelength a UV light used, the mask type and the thickness of the photoresist.

Development: One of the last steps in the photolithographic process is development. At low-exposure levels, the negative resist remains completely soluble in the developer solution. As the exposure is increased above a threshold energy (E_t), more of the resist film remains after development. At exposures two or three times the threshold energy, very little of the resist film is dissolved. For positive resists, the resist solubility in its developer is finite even at zero-exposure energy. The solubility gradually increases until, at some threshold, it becomes completely soluble. These curves are affected by all the resist processing variables: initial resist thickness, prebake conditions, developer chemistry, developing time, and others.

Hard-Baking: Hard-baking is the final step in the photolithographic process. This step is necessary in order to harden the photoresist to improve the adhesion of the photoresist to the wafer surface, and increase the etch resistance of the resist.

The lithography process carried out before deep dry etching is critical, since it directly affects the quality of etching.

All resist processing is done on a spinner, hotplate, at 40% relative humidity and 70 °F:

The following steps are lithography processes before dry etching:

- 1) Spin cosat AZ9260: 500rpm for 10 seconds 900rpm for 20 seconds Let the wafer sit for 5 minutes
- 2) Softbake at 110 °C, and and dry in vacuum oven for 4 min 10 sec.
Spin wafer for 60 second at 1000rpm, remove the edge bead using acetone soaked swab.
- 3) Spin AZ9260: 500rpm for 10 seconds at 900rpm for 20 seconds, let the wafer sit for 5 minutes.
- 4) Softbake at 110 °C for 5 minute, and dry in vacuum oven for 10 seconds, and xpose for 175 seconds.
- 5) Develop in AZ400K (1:4 ratio with water) for 1-4 minutes with proper agitation.
Developing time control is especially important for small feature size device. The developing time depends on both feature size and open area.
- 6) Hard-bake the wafer for 30-60 minutes at 160 °C, this step guarantees that the photoresist will be free of bubbles during the dry etching process.

5.1.2 Etching Processes

The Inductively Coupled Inductive Plasma Etching (ICP) reactors are widely used now for etching and polymer deposition applications due to their simpler design compared to other high density sources. The ICP is a reactor that couples plasma generation and transport phenomona with neutral species performing under particular

dynamics, and with the gas flow dynamics following certain principles. Current ongoing research has provided a valuable understanding of the physical etching mechanisms, and improvements to the physical etching processes [49][50]. In ICP, there are several inductor coils around the top of the chamber, which are driven by radiofrequency (RF) power. The inductor produces an alternating magnetic field in vertical direction. This alternating magnetic field produces a circular alternating electric field in the horizontal direction; The substrate to be etched is biased by RF power; the ion energy is controlled by the RF power at the plasma electrode.

The primary technology is based on the so-called "Bosch process", named after the German company, Robert Bosch, which filed the original patent, where two different gas compositions are alternated in the reactor. The first gas (C_4F_8) composition creates a polymer on the surface of the substrate, and the second gas (SF_6) composition etches the substrate. The polymer is immediately sputtered away by the physical part of the etching process, but only on the horizontal surfaces and not the sidewalls. Since the polymer only dissolves very slowly in the chemical part of the etching process, and builds up on the sidewalls protecting them from etching.

The Inductively Coupled Plasma Source using a room temperature process with He gas as the backside cooling medium, can perform isotropic etch and polymer formation in a controllable time sequence.

Deep etching of Si is achieved by inductive coupling of radiofrequency electrical energy to a sulfur hexafluoride (SF_6) plasma to direct a high flux of energetic ions and reactive fluorine atoms to the Si surface. The plasma etch is performed at a pressure, 3.2 Pa, which together with a high gas throughput, provides for rapid removal of the gaseous

etch products. The lateral topology of the Si microstructure is defined by a thin film of etch-resistant material, such as PR1813, and AZ9260 (thick photo-resist), which is patterned using conventional photolithographic processes. Ions from the plasma bombard the exposed Si surfaces and supply the energy needed to initiate a reaction between Si and atomic fluorine. In the absence of ion bombardment, no reaction occurs, so surfaces perpendicular to the wafer surface (the etch sidewalls) are etched slowly, yielding the desired vertical sidewalls.

The etch rate is dependant on the open area of silicon (macro-loading effect) with large open area samples etching slower than small open area samples. Features with a high aspect ratio will also etch slower than more open areas. This is known as the micro-loading effect (a phenomenon by which isolated trenches etch faster than those located in a dense array, or the variation in trench depth with mask window size). The basic assumption is that the microloading effect is due to diffusion limitations in the dark space region between the glow region and the wafer to be etched. [54] The channel shapes varied from straight, zigzag, and omega. Figure 5. 4 shows the SEM pictures of the channels. Figure 5. 5 shows the wafer of microreactors before and after dicing.

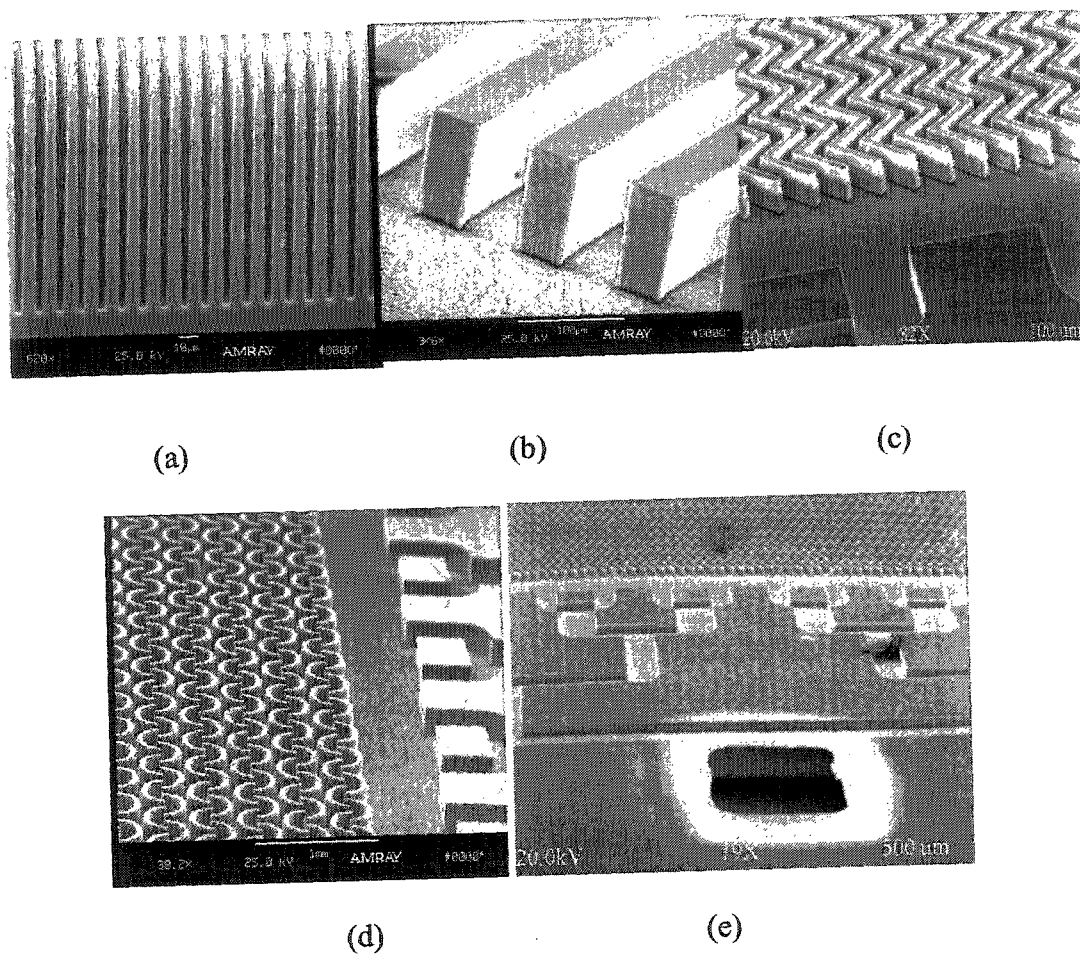


Figure 5. 4 SEM photos (a) cross-section of zigzag channels (b) straight channels (c) zigzag channels side view (d) omega channels (e) microreactor inlet via

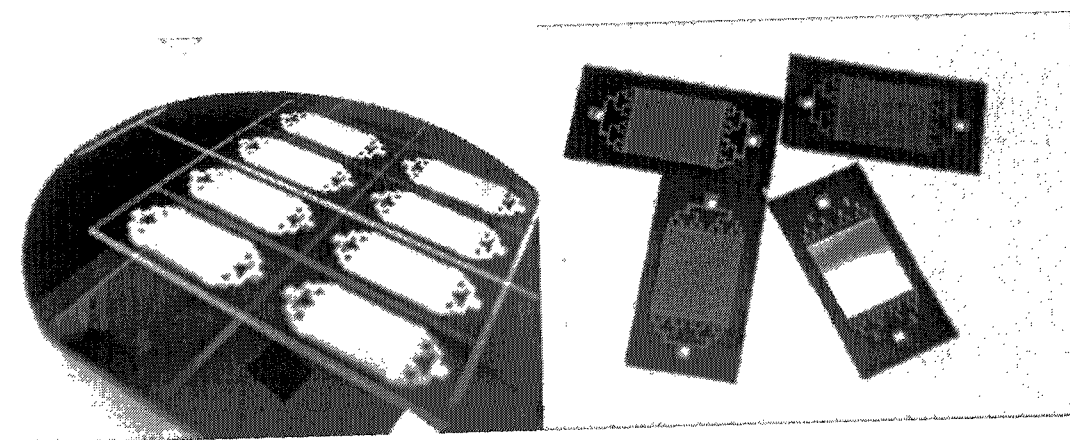


Figure 5. 5 Microreactor before and after dicing

After microfabrication, the Si wafer was diced into microreactors components according to the dimensional requirements. Apply the catalyst according to the desired reaction. The sol-gel catalyst preparation for reactions will be addressed in next section. After dipping in the sol-gel catalyst support, the reactor was anodically bonded to a 450 μ m thick Pyrex glass, which has the same dimension with the reactor, and the same thermal expansion coefficients as silicon.

5.2 Catalyst Preparation

The higher the active surface area of the catalyst, the greater the number of product molecules produced per unit time. There are two kinds of catalyst preparation methods-physical and chemical methods. The physical method refers to sputtering metal onto the reactor channel surface, while the chemical method refers to the sol-gel method, ion impregnation method, or a combination of both has been used [15]. The sol-gel process is the name given to any process involving a solution or sol that undergoes a sol-gel transition, which is a transition of a suspension of solid particles in a liquid (sol) to an apparent solid, jelly-like material (gel).

The solution is a truly single-phase liquid, while a sol is a stable suspension of colloidal particles. At the transition, the solution or sol becomes a rigid, porous mass by destabilization, precipitation, or super-saturation. Most of the coatings (spinning, dip, or drop) present the sol-gel transitions from true one-phase solutions to a rigid two-phase system of solid and solvent-filled pores. The sol-gel transition in this case is not reversible.

Iron and cobalt are the catalysts for the syn-gas conversion. Iron has high activity and the cobalt based catalyst shows lower water-gas shift activity [15]. Silica sol-gel was the support for Fe and Co.

Preparation of the Sol-gel Solution: We make the solution according to a fixed ratio; each ratio amount is listed in the following table. The processes of preparing silica sol-gel solution are listed in Table 5.1:

Take 108.5 g water in a beaker and heat to about 80 °C. Slowly add 10.4 g tetraethyl orthosilane (which is $\text{Si}(\text{OC}_2\text{H}_5)_4$, also called TEOS) into the beaker, while continuously stirring the solution. Add 103.5 g $\text{C}_2\text{H}_5\text{OH}$ and 1.17g 70% HNO_3 , then heat the solution until the temperature reaches to 90 °C. Reflux the content of the beaker for 12-16 hours, and then decrease to room temperature. This sol-gel solution can be stored for 2 to 3 weeks. It is ready for adding catalyst to form the catalyst solution.

Table 5.1 Sol-gel solution ratio

Partial	TEOS	DI water	$\text{C}_2\text{H}_5\text{OH}$	HNO_3
Mole	1	12	45	0.26
Net weight	208	18	46	63
eight ratio	208	216	2070	23.4
Density	0.934	1	0.79	1.41
Volume (ml)	2.23	216	2620	16.6
Real volume	2.22	2.16	26.2	0.16

Catalyst Preparation: The catalyst application method varies with different research approaches. In this research, we use ferric/cobalt nitrate as the catalyst precursor.

Table 5. 2 shows the chemicals used for sol-gel precursors and ion impregnation.

Table 5. 2 Sol-gel precursors and ion impregnation

		Precursors	Loading	
Catalyst	Iron	Ferric nitrate	0.77g	12%
	Cobalt	Cobalt nitrate	0.52 g	12%
Catalyst Promoter	Ru	RuCl ₃	9mg	
Catalyst Support	Silica	TEOS	10g	

They first undergo ammonia treatment to form ferric/cobalt hydroxides, then are calcinated to form ferric oxide, followed by hydrogenation to form pure metals of Fe/Co.

The procedure is given below:

- 1) Take 10 g sol-gel solution into a beaker and heat the solution to 70 °C, add 0.77 g of ferric nitrate-Fe(NO₃)₃·9H₂O, 0.52 g cobalt nitrate- Co(NO₃)₂·6H₂O and 9mg RuCl₃.
- 2) Stir the mixture continuously for 15 minutes. Dip the reactor into the solution, take it out and set on a 30 °C hot plate for 20 minutes until it is dry.
- 3) Wash the reactor with 10% NH₄OH for 25-30 minutes, followed by washing in hot water.
- 4) Dry the reactor in a vacuum oven at 60 °C for 30 minutes.
- 5) The catalyst then is treated with 10 sccm of H₂ in a wafer process oven at 600 °C to change the chemical state of the catalyst from Fe⁺ and Co⁺ to Fe⁰ and Co⁰, since the reduced metal is the final catalyst.

After the catalyst is applied into the channels, the catalyst coating on the channel walls should undergo an important step called ammonia wash to produce hydronitride followed by reduction with H_2 .

One important issue is that, before the 40% H_2 could be fed into the oven, argon gas is needed to purge the air out of the furnace and tubes to keep residual oxygen from mixing with hydrogen because of the high temperature of operation. The process for the reduction of Fe/Co is listed below.

- 1) Calculate the volume of the furnace (15.67 L) and the volume of all tubes (2.695 L). The total volume is 55 L.
- 2) Close V1, V2, and V6, open V3, V4, V5, and V8.
- 3) Flow argon at 100 sccm ($cm^3/minute$) for 30 min to remove air from the furnace and tubes.
- 4) 2. Close V7, open V6, and flow H_2 into the furnace at 10 sccm for 14 min.
- 5) Heat the furnace to 450-600 °C at the same time. Then, change the flow rate to 15 sccm. Keep this flow rate and temperature for approximately 7 hours for Fe/CO reduction.
- 6) Stop heating after 7 hours and allow the system to cool down.
- 7) Close V6, open V7, and flow argon into the furnace at 10 sccm for 14 min when the temperature reaches 100 °C.
- 8) Close V7, unload the samples.

The schematic drawing of the metal reduction apparatus is shown in Figure 5. 6.

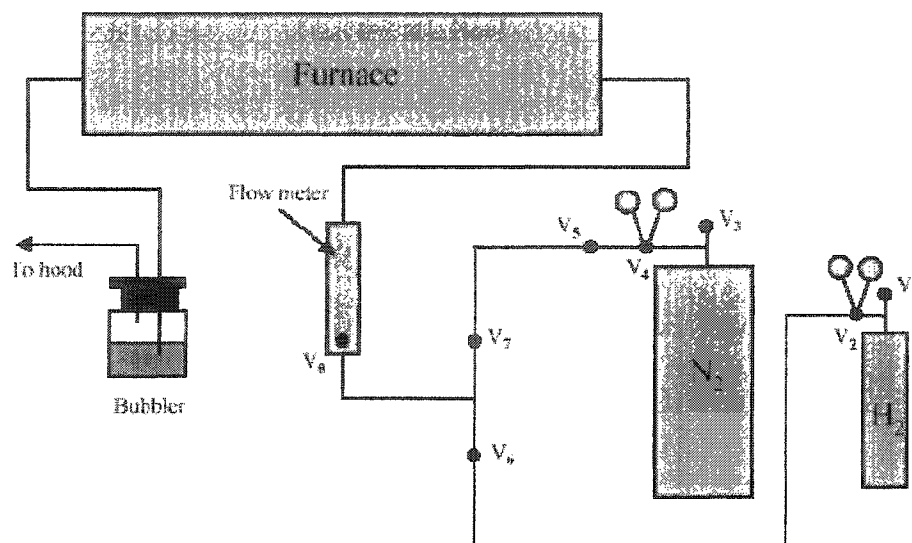


Figure 5. 6 Schematic drawing of metal reduction apparatus

It has been reported by other researchers that the loading of 6% ferric nitrate and 6% cobalt nitrate does produce good results. We use 12% ferric nitrate and 12% cobalt nitrate for catalyst loading as our basic reaction comparisons. However, this is the intended loading. The real loading is much lower than intended (around 3% loading of each metal).

5.3 Bonding

When the fabrication process and catalyst coating process are completed, the reactor is encapsulated for reaction. The reactor is sealed with pyrex glass 7740, which has the same dimension as the microreactor, and 500 μm in thickness, for testing catalyst activity and efficiency. The microreactor and the pyrex were assembled together by anodic bonding. The schematic drawing of Anodic bonding is shown in Figure 5. 7.

- 1) Clean the microreactor and the pyrex glass with acetone, distilled water, and isopropyl alcohol.

- 2) Place the microreactor into the bed of a stainless plate, cove the microreactor with the glass, and put the top stainless plate on the glass.
- 3) Hold them together and put into the furnace. Connect to the high voltage power supply, the power range is between 500- 1000 w.
- 4) Heat the furnace to 450 °C and allow to set for 45 minutes
- 5) Apply the voltage to 750 volts and keep the current close to 0.1 amp for 45 minutes.
- 6) Turn off the power to the furnace and power supply. Cool down the furnace to room temperature. Then take out the microreactor for pressure testing.

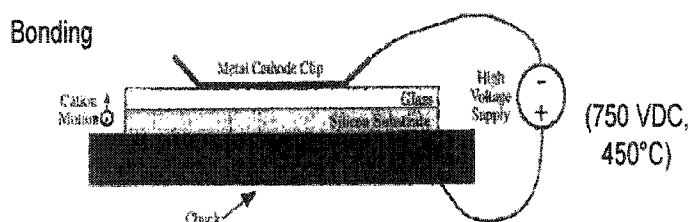


Figure 5. 7 Anode bonding

Currently, sealing techniques such as wafer bonding and soft elastomer sealing are being used for sealing the micrometer-scale exposed channels and structures. In our new setup system rather than the pyrex cover bonding with the reactor, a fluoroelastomer (a sample from Mosites rubber company Inc) is plated between the inlet/out vias and the apparatus. This elastomer, which has high strength, high elongation, and good heat resistance, serves both as the spacer and the sealing method. Its mechanical properties are listed in Table 5.3. By comparing the above methods in the experimental setup, the one with temperature resistance elastomer turned out to be more efficient and effort saving.

Table 5.3 Mechanical Properties of Fluoroelastomer

Temp Range	Tensile Strength	Elongation at Break	Modulus at 100% Elongation	Tear Strength
-23 °C-357°C	2600 psi	210%	1150 psi	128 psi

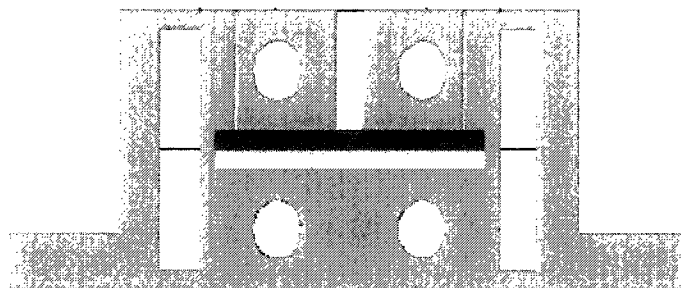


Figure 5.8 Heating Block for System Setup

5.4 Testing System

Testing of the reactors' performance is as important as that of design and fabrication. The testing apparatus includes controlling of flow, temperature, and pressure, and the acquisition of the product distribution of the effluent stream. The reactor chip interfaces to a steel holding block (Figure 5.8) fitted with gas connections to the inlet and outlet openings on the bottom side of the chip. Gases are fed to the block by mass flow controllers, and digital pressure sensors are located in the inlet and outlet streams to monitor pressure drops [15]. Figure 5.9 shows the microreaction system setup. The flow and reactor temperature settings were monitored and controlled by a LabView (National Instrument) software. The testing apparatus is shown in Figure 5.9.

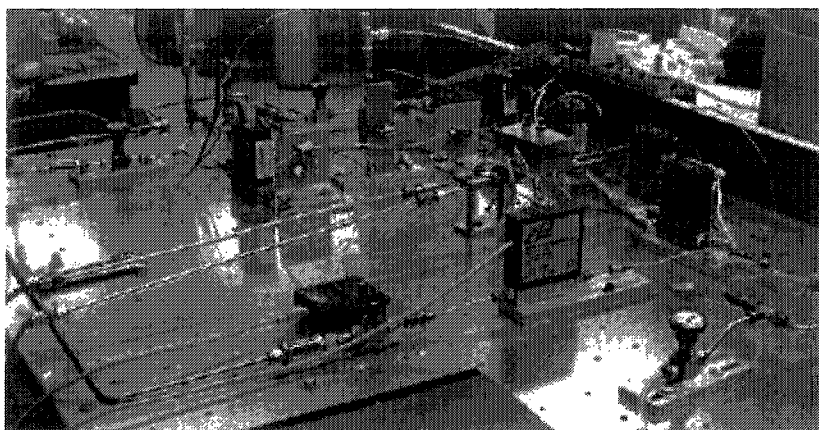


Figure 5.9 Microreaction setup system

The outlet stream for the experiments was exhausted at atmospheric pressure. Reactor effluent was monitored for composition detection using a Stanford Research System mass spectrometer with data acquisition and control programs. The effluent stream, which in these experiments varied between approximately 0.2 sccm and 2 sccm, was diluted with helium prior to the mass spectrometer sampling point to protect the mass spectrometer, and also to supply an adequate sampling flow.

The procedure for quantitative analysis of the effluent began by calibrating the mass spectrometer with ambient air as a standard for establishing the sensitivity to nitrogen. Pure reactants were fed into the reactor in combination with nitrogen in order to determine their respective sensitivity factors. The calibrated mass spectrometer was then used to record continuous partial pressure data during the course of the experiments where conditions of temperature and reaction flow rates were varied [15]. For syn-gas reactions, pure hydrogen and carbon monoxide were the reactants mixed together before being fed into the microreactor. The reaction of syn-gas to higher alkanes with the newly designed reactor with omega channels is accomplished in this system.

CHAPTER 6

RESULTS AND DISCUSSION

6.1 Catalyst in Syn-Gas Reaction

A wide range of syn-gas conversions have been obtained by varying space velocities over catalysts with various Fe loadings. Different trends in catalyst activity with Fe loading were observed depending on the space velocity or synthesis gas conversion. As Fe loading increased, the catalyst activity either decreased (low conversions), passed through a maximum (intermediate conversions) or increased (high conversions). This is shown to be a result of the increasing dependency of the Syn-Gas synthesis on the hydrogen formed by the water-gas shift reaction with increasing synthesis gas conversions [67][68][69].

Characterization of the catalyst: surface area measurement is important to determine the best support material for the catalyst. The sol-gel method improves the surface area of the catalyst encapsulated in it and also increases its reactivity. Surface area measurements of the substrates coated with Silica were performed in a Quantachrome NOVA 2000 series instrument. Nitrogen was used as adsorbate in these measurements. Brunauer-Emmett-Teller (BET) method is the widely used method for the determination of surface area of solid materials [70][71][72].

Scanning Electron Microscopy (SEM): SEM is a very widely used technique to

study surface topography. A high energy (typically 10-30 keV) focused electron beam is scanned across the surface. The incident electrons cause low energy secondary electrons to be generated, and some escape from the surface. The secondary electrons emitted from the sample are detected by attracting them to a scintillator. The scintillator converts electron energy to photons and the intensity of the light produced is measured with a photomultiplier. The resulting information appears as a scanned topographical image on a CRT. The incident electrons will also cause X-rays to be generated. Some of the incident electrons interact with the atomic structure of the sample and are deflected back into the vacuum chamber. These electrons are known as backscattered primaries and can be detected with a backscattered electron detector. Backscattered electrons can also give information on the surface topography and on the average atomic number of the area scanned by the electron beam. Figure 6.1 shows the SEM pictures of sol-gel coating omega channel.

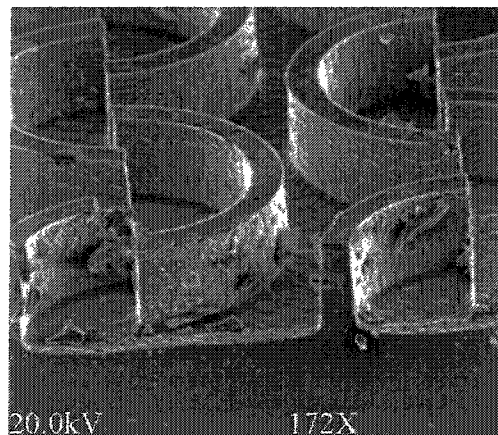


Figure 6. 1 SEM picture of sol-gel coated omega channel

Energy Dispersive X-ray Analysis (EDX) Analysis: The EDX system is used in conjunction with the SEM, and is capable of detecting all elements from carbon to uranium, with a detection limit of ~ 0.5 wt% for most elements. Backscattered electron imaging and elemental X-ray mapping provide graphic presentation of elemental distributions.

The Quartz Xone system uses full spectral imaging. This means that all of the X-ray events that occur at each pixel are recorded. This allows for live and post collection data analysis.

EDX analysis examines the elemental composition of Co and Fe encapsulated in the silica sol-gel deposited in the microreactors. EDX spectroscopy is used in order to optimize the catalyst preparation and deposition processes. The EDX spectrometer is equipped with a super quantum lithium drifted silicon detector detector that has elemental analysis capability in the wide range from boron through uranium with better than 145 eV resolution. Figure 6. 2 shows the X-ray spectrum of the sol-gel deposited reactor channel surface.

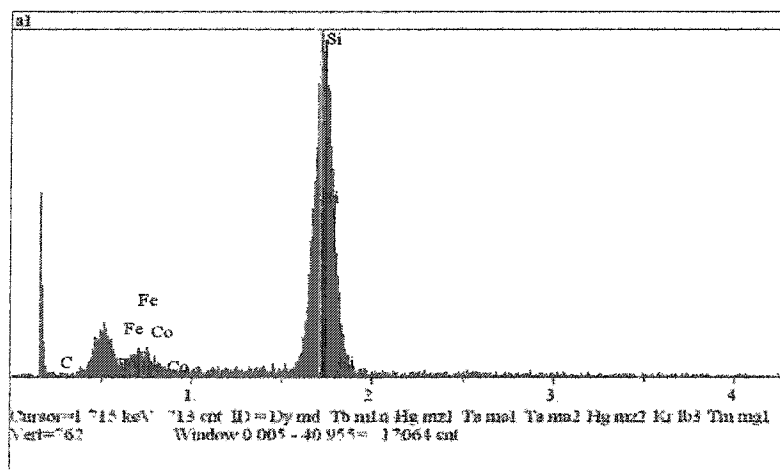


Figure 6. 2 Energy dispersive X-ray analysis of an intended composition of 12% Fe+12% Co catalyst

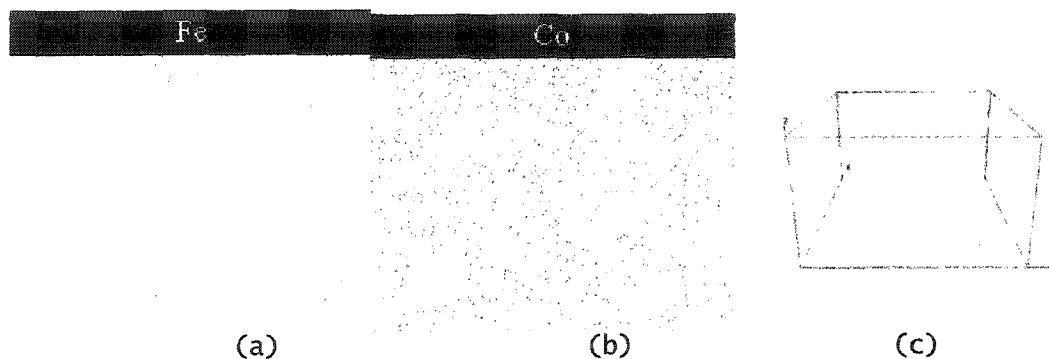


Figure 6. 3 EDX fast map on density of catalyst (a) Fe density from EDX fast map (b) Co density from EDX fast map (c) 3D views of metal density

The percentage of intended 12% loading with iron and cobalt catalysts are extracted by the EDX's fastmap function. 1.54 g of iron, and 1.04 g of cobalt was loaded. It is shown that only 6.7% of Fe and 5.8 % of Co were loaded in the solgel instead of 12 % each; and only 15.4% of Fe and 12.3 % of Co were loaded in the solgel instead of 18 % each. This may be due to incomplete reduction process and due to seeping that may occur during the activation of the catalyst to pure metal. The EDX fast maps for samples with 12% Fe+12% Co catalyst are shown in Figure 6.3. The comparison of the density of the two catalysts is presented in Figure 6. 3.

This also signifies that only small amount of the catalyst is really responsible for the reaction. The activation process of the catalysts from their nitrate salts to pure metal form has to be improved for increasing the % loading of Fe and Co in the sol-gel.

6.2 Catalyst and Conversion Study in Syn-Gas Conversion

The conversion of the reaction is expressed as:

$$\frac{\text{Baseline CO Partial Pressure} - \text{Real Reaction CO Partial Pressure}}{\text{Baseline CO Partial Pressure}}$$

Therefore, we need to know the partial pressure of CO in both the real reaction and the baseline reaction. Base line reaction is the reaction that takes place at room temperature without a catalyst.

QMS 100 Series Gas Analyzer: For quantitative analysis of the effluent of reactants and products at the outlet of the reaction system, a QMS 100 Series Gas Analyzer from Stanford Research Systems was employed to record continuous partial pressure data of CO during the course of the experiments while temperature and reactant flow rates were varied.

The QMS 100 series instruments are modern mass spectrometers designed for the analysis of light gases. The spectrometer operates at high vacuum (10mbar). Not only are the data acquired continuously, but the response is also fast. A change in composition at the inlet can be detected in less than 0.5 second. The system allows data to be collected quickly; a complete spectrum can be acquired in less than one minute and individual masses can be measured at rates up to 25 ms per point. The QMS consists of two subsystems: gas handling and the analyzer. The analyzer specializes in large dynamic range measurements of light gases. For users with specialized needs, the QMS can be controlled from user programs. This modern system allows many new applications in contrast to the traditional mass spectrometer that is large and heavy . The analyzer is a quadrupole mass spectrometer, and it can only operate in high vacuum. The class of quadrupole mass spectrometer employed belongs to a class which is referred to as a residual gas analyzer (RGA). A residual gas analyzer is a mass spectrometer of small physical dimensions whose function is to analyze the gases inside the vacuum chamber. The principle is that a small fraction of the gas molecules are ionized to create positive

ions, and the resulting ions are separated, detected and measured according to their molecular masses. It can quickly identify the molecules present in a gas, and when properly calibrated, it can be used to determine the concentrations and partial pressures of the components of a gas mixture. Once the different components of a mixture have been identified, RGA is also used to obtain quantitative values for the various partial pressures. In this research, what we require is to extract the partial pressures of CO both for the baseline and the real reactions.

The baseline reactions have been performed with three different target microreactors (straight, zigzag, and omega channels respectively) with the same input flow rates and three different gas ratios. The six different feed-in flow rates of the reactant gas (H_2/CO) are: 0.6 sccm of H_2 to 0.4 sccm of CO; 0.6 sccm of H_2 to 0.3 sccm of CO; 0.6 sccm of H_2 to 0.2 sccm of CO; 0.3 sccm of H_2 to 0.2 sccm of CO; 0.2 sccm of H_2 to 0.1 sccm of CO; and 0.3 sccm of H_2 to 0.1 sccm of CO.

At constant temperature and volume, the total pressure of a gas sample is determined by the total number of moles of gas present, whether this represents a single substance, or a mixture. The ratio of the partial pressure to the total pressure is equal to the mole fraction of the component gas, which is given in Dalton's atomic theory.

The data of the baseline reactions for straight, zigzag and omega channels from the residual gas analyzer and data acquisition programs are listed in table 6.1. It can be observed from the table that the partial pressure of CO from straight, zigzag and omega channel reactors increase, which means that the omega reactor does consume more of CO than the zigzag and straight reactors, and the zigzag reactor consumes more CO than the straight reactor does. This can be explained in that longer residence time encourages

more collisions among the reactant species and the catalyst coated channel walls, hence higher conversion of CO to syn-gas.

Table 6. 1 Baseline reaction partial pressure of CO

H ₂ /CO feed-in flow rates	Straight Channel CO partial pressure	Zigzag Channel CO partial pressure	Omega Channel CO partial pressure
0.6/0.4	57 mTorr	60.7 mTorr	81 mTorr
0.6/0.3	48.9 mTorr	43.8 mTorr	67 mTorr
0.6/0.2	36.4 mTorr	37.7 mTorr	40.8 mTorr

Also, real time reactions with the same series of three different target reactors (with straight, zigzag, and omega channels respectively) have been performed with an intended composition, 12% Fe and 12% Co catalyst (with 1% Ru as the promoter). The data were extracted and processed from the RGA in the same way as that of the baseline reactions. The gas ratios are: 0.6 sccm of H₂ to 0.4 sccm of CO; 0.6 sccm of H₂ to 0.3 sccm of CO; 0.6 sccm of H₂ to 0.2 sccm of CO. Table 6.4 present the partial pressure of CO after the catalyst has promoted real reactions.

Table 6. 2 Real reaction partial pressure of CO with 12% Fe +12% Co catalyst

H ₂ /CO feed-in flow rates	Straight Channel CO partial pressure	Zigzag Channel CO partial pressure	Omega Channel CO partial pressure
0.6/0.4	34.8 mTorr	33.57 mTorr	45.9 mTorr
0.6/0.3	25.4 mTorr	21.93 mTorr	27.7 mTorr
0.6/0.2	17.6 mTorr	17.1 mTorr	17.9 mTorr

Table 6. 3 Conversion of syn-gas to higher alkanes with 12% Fe +12% Co catalyst

H ₂ /CO feed-in flow rates	Straight Channel CO Conversion	Zigzag Channel CO Conversion	Omega Channel CO Conversion
0.6/0.4	38.9 %	44.7%	43.3 %
0.6/0.3	48 %	50%	58.7 %
0.6/0.2	51.6 %	54.75%	56.2 %

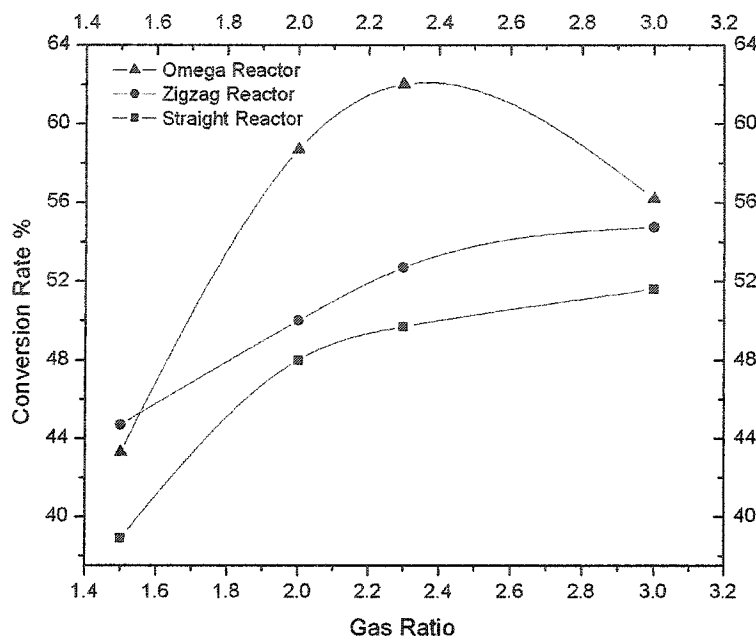


Figure 6. 4 Conversion of straight, zigzag and omega microreactors with different reactant gas ratios at H_2/CO flow rate of 0.6/0.4, 0.6/0.3 and 0.6/0.2 sccm

The conversions of each microreactor with different gas ratios are calculated according to equation 6.2. The different conversions at higher flow rates are shown in Figure 6.4. The conversions at lower flow rates are shown in Figure 6.5. It can be observed that the conversions in the omega channel microreactors are higher than that in the zigzag channel microreactors under the same conditions, and the conversion in the zigzag channel microreactor is higher than that of the straight channel microreactors under the same condition. This is coincident with the simulation prediction discussed in chapter three. The advantage of the omega reactor lies in the mixing performances. Consequently, this mixing advantage contributes to the higher conversion of the omega reactor over that of the other two types of reactors.

It can also be observed that the three reactors have the lowest conversion when gas ratio (H_2/CO) is 1.5. Omega reactors reach the maximum conversion when the gas

ratio reaches to 2, and begin to drop when the gas ratio increases. The conversions of both zigzag and straight microreactors increase as the ratio increases from 1.5 to 3. As a result, at H₂/CO gas ratio of 2, omega has the best performance compare to the other two microreactors. The highest flow rate is only 0.6 sccm of H₂ to 0.4 sccm of CO. This flow rate is still not high enough to generate asymmetry and recirculation of the flows in the omega channel (a phenomenon discussed in chapter three) of the current microreaction system. Therefore, long residence time is the primary reason for better conversion. Real reactions with three different target reactors (with straight, zigzag, and omega channels respectively) have also been performed for the lower flow rate conditions.

Table 6. 4 Baseline reaction partial pressure of CO

H ₂ /CO feed-in flow rates	Straight Channel CO partial pressure	Zigzag Channel CO partial pressure	Omega Channel CO partial pressure
0.3/0.2	30.5 mTorr	32.5 mTorr	39.5 mTorr
0.2/0.1	18.4 mTorr	22.3 mTorr	26.5 mTorr
0.3/0.1	19.3 mTorr	27.8 mTorr	32.25 mTorr

Table 6.4 shows the baseline reaction partial pressures of the three set of reactors at 0.3 sccm of H₂ to 0.2 sccm of CO; 0.2 sccm of H₂ to 0.1 sccm of CO; and 0.3 sccm of H₂ to 0.1 sccm of CO.

Table 6. 5 presents the partial pressure of CO following the catalyst promoted real reactions. The data were extracted and processed from the RGA in the same way as that of the baseline reactions.

Table 6. 5 Real reaction partial pressure of CO with an intended 12% Fe +12% Co catalyst loading

H ₂ /CO feed-in flow rates	Straight Channel CO partial pressure	Zigzag Channel CO partial pressure	Omega Channel CO partial pressure
0.3/0.2	15.5 mTorr	17.225 mTorr	17.4 mTorr
0.2/0.1	8.99 mTorr	10.258 mTorr	8.79 mTorr
0.3/0.1	6.49 mTorr	8.84 mTorr	6.87 mTorr

Table 6. 6 Conversion of syn-gas to higher alkanes with an intended 12% Fe +12% Co catalyst loading

H ₂ /CO feed-in flow rates	Straight Channel CO Conversion	Zigzag Channel CO Conversion	Omega Channel CO Conversion
0.3/0.2	49.2 %	47%	55.98 %
0.2/0.1	51.1 %	54%	67 %
0.3/0.1	67 %	68.2%	78.7 %

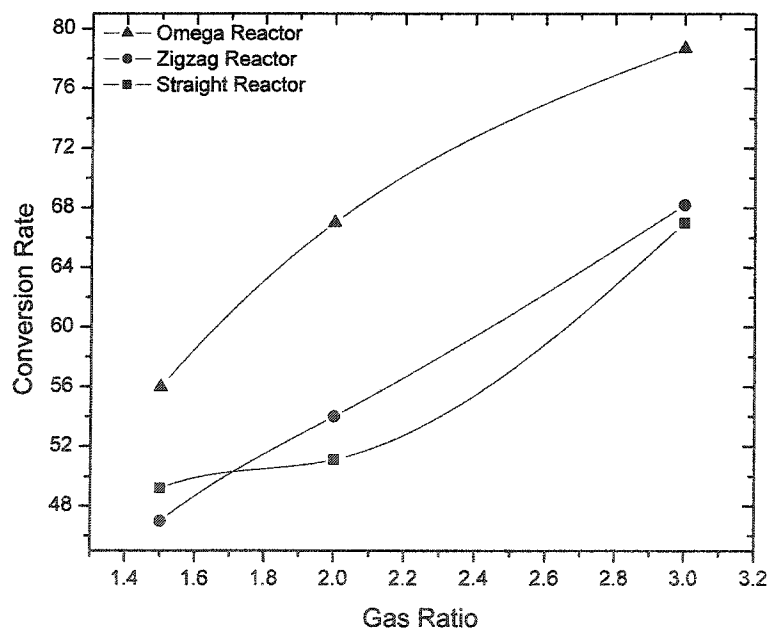


Figure 6. 5 Conversion of straight, zigzag and omega microreactors with different reactant gas ratios at H₂/CO flow rate of 0.3/0.2, 0.2/0.1 and 0.3/0.1 sccm

Table 6. 6 and Figure 6. 5 show the experimental results of conversions at lower flow rates of 0.3/0.2, 0.2/0.1 and 0.3/0.1. They are also in agreement with the simulation discussed in chapter three. At same gas ratios, lower flow rates generate higher conversion than that of higher flow rates (again, the residence time is the primary reason for better conversion under our system conditions). When the gas ratio is 3, at low flow rate the omega reactor has conversion of 78.7 %, but at high flow rate the omega reactor can only reach 56.2%. This can be explained by the fact that lower flow rates have longer residence time, which allows the molecules of different reaction species more time in the mixing and breaking of the C – O bond, therefore promoting hydrocarbon chain $(-CH_2-)_n$ growth. The experimental results show that the conversion efficiency for an omega-shaped reactor is 17 % greater than that for a conventional straight channel microreactor, and is 12 % greater than that for the zigzag-shaped channel microreactor.

It can also be concluded that among the different H_2/CO feed-in flow rates. An H_2/CO feed-in flow rate of 0.3sccm/0.1sccm gives the best performance. This can explain why the lower flow rate results in a lower velocity during the reaction, which then increases the residence time, and, therefore allows more collision chances between reactant molecules and catalyst, and encourages more CO molecules to be consumed in the reaction. The conversion improvement of omega channel microreactor than that of the zigzag channel microreactor is around 13% at the H_2/CO feed-in flow rate at 0.3sccm/0.1sccm. The conversion improvement of the omega channel microreactor over that of the straight channel microreactor is around 15% at the H_2/CO feed-in flow rate of 0.3sccm/0.1sccm.

6.3 Comparison with Modeling Results

There are four different compartments, one row by one column (1x1), one row by three columns (1x3), two rows by two columns (2x2), and two rows by three columns (2x3) of the omega channel reactor. The Figure 4.1 previously shown in Chapter Four, as well as Figure 6.6, Figure 6.7 and Figure 6.8 are corresponding to the velocity contours of omega channel compartments 1x1, 1x3, 2x2, and 2x3 respectively. There are four different counterparts of zigzag channel reactors and straight channel reactors. The three sets of microreactors with four different compartments were investigated by the Markov chain approach in terms of probability of molecules exiting the reactors studied, the mean and variance of residence time in the reactors studied, and residence time distributions.

From the Markov chain approach, a series of cumulative probabilities $P_{1D}(t)$ for the reactors were calculated with Matlab®, an integrated technical computing environment that combines numeric computation, advanced graphics and visualization, and a high-level programming developed by The Mathworks, Inc.

The graphs of $P_{1D}(t)$ vs t show in Figure 6.7, Figure 6.9 and Figure 6.11 present the simulation results for the 1x3, 2x2, and 2x3 compartments for different reactor types, omega channel (omega), zigzag channel, and straight channel reactor. It is obvious that $P_{1D}(t)_{straight} > P_{1D}(t)_{zigzag} > P_{1D}(t)_{Omega}$. This was shown previously in Figure 4.2. As expected, a molecule in the omega channel will take the longest time to exit the reactor among the three sets of reactors.

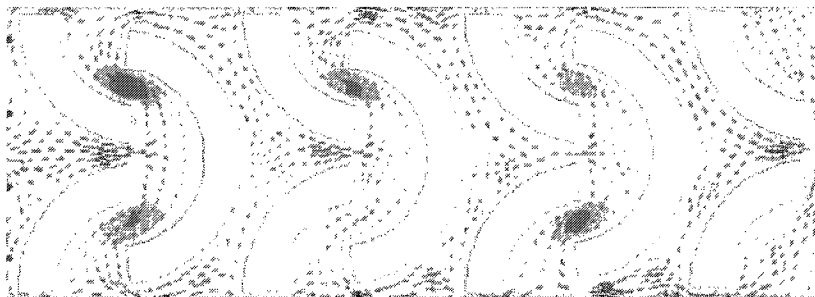


Figure 6. 6 Velocity contour for compartments 1x3

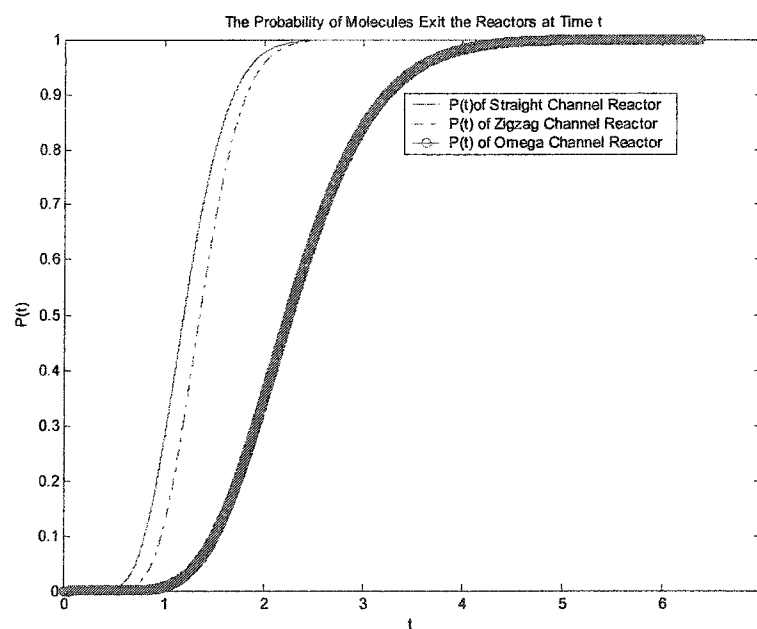


Figure 6. 7 Cumulative probability of a molecule exiting the three microreactors for compartments 1x3

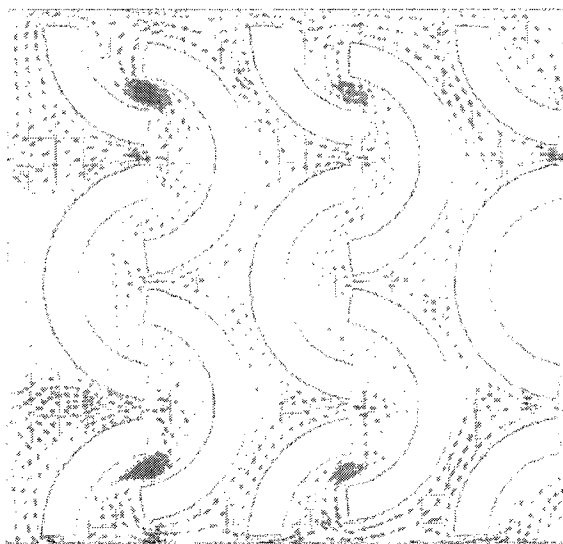


Figure 6. 8 Velocity contour for compartments 2x2

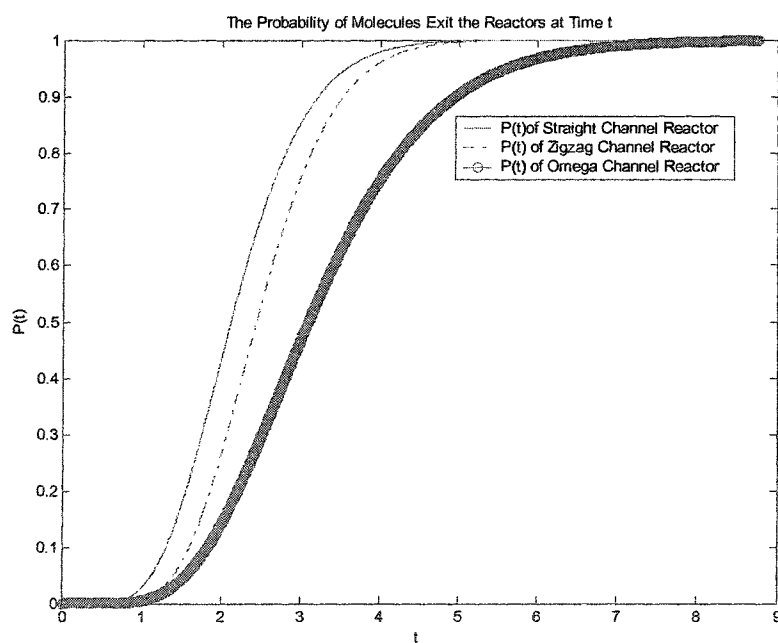


Figure 6. 9 Cumulative probability of a molecule exiting the three microreactors for compartments 2x2

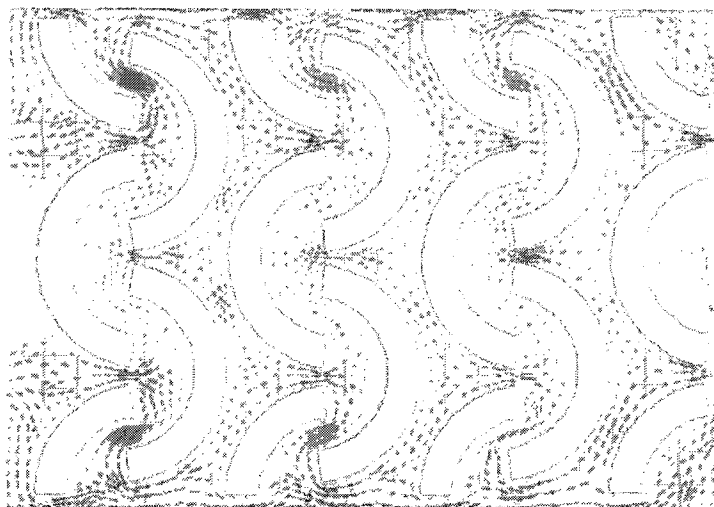


Figure 6. 10 Velocity contour for compartments 2x3

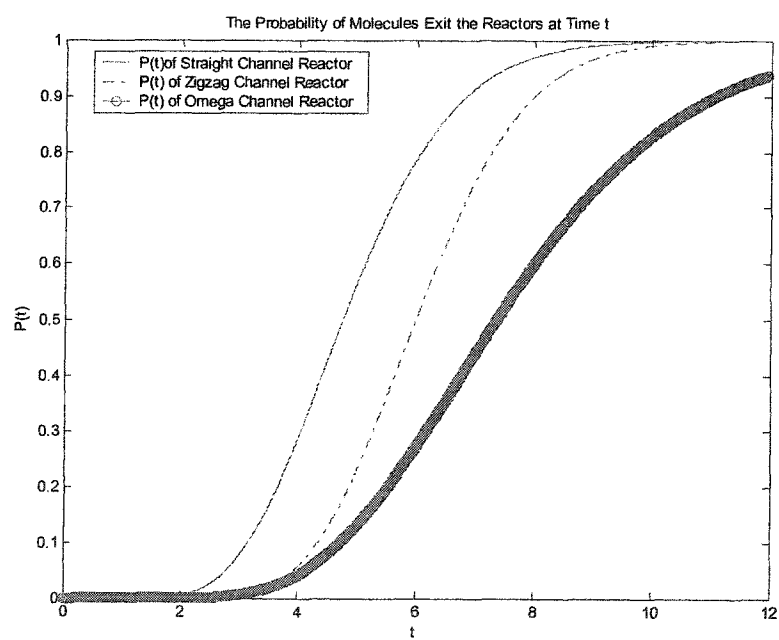


Figure 6. 11 Cumulative probability of a molecule exiting the three microreactors for compartments 2x3

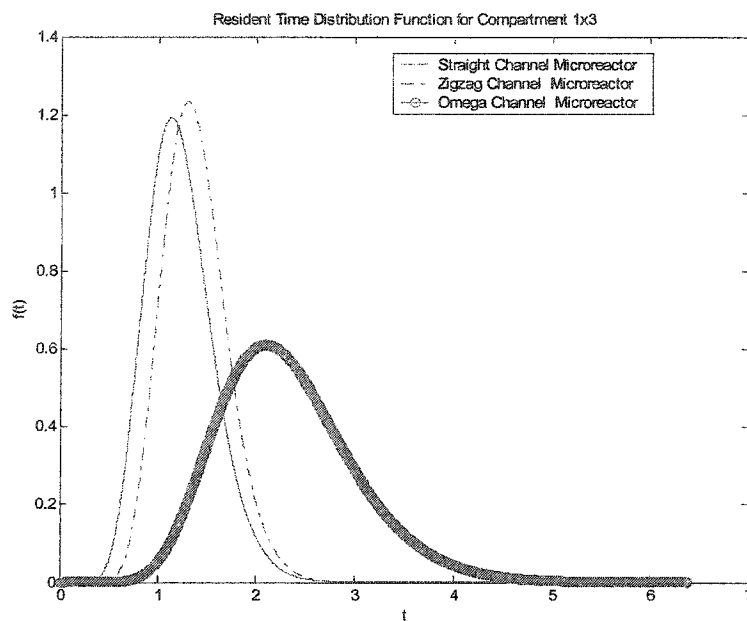


Figure 6.12 Residence time distributions of the three microreactors for compartments 1x3

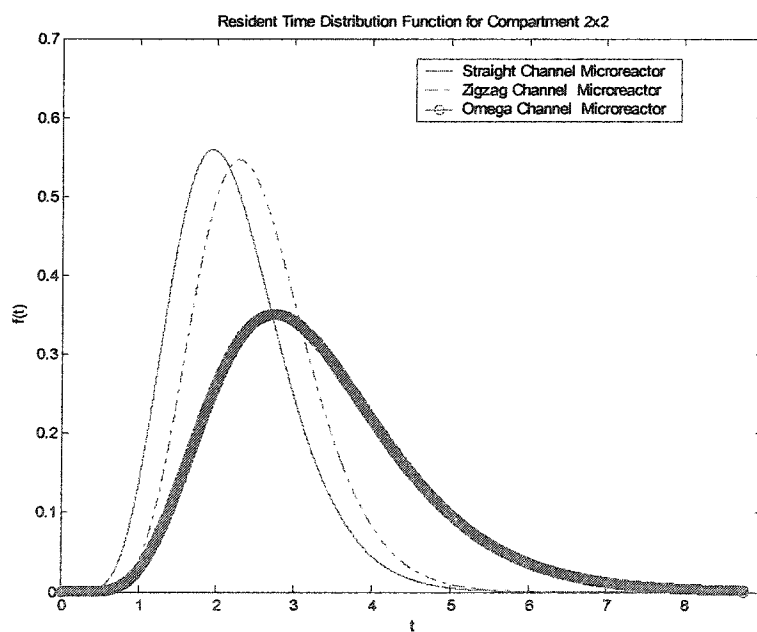


Figure 6.13 Residence time distributions of the three microreactors for compartments 2x2

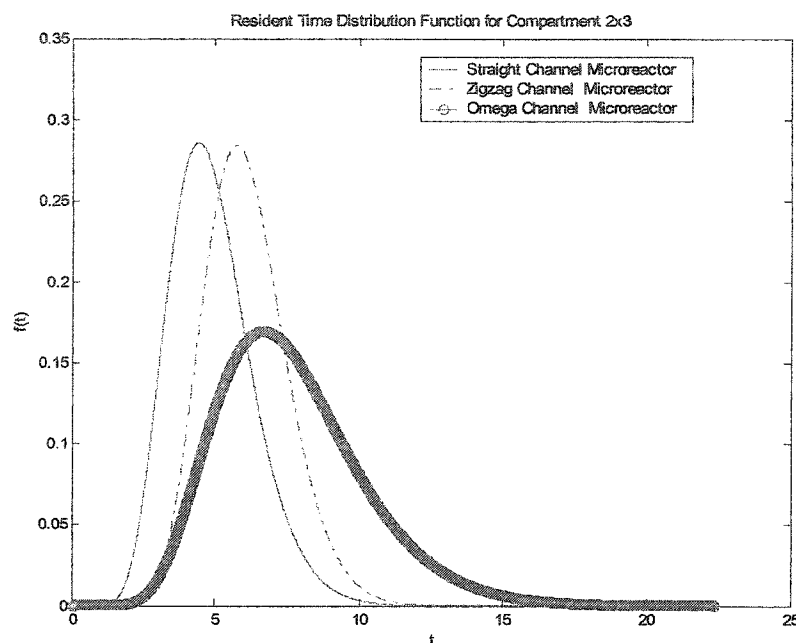


Figure 6.14 Residence time distribution of the three microreactors for compartments 2x3

Figure 6.12, 6.13 and 6.14 show the simulation results (for compartments 1x3, 2x2, and 2x3) of the probability density function for the residence time. From these Figures, it is easy to see that the omega channel microreactor has a higher mean residence time than the other two microreactors and the variance of the residence time is the largest due to the turbulence tendency (which has been discussed in chapter three). It also indicates that a molecule in the omega microreactor takes, on the average, a longer time to exit than for the case of the other two microreactors. Also, the variance in residence time in the omega microreactor is larger than that of the other two, which agrees with the observations with regard to the cumulative probabilities of a molecule exiting the reactor. The above results indicate that the omega channel microreactor has a longer residence time than the other reactors. This tends to agree with the earlier observation in chapter three that the omega channel type has a much greater mixing efficiency than that of the

other two types, and in agreement with the experimental run of the reaction conversion shown in Figure 6.4 and Figure 6.5.

CHAPTER 7

CONCLUSION AND FUTURE WORK

7.1 Conclusion

In this study, the flow properties in the straight, zigzag, and omega shaped microchannels were studied. Computational Fluid Dynamics simulations, which could produce large number of results under different design circumstances, were performed to further study the flow properties and mixing phenomena in the three sets of microreactors. The proposed omega-shaped channel microreactor design exhibits a more favorable velocity profile by guiding fluid streams over alternating, turbulence-generating obstacles.

Markov chain techniques were used to characterize the different structure of the microreactors in order to exhibit the molecular residence time distribution in the novel omega microreactor, and compared the results from the omega reactor with those of the straight and zigzag microreactors, and predict their reaction conversion efficiency.

The results of the Markov chain approaches and cumulative probability distribution and residence time distribution, validate the novelty of the omega channel microreactor. Micromaching technology and dry etching processes are used in the microreactor fabrication. Fischer-Tropsch reactions were carried out in straight, zigzag, and omega shaped micro-channel silicon microreactors at atmospheric pressure,

controlled temperature and controlled inlet, outlet flow rates. The catalytic reactions in the three sets of microreactors were studied. In the reaction part, we have tried to optimize the reaction conditions by studying the reactions at different flow rates within a microreactor. A high conversion of CO is achieved at H₂: CO ratio 2:1 and 3:1, as is evident from the fact that as the ratio of H₂: CO is increased, the conversion of CO gradually decreases. A temperature in range of 200- 260 °C was found to be good for the CO conversion with a maximum yield observed at temperatures around 230- 240 °C. The flow rate at which the feed gas is sent through the reactor also has a significant effect on the conversion of CO. The residence time is the primary reason for better conversion under our system conditions. The overall conversion of CO decreases with increasing flow rate. Finally, the conversions under the three different microreactors were compared with the theoretical predictions from the CFD and Markov chain models, and good agreement was obtained.

This work is expected to provide a precursory research and solid base for a Fischer-Tropsch reaction evaluation. The knowledge we obtained from these studies will set valuable guidelines for design and configuring different microfluidic devices to support the development of μ Total analysis system.

7.2 Future Work

To appropriately model the movement of an element a particle as a combination of diffusion and random displacements in a turbulent flow system for the omega-shaped channel microreactor is the next step of our research.

The design rules for a micro/nano reaction system can be summed up in three aspects: highly integrated, high precision control, and faster analysis for these micro

devices that have been built by research facilities. However few have been integrated into a complete system as yet. Therefore, reducing the need for external components, which includes integrated heaters, temperature sensors, flow sensors, pressure sensors, etc, is the basic goal of chemical processing system on a chip- which is next step of our research.

APPENDIX A

SOURCE CODES

Cumulative Probability of a Molecule Exiting the Three Microreactors

&

Residence Time Density Function.

Compartment 1x1

```

AS=[
0.9721540.0278460      0      0      0;
0      0.9710620.0289380      0      0;
0      0      0.9710620.0289380      0;
0      0      0      0.9710620.0289380;
0      0      0      0      0.9181  0.0819;
0      0      0      0      0      1
];

n=999;
BS= zeros(1,n);
CS =AS* AS;
for i=1:n

    CS =CS*AS;
    BS(i) = CS(1, 6) ;
end;
%% calculate mean and variance
Q=AS;
Q(:,6)=[];
Q(6,:)=[];
I=eye(5);

N=inv(I-Q);
E=[1; 1; 1; 1; 1];
MeanTimeS=N*E;
SQ=MeanTimeS.^2;
VarianceS =(2*N-I)*MeanTimeS-SQ;
MeanTimeS= MeanTimeS*0.0031941;
VarianceS= VarianceS*0.0031941^2;
FS= zeros(1,n);
%% calculate mean and get F- the density function

```

```

for i=2:n
    FS (i-1) = ( BS(i)-BS(i-1) )/ (0.0031941);

    end;
%% test that sum of f(t)* 0.0031941=1
sum=zeros(1,1);
for i=1:n
    sum = FS(i)* 0.0031941+sum;
end;
sum
%% sum=1
meanfS=0;
for i=1:n
    meanfS= FS(i)*(i+3)*0.0031941+ meanfS;
end;
meanfS =meanfS*0.0031941;
%% calculate variance
vfS=0;
for i=1:n
    vfS= FS(i)*((i+3)*0.0031941)^2*0.0031941 + vfS;
end;
VarS =vfS- meanfS^2;
VarS

AZ=[
0.9612340.0387660      0      0      0      0      0;
0      0.9625990.0374010      0      0      0      0;
0      0      0.9625990.0374010      0      0      0;
0      0      0      0.9602785      0.0397215      0      0;
0      0      0      0      0.9602785      0.0397215      0;
0      0      0      0      0      0.9602785      0.0397215;
0      0      0      0      0      0      0.9191920.080808;
0      0      0      0      0      0      0      1
];

n=999;
BZ= zeros(1,n);
FZ= zeros(1,n);
CZ =AZ*AZ;
for i=1:n
    CZ =CZ*AZ;
    BZ(i) = CZ(1, 8) ;
end;
%% calculate F(t)
for i=2:n

```

```

                                FZ (i-1) = ( BZ(i)-BZ(i-1) )/ (0.0031941);
                                end;
                                meanfZ=0;
                                for i=1:n
                                    meanfZ= FZ(i)*(i+3)*0.0031941+ meanfZ;
                                end;
                                meanfZ =meanfZ*0.0031941;
                                %% calculate variance
                                vfZ=0;
                                for i=1:n
                                    vfZ= FZ(i)*((i+3)*0.0031941)^2*0.0031941 + vfZ;
                                end;
                                VarZ =vfZ- meanfZ^2;
                                VarZ
                                %% calculate mean and variance
                                QZ=AZ;
                                QZ(:,8)=[];
                                QZ(8,:)=[];
                                IZ=eye(7);
                                NZ=inv(IZ-QZ);
                                EZ=[1; 1; 1; 1; 1;1;1];
                                MeanTimeZ=NZ*EZ;
                                SQZ=MeanTimeZ.^2;
                                VarianceZ =(2*NZ-IZ)*MeanTimeZ-SQZ;
                                MeanTimeZ= MeanTimeZ*0.0031941;
                                VarianceZ= VarianceZ*0.0031941^2;
                                A=[
                                0.967463951      0.016268025      0      0      0.016268025      0      0
                                0      0;
                                0      0.943204526      0.056795474      0      0      0      0      0
                                0;
                                0      0      0.97285015      0.02714985      0      0      0      0
                                0;
                                0      0      0      0.958837624      0      0      0      0.041162376
                                0;
                                0      0      0      0      0.943204526      0.056795474      0      0
                                0;
                                0      0      0      0      0      0.97285015      0.02714985      0
                                0;
                                0      0      0      0      0      0      0.958837624      0.041162376
                                0;
                                0      0      0      0      0      0      0      0.9904177
                                0.0095823
                                0      0      0      0      0      0      0      0      1

```

```

];
n=999;
B= zeros(1,n);
FH= zeros(1,n);
C =A*A;
for i=1:n
    C =C*A;
    B(i) = C(1, 9) ;
end;
%% calculate F(t)
for i=2:n
    FH (i-1) = ( B(i)-B(i-1) )/(0.0031941);
end;
meanfH=0;
for i=1:n
    meanfH= FH(i)*(i+3)*0.0031941+ meanfH;
end;
meanfH =meanfH*0.0031941;
%% calculate variance
vfH=0;
for i=1:n
    vfH= FH(i)*((i+3)*0.0031941)^2*0.0031941 + vfH;
end;
    VarH =vfH- meanfH^2;
VarH
%% calculate mean and variance
QH=A;
QH(:,9)=[];
QH(9,:)=[];
IH=eye(8);
NH=inv(IH-QH);
EH=[1; 1; 1; 1; 1; 1; 1; 1];
MeanTimeH=NH*EH;
SQH=MeanTimeH.^2;
VarianceH =(2*NH-IH)*MeanTimeH-SQH;
MeanTimeH= MeanTimeH*0.0031941;
VarianceH= VarianceH*0.0031941^2;
%% set x asix as n*delta T
xx=zeros(1,n);
ax=zeros(1,n);
%%%%%%%%%%%%%%
AlphaS=0.48484^2/0.049679; LambdaS= 0.48484/0.049679;
YS=gamma(AlphaS);
FF=zeros(1,n);

```

```

for i=1:n
    xx(i)=i;
    ax(i)=xx(i)*0.0031941;
    FFS(i)=( LambdaS*exp((-1)*LambdaS*ax(i))*( LambdaS*ax(i))^(AlphaS-1))/YS;
end;
%%%%%%%%%%%%%%%%%%%%%%%%%%%%%%%%%%%%%%%%%%%%%%%%%%%%%%%%%%%%%%%%%%%%%%%%
AlphaZ= 0.53396^2/0.040631; LambdaZ= 0.53396/0.040631;
YZ=gamma(AlphaZ);
FFZ=zeros(1,n);
for i=1:n
    xx(i)=i;
    ax(i)=xx(i)*0.0031941;
    FFZ(i)=( LambdaZ*exp((-1)*LambdaZ*ax(i))*( LambdaZ*ax(i))^(AlphaZ-1))/YZ;
end;
%%%%%%%%%%%%%%%%%%%%%%%%%%%%%%%%%%%%%%%%%%%%%%%%%%%%%%%%%%%%%%%%%%%%%%%%
AlphaH= 0.6822^2/0.13986; LambdaH= 0.6822/0.13986;
YH=gamma(AlphaH);
FFH=zeros(1,n);
for i=1:n
    xx(i)=i;
    ax(i)=xx(i)*0.0031941;
    FFH(i)=( LambdaH*exp((-1)*LambdaH*ax(i))*( LambdaH*ax(i))^(AlphaH-1))/YH;
end;
xaxis=ax;
% FS is the value from deltaP/deltat, FFS is the value from % lambda
function
plot (xaxis, FS, xaxis, FZ, '-.b', xaxis, FH, '-ro' );
%% Plot Figures with different line properties-line style
%plot(xaxis, BS , xaxis, FS , xaxis, BZ, '-.b', xaxis, FZ, xaxis, B, '-ro' , xaxis, FH);
h=legend('Straight Channel Microreactor','Zigzag Channel Microreactor ','Omega
Channel Microreactor ',3);
xlabel(' t' )
ylabel(' f(t)')
title(' Resident Time Distribution Function for Compartment 1x1 ' )
%text(1,-1/3,'\itNote the difference among each reactor set')

```

APPENDIX B

SOURCE CODES

Cumulative Probability of a Molecule Exiting the Three Microreactors &

Residence Time Density Function.

Compartment 1x3

AS=[

```

0.96875337 0.03124663 0 0 0 0 0 0 0
    0 0 0 0 0;
0 0.970489293 0.029510707 0 0 0 0 0
    0 0 0 0 0 0;
0 0 0.970489293 0.029510707 0 0 0 0
    0 0 0 0 0;
0 0 0 0.96875337 0.03124663 0 0 0
    0 0 0 0 0;
0 0 0 0 0.96875337 0.03124663 0 0
    0 0 0 0 0;
0 0 0 0 0 0.96875337 0.03124663 0
    0 0 0 0 0;
0 0 0 0 0 0 0.96875337 0.03124663
    0.03124663 0 0 0 0;
0 0 0 0 0 0 0 0 0.962504043
    0.037495957 0 0 0;
0 0 0 0 0 0 0 0 0
    0.96875337 0.03124663 0 0;
0 0 0 0 0 0 0 0 0 0
    0.967017446 0.032982554 0;
0 0 0 0 0 0 0 0 0 0
    0 0.861126087 0.138873913;
0 0 0 0 0 0 0 0 0 0
    0 0 1

```

];

```

n=2000;
BS= zeros(1,n);
FS= zeros(1,n);
CS =AS*AS;
for i=1:n
    CS =CS*AS;
    BS(i) = CS(1, 14) ;
end;
%%% calculate F(t)
for i=2:n
    FS (i-1) = ( BS(i)-BS(i-1) )/ 0.0031941;
    end;
meanfS=0;
for i=1:n
    meanfS= FS(i)*(i+3)*0.0031941+meanfS;
end;
meanfS
%%% calculate mean and variance
Q=AS;
Q(:,14)=[];
Q(14,:)=[];
I=eye(13);
N=inv(I-Q);
E=zeros (13,1);
    for i=1:13
        E(i)=1
    end
    MeanTimeS=N*E;
SQ=MeanTimeS.^2;
VarianceS =(2*N-I)*MeanTimeS-SQ;
MeanTimeS= MeanTimeS*0.0031941;
VarianceS= VarianceS*0.0031941^2;
FS= zeros(1,n);
%%% calculate mean and get F- the density function
for i=2:n
    FS (i-1) = ( BS(i)-BS(i-1) )/ (0.0031941);
    end;
%%% test that sum of f(t)* 0.0031941=1
sum=zeros(1,1);
for i=1:n
    sum = FS(i)* 0.0031941+sum;
    end;
sum
%%% sum=1

```



```

0      0 0 0      0      0.96256 0.03744 0;
0      0 0 0      0      0      0      0      0      0
      0 0 0      0      0      0.95632 0.04368;
0      0 0 0      0      0      0      0      0      0
      0 0 0      0      0      0      1
];
n=2000;
BZ= zeros(1,n);
FZ= zeros(1,n);
CZ =AZ*AZ;
for i=1:n
    CZ =CZ*AZ;
    BZ(i) = CZ(1, 18) ;
end;
%% calculate F(t)
for i=2:n
    FZ (i-1) = ( BZ(i)-BZ(i-1) )/ 0.0031941;
end;
meanfZ=0;
for i=1:n
    meanfZ= FZ(i)*(i+3)*0.0031941+meanfZ;
end;
meanfZ
%% calculate mean and variance
QZ=AZ;
QZ(:,18)=[];
QZ(18,:)=[];
IZ=eye(17);
NZ=inv(IZ-QZ);
EZ=zeros (17,1);
for i=1:17
    EZ(i)=1
end;
MeanTimeZ=NZ*EZ;
SQZ=MeanTimeZ.^2;
VarianceZ =(2*NZ-IZ)*MeanTimeZ-SQZ;
MeanTimeZ= MeanTimeZ*0.0031941;
VarianceZ= VarianceZ*0.0031941^2;
%% calculate F(t)
for i=2:n
    FZ (i-1) = ( BZ(i)-BZ(i-1) )/ (0.0031941);
end;
meanfZ=0;
for i=1:n
    meanfZ= FZ(i)*(i+3)*0.0031941+ meanfZ;
end;

```

```

meanfZ =meanfZ*0.0031941;
%% calculate variance
vfZ=0;
for i=1:n
    vfZ= FZ(i)*((i+3)*0.0031941)^2*0.0031941 + vfZ;
end;
VarZ =vfZ- meanfZ^2;
VarZ
A=[
0.98468015 0.007659925 0 0 0.007659925 0 0 0 0 0
0 0 0 0 0 0;
0 0.964502829 0.035497171 0 0 0 0 0 0 0
0 0 0 0 0 0;
0 0 0.9840295 0.0159705 0 0 0 0 0 0
0 0 0 0 0 0;
0 0 0 0.978916832 0 0 0.021083168 0 0 0
0 0 0 0 0;
0 0 0 0.964502829 0.035497171 0 0 0 0 0
0 0 0 0 0;
0 0.9840295 0.0159705 0 0 0 0 0 0 0
0 0 0 0 0;
0 0 0 0 0.978916832 0.021083168 0 0 0 0
0 0 0 0 0;
0 0.007659925 0 0.98468015 0.007659925
0 0 0 0 0;
0 0.964502829 0.035497171 0 0 0 0.964502829 0 0 0
0.035497171 0 0 0 0;
0 0 0 0 0;
0.978916832 0.021083168 0 0 0 0 0 0 0 0
0.98468015 0 0 0 0.007659925 0.007659925
0 0 0 0 0;
0 0 0 0 0;
0.978916832 0.021083168 0 0 0 0 0 0 0 0
0.98468015 0 0 0 0.007659925 0.007659925
0 0 0 0 0;
0 0 0 0 0

```

```

0 0.964502829 0.035497171 0 0 0 0 0
0 0 0 0;
0 0 0 0 0 0 0 0 0
0 0 0.9840295 0.0159705 0 0 0 0
0 0 0 0;
0 0 0 0 0 0 0 0 0
0.021083168 0 0 0.978916832 0 0 0
0 0 0 0 0;
0 0 0 0 0 0 0 0 0
0 0 0 0 0.964502829 0 0.035497171 0
0 0 0 0;
0 0 0 0 0 0 0 0 0
0 0 0 0 0 0.964502829 0 0.035497171
0 0 0 0;
0 0 0 0 0 0 0 0 0
0 0 0 0 0 0 0.9840295 0
0.0159705 0 0 0;
0 0 0 0 0 0 0 0 0
0 0 0 0 0 0 0 0.9840295 0
0.0159705 0 0;
0 0 0 0 0 0 0 0 0
0 0 0 0 0 0 0 0 0.978916832
0 0.021083168 0;
0 0 0 0 0 0 0 0 0
0 0 0 0 0 0 0 0 0
0.989659101 0.010340899 0;
0 0 0 0 0 0 0 0 0
0 0 0 0 0 0 0 0 0
0.989659101 0.010340899;
0 0 0 0 0 0 0 0 0
0 0 0 0 0 0 0 0 0
0 1

```

```

];
n=2000;
B= zeros(1,n);
FH= zeros(1,n);
C =A*A;
for i=1:n
    C =C*A;
    B(i) = C(1, 23) ;
end;
%% calculate F(t)
for i=2:n
    FH (i-1) = ( B(i)-B(i-1) )/(0.0031941);

```

```

end;
meanfH=0;
for i=1:n
    meanfH= FH(i)*(i+3)*0.0031941+ meanfH;
end;
meanfH =meanfH*0.0031941;
%% calculate variance
vfH=0;
for i=1:n
    vfH= FH(i)*((i+3)*0.0031941)^2*0.0031941 + vfH;
end;
VarH =vfH- meanfH^2;
VarH
%% calculate mean and variance
QH=A;
QH(:,23)=[];
QH(23,:)=[];
IH=eye(22);
NH=inv(IH-QH);
EH=zeros (22,1);
    for i=1:22
        EH(i)=1;
    end;
MeanTimeH=NH*EH;
SQH=MeanTimeH.^2;
VarianceH =(2*NH-IH)*MeanTimeH-SQH;
MeanTimeH
VarianceH
MeanTimeH= MeanTimeH*0.0031941;
VarianceH= VarianceH*0.0031941^2;
%% set x asix as n*delta T
xx=zeros(1,n);
ax=zeros(1,n);
for i=1:n
    xx(i)=i;
    ax(i)=xx(i)*0.0031941;
end;
xaxis=ax;
%% set x asix as n*delta T
xx=zeros(1,n);
ax=zeros(1,n);
%% %% %% %% %% %% %% %% %% %% %% %% %% %% %%
AlphaS=1.2393^2/ 0.12023 ; LambdaS= 1.2393/ 0.12023 ;
YS=gamma(AlphaS);
FF=zeros(1,n);

```

```

for i=1:n
    xx(i)=i;
    ax(i)=xx(i)*0.0031941;
    FFS(i)=( LambdaS*exp((-1)*LambdaS*ax(i))*( LambdaS*ax(i))^(AlphaS-1))/YS;
end;
%%%%%%%%%%%%%%%%%%%%%%%%%%%%%%%%%%%%%%%%%%%%%%%%%%%%%%%%%%%%%%%%%%%%%%%%
AlphaZ= 1.3919^2/ 0.10981; LambdaZ= 1.3919/ 0.10981;
YZ=gamma(AlphaZ);
FFZ=zeros(1,n);
for i=1:n
    xx(i)=i;
    ax(i)=xx(i)*0.0031941;
    FFZ(i)=( LambdaZ*exp((-1)*LambdaZ*ax(i))*( LambdaZ*ax(i))^(AlphaZ-1))/YZ;
end;
%%%%%%%%%%%%%%%%%%%%%%%%%%%%%%%%%%%%%%%%%%%%%%%%%%%%%%%%%%%%%%%%%%%%%%%%
AlphaH= 2.3374^2/ 0.47365; LambdaH= 2.3374/ 0.47365;
YH=gamma(AlphaH);
FFH=zeros(1,n);
for i=1:n
    xx(i)=i;
    ax(i)=xx(i)*0.0031941;
    FFH(i)=( LambdaH*exp((-1)*LambdaH*ax(i))*( LambdaH*ax(i))^(AlphaH-1))/YH;
end;
xaxis=ax;
% FS is the value from deltaP/deltat, FFS is the value from % lambda function
plot (xaxis, FS, xaxis, FZ, '-.b', xaxis, FH, '-ro' );
%% Plot Figures with different line properties-line style
%plot(xaxis, BS , xaxis, FS , xaxis, BZ, '-.b', xaxis, FZ, xaxis, B, '-ro' , xaxis, FH);
h=legend('Straight Channel Microreactor','Zigzag Channel Microreactor ','Omega
Channel Microreactor ' ,3);
xlabel(' t ')
ylabel(' f(t)')
title(' Resident Time Distribution Function for Compartment 1x3 ')
%text(1,-1/3, '{\itNote the difference among each reactor set}')

```

APPENDIX C

SOURCE CODES

Cumulative Probability of a Molecule Exiting the Three Microreactors

&

Residence Time Density Function.

Compartment 2x2

```
% 2x2 Str has 10x10 elements
```

```
AS=[
```

```
0.9885925      0.0114075      0      0      0      0      0      0
      0      0;
0      0.9885925      0.0114075      0      0      0      0      0
      0      0;
0      0      0.9885925      0.0114075      0      0      0      0
      0      0;
0      0      0      0.9885925      0.0114075      0      0      0
      0      0;
0      0      0      0      0.9885925      0.0114075      0      0
      0      0;
0      0      0      0      0      0.987940643      0.012059357      0
      0      0;
0      0      0      0      0      0      0.987940643      0.012059357
      0      0;
0      0      0      0      0      0      0      0.979140571
      0.020859429      0;
0      0      0      0      0      0      0      0      0.977185
      0.022815;
0      0      0      0      0      0      0      0      0      1
```

```
];
```

```
n=2743;
```

```
BS= zeros(1,n);
```

```
FS= zeros(1,n);
```

```
CS =AS*AS;
```

```
for i=1:n
```

```
    CS =CS*AS;
```

```
    BS(i) = CS(1, 10)
```

```
end;
```

```

%% calculate F(t)
for i=2:n
    FS (i-1) = ( BS(i)-BS(i-1) )/ 0.0031941;
end;
meanfS=0;
for i=1:n
    meanfS= FS(i)*(i+3)*0.0031941+meanfS;
end;
meanfS
%% calculate mean and variance
Q=AS;
Q(:,10)=[];
Q(10,:)=[];
I=eye(9);
N=inv(I-Q);
E=[1; 1; 1; 1; 1;1;1;1;1];
MeanTimeS=N*E;
SQ=MeanTimeS.^2;
VarianceS =(2*N-I)*MeanTimeS-SQ;
MeanTimeS= MeanTimeS*0.0031941;
VarianceS= VarianceS*0.0031941^2;
FS= zeros(1,n);
%% calculate mean and get F- the density function
for i=2:n
    FS (i-1) = ( BS(i)-BS(i-1) )/ (0.0031941);
end;
%% test that sum of f(t)* 0.0031941=1
sum=zeros(1,1);
for i=1:n
    sum = FS(i)* 0.0031941+sum;
end;
sum
%% sum=1
meanfS=0;
for i=1:n
    meanfS= FS(i)*(i+3)*0.0031941+ meanfS;
end;
meanfS =meanfS*0.0031941;
%% calculate variance
vfS=0;
for i=1:n
    vfS= FS(i)*((i+3)*0.0031941)^2*0.0031941 + vfS;
end;
VarS =vfS- meanfS^2;
VarS

```

```

AZ=[
0.9863110.0136890      0      0      0      0      0
      0      0      0      0;
0      0.9863110.0136890      0      0      0      0
      0      0      0      0;
0      0      0.9863110.0136890      0      0      0
      0      0      0      0;
0      0      0      0.9863110.0136890      0      0
      0      0      0      0;
0      0      0      0      0.9863110.0136890      0
      0      0      0      0;
0      0      0      0      0      0.9863110.0136890
      0      0      0      0;
0      0      0      0      0      0      0.9863110.0136890
      0      0;
0      0      0      0      0      0      0      0.986311
      0.0136890      0;
0      0      0      0      0      0      0      0      0
      0.9863110.0136890;
0      0      0      0      0      0      0      0      0      0
      0.9840295      0.0159705;
0      0      0      0      0      0      0      0      0      0
      0      1
];

n=2743;
BZ= zeros(1,n);
FZ= zeros(1,n);
CZ =AZ*AZ;
for i=1:n
    CZ =CZ*AZ;
    BZ(i) = (CZ(1, 12));
end;
%% calculate F(t)
for i=2:n
    FZ (i-1) = ( BZ(i)-BZ(i-1) )/ 0.0031941;
end;
meanfZ=0;
for i=1:n
    meanfZ= FZ(i)*(i+3)*0.0031941+meanfZ;
end;
meanfZ

```

```

%% calculate mean and variance
QZ=AZ;
QZ(:,12)=[];
QZ(12,:)=[];
IZ=eye(11);
NZ=inv(IZ-QZ);
EZ=[1; 1; 1; 1; 1; 1; 1; 1; 1; 1; 1];
MeanTimeZ=NZ*EZ;
SQZ=MeanTimeZ.^2;
VarianceZ =(2*NZ-IZ)*MeanTimeZ-SQZ;
MeanTimeZ= MeanTimeZ*0.0031941;
VarianceZ= VarianceZ*0.0031941^2;
%% calculate F(t)
for i=2:n
    FZ (i-1) = ( BZ(i)-BZ(i-1) )/ (0.0031941);
end;
meanfZ=0;
for i=1:n
    meanfZ= FZ(i)*(i+3)*0.0031941+ meanfZ;
end;
meanfZ =meanfZ*0.0031941;
%% calculate variance
vfZ=0;
for i=1:n
    vfZ= FZ(i)*((i+3)*0.0031941)^2*0.0031941 + vfZ;
end;
VarZ =vfZ- meanfZ^2;
VarZ
% 2x2 Omega has 29x29 elements
A=[
0.9929020.0035490      0      0      0      0      0
      0      0.0035490      0      0      0      0      0
      0      0      0      0      0      0      0      0
      0      0      0      0;
0      0.972247666      0.027752334      0      0      0      0      0
      0      0      0      0      0      0      0      0
      0      0      0      0      0      0      0      0
      0      0      0;
0      0      0.993212538      0.006787463      0      0      0      0
      0      0      0      0      0      0      0      0
      0      0      0      0      0      0      0      0
      0      0      0;
0      0      0      0.986446535      0.013553465      0      0      0
      0      0      0      0      0      0      0      0
      0      0      0      0      0      0      0      0

```

0	0	0	0;						
0	0	0	0	0.9904177	0.00479115	0	0	0	0
	0	0	0	0	0.00479115	0	0	0	0
	0	0	0	0	0	0	0	0	0
	0	0	0	0;					
0	0	0	0	0	0.972247666	0.027752334	0	0	0
	0	0	0	0	0	0	0	0	0
	0	0	0	0	0	0	0	0	0
	0	0	0;						
0	0	0	0	0	0	0.993212538	0.006787463		
	0	0	0	0	0	0	0		
	0	0	0	0	0	0	0	0	0
	0	0	0	0	0;				
0	0	0	0	0	0	0	0.986446535		
	0.013553465	0	0	0	0	0	0	0	0
	0	0	0	0	0	0	0	0	0
	0	0	0	0;					
0	0	0	0	0	0	0	0	0.99520885	
	0	0	0	0	0	0	0	0	0
	0	0	0	0	0	0	0	0	0
	0	0.00479115;							
0	0	0	0	0	0	0	0	0	
	0.972247666	0.027752334		0	0	0	0	0	0
	0	0	0	0	0	0	0	0	0
	0	0	0	0;					
0	0	0	0	0	0	0	0	0	0
	0.994909403	0.003393731		0	0	0	0	0	0
	0	0.001696866	0	0	0	0	0	0	0
	0	0	0	0;					
0	0	0	0	0.013553465	0	0	0	0	0
	0	0	0.986446535	0	0	0	0	0	0
	0	0	0	0	0	0	0	0	0
	0	0	0;						
0	0	0	0	0	0	0	0	0	0
	0	0	0.972247666	0.027752334	0	0	0	0	0
	0	0	0	0	0	0	0	0	0
	0	0	0;						
0	0	0	0	0	0	0	0	0	0
	0	0	0	0.994909403	0.003393731	0	0	0	0
	0	0	0	0	0	0.001696866	0	0	0
	0	0	0	0;					
0	0	0	0	0	0	0	0	0.013553465	
	0	0	0	0	0	0.986446535	0	0	0
	0	0	0	0	0	0	0		
	0	0	0	0	0	0	0;		
0	0	0	0	0	0	0	0	0	0

	0	0	0	0	0	0.9929020	0.003549		
	0	0	0	0	0	0	0	0.003549	
	0	0	0	0;					
0	0	0	0	0	0	0	0	0	0
	0.027752334	0	0	0	0	0	0	0.972247666	
0	0	0	0	0	0	0			
	0	0	0	0	0;				
0	0	0	0	0	0	0	0	0	0
	0	0	0	0	0	0	0	0.993212538	
	0	0	0	0	0	0	0		
	0.006787463	0	0	0;					
0	0	0	0	0	0	0	0	0	0
	0	0	0	0	0	0	0	0	
	0.986446535	0.013553465	0	0	0	0	0	0	0
	0	0	0	0;					
0	0	0	0	0	0	0	0	0	0
	0	0	0	0	0	0	0	0	0
	0.9904177	0.00479115	0	0	0	0	0	0	0
	0.00479115	0	0;						
0	0	0	0	0	0	0	0	0	0
	0	0	0	0.027752334	0	0	0	0	0
	0	0	0.972247666	0	0	0	0	0	0
	0	0	0;						
0	0	0	0	0	0	0	0	0	0
	0	0	0	0	0	0	0	0	0
	0	0	0.996606269	0	0	0	0	0	0
	0.003393731	0;							
0	0	0	0	0	0	0	0	0	0
	0	0	0	0	0	0	0	0	0
	0	0	0	0.986446535	0.013553465	0	0	0	
	0	0	0;						
0	0	0	0	0	0	0	0	0	0
	0	0	0	0	0	0	0	0	0
	0	0	0	0	0.99520885	0	0	0	0
	0	0.00479115;							
0	0	0	0	0	0	0	0	0	0
	0	0	0	0	0	0	0	0.027752334	
	0	0	0	0	0	0	0.972247666	0	
0	0	0;							
0	0	0	0	0	0	0	0	0	0
	0	0	0	0	0	0	0	0	0
	0.013553465	0	0	0	0	0	0	0.986446535	
0	0	0;							
0	0	0	0	0	0	0	0	0	0
	0	0	0	0	0	0	0	0	0


```

%% set x asix as n*delta T
xx=zeros(1,n);
ax=zeros(1,n);
for i=1:n
    xx(i)=i;
    ax(i)=xx(i)*0.0031941;
end;
xaxis=ax;
%% set x asix as n*delta T
xx=zeros(1,n);
ax=zeros(1,n);
%%%%%%%%%%%%%%%%%%%%%%%%%%%%%%%%%%%%%%%%%%%%%%%%%%%%%%%%%%%%%%%%%%%%%%%%
AlphaS=1.2393^2/ 0.12023 ; LambdaS= 1.2393/ 0.12023 ;
YS=gamma(AlphaS);
FF=zeros(1,n);
for i=1:n
    xx(i)=i;
    ax(i)=xx(i)*0.0031941;
    FFS(i)=( LambdaS*exp((-1)*LambdaS*ax(i))*( LambdaS*ax(i))^(AlphaS-1))/YS;
end;
%%%%%%%%%%%%%%%%%%%%%%%%%%%%%%%%%%%%%%%%%%%%%%%%%%%%%%%%%%%%%%%%%%%%%%%%
AlphaZ= 1.3919^2/ 0.10981; LambdaZ= 1.3919/ 0.10981;
YZ=gamma(AlphaZ);
FFZ=zeros(1,n);
for i=1:n
    xx(i)=i;
    ax(i)=xx(i)*0.0031941;
    FFZ(i)=( LambdaZ*exp((-1)*LambdaZ*ax(i))*( LambdaZ*ax(i))^(AlphaZ-1))/YZ;
end;
%%%%%%%%%%%%%%%%%%%%%%%%%%%%%%%%%%%%%%%%%%%%%%%%%%%%%%%%%%%%%%%%%%%%%%%%
AlphaH= 2.3374^2/ 0.47365; LambdaH= 2.3374/ 0.47365;
YH=gamma(AlphaH);
FFH=zeros(1,n);
for i=1:n
    xx(i)=i;
    ax(i)=xx(i)*0.0031941;
    FFH(i)=( LambdaH*exp((-1)*LambdaH*ax(i))*( LambdaH*ax(i))^(AlphaH-1))/YH;
end;
xaxis=ax;
% FS is the value from deltaP/deltat, FFS is the value from % lambda function
plot (xaxis, FS, xaxis, FZ, '-.b', xaxis, FH, '-ro' );
%% Plot Figures with different line properties-line style
%plot(xaxis, BS , xaxis, FS , xaxis, BZ, '-.b', xaxis, FZ, xaxis, B, '-ro' , xaxis, FH);
h=legend('Straight Channel Microreactor','Zigzag Channel Microreactor ','Omega
Channel Microreactor ',3);

```

```
xlabel(' t ' )  
ylabel(' f(t)')  
title(' Resident Time Distribution Function for Compartment 2x2 ' )  
%text(1,-1/3,'\itNote the difference among each reactor set')
```

APPENDIX D


```

BS= zeros(1,n);
CS =AS*AS;
for i=1:n
    CS =CS*AS;
    BS(i) = (CS(1, 14)) ;
end;
%% calculate mean and variance
Q=AS;
Q(:,14)=[];
Q(14,:)=[];
I=eye(13);
N=inv(I-Q);
E=zeros(13,1);
for i=1:13
    E(i)=1;
end;
MeanTimeS=N*E;
SQ=MeanTimeS.^2;
VarianceS =(2*N-I)*MeanTimeS-SQ;
MeanTimeS= MeanTimeS*0.0031941;
VarianceS= VarianceS*0.0031941^2;
FS= zeros(1,n);
%% calculate mean variance and get F- the density function
for i=2:n
    FS (i-1) = ( BS(i)-BS(i-1) )/ (0.0031941);
    end;
%% test that sum of f(t)* 0.0031941=1
sum=zeros(1,1);
for i=1:n
    sum = FS(i)* 0.0031941+sum;
    end;
sum
%% sum=1
meanfS=0;
for i=1:n
    meanfS= FS(i)*(i+3)*0.0031941+ meanfS;
end;
meanfS =meanfS*0.0031941;
%% calculate variance
vfS=0;
for i=1:n
    vfS= FS(i)*((i+3)*0.0031941)^2*0.0031941 + vfS;
end;

VarS =vfS- meanfS^2;

```

VarS

%% 2x3 zig

AZ=[

0.990720581	0.009279419	0	0	0	0	0	0	0
0	0	0	0	0	0	0	0	0
0	0;							
0	0.990720581	0.009279419	0	0	0	0	0	0
0	0	0	0	0	0	0	0	0
0	0;							
0	0	0.990720581	0.009279419	0	0	0	0	0
0	0	0	0	0	0	0	0	0
0	0;							
0	0	0	0.990720581	0.009279419	0	0	0	0
0	0	0	0	0	0	0	0	0
0	0;							
0	0	0	0	0.990720581	0.009279419	0	0	0
0	0	0	0	0	0	0	0	0
0	0;							
0	0	0	0	0	0.990720581	0.009279419	0	0
0	0	0	0	0	0	0	0	0
0	0;							
0	0	0	0	0	0	0.990720581	0.009279419	0
0	0	0	0	0	0	0	0	0
0	0;							
0	0	0	0	0	0	0	0.990720581	0
0	0.009279419	0	0	0	0	0	0	0
0	0	0	0;					
0	0	0	0	0	0	0	0	0.990720581
0	0.009279419	0	0	0	0	0	0	
0	0	0	0	0;				
0	0	0	0	0	0	0	0	0
0	0.990720581	0.009279419	0	0	0	0	0	0
0	0	0	0;					
0	0	0	0	0	0	0	0	0
0	0.990720581	0.009279419	0	0	0	0	0	0
0	0	0;						
0	0	0	0	0	0	0	0	0
0	0	0.990720581	0.009279419	0	0	0	0	0
0	0	0;						
0	0	0	0	0	0	0	0	0
0	0	0	0.990720581	0.009279419	0	0	0	0
0	0	0;						
0	0	0	0	0	0	0	0	0
0	0	0	0	0.990720581	0.009279419	0	0	0
0	0	0;						
0	0	0	0	0	0	0	0	0
0	0	0	0	0.990720581	0.009279419	0	0	0
0	0	0;						
0	0	0	0	0	0	0	0	0
0	0	0	0	0	0	0	0	0

```

0      0      0      0      0.990720581      0.009279419      0
0      0;
0      0      0      0      0      0      0      0      0
0      0      0      0      0      0.990720581      0.009279419
0      0;
0      0      0      0      0      0      0      0      0
0      0      0      0      0      0      0      0.990720581
0.009279419      0;
0      0      0      0      0      0      0      0      0
0      0      0      0      0      0      0      0.988069318
0.011930682;
0      0      0      0      0      0      0      0      0
0      0      0      0      0      0      0      0      1

];
n=7000;
BZ= zeros(1,n);
CZ =AZ*AZ;
for i=1:n
    CZ =CZ*AZ;
    BZ(i) = CZ(1, 19) ;
end;
%% calculate mean and variance
QZ=AZ;
QZ(:,19)=[];
QZ(19,:)=[];
IZ=eye(18);
NZ=inv(IZ-QZ);
EZ=[ 1; 1; 1; 1; 1; 1;
     1; 1; 1; 1; 1; 1;
     1; 1; 1; 1; 1; 1];
MeanTimeZ=NZ*EZ;
SQZ=MeanTimeZ.^2;
VarianceZ =(2*NZ-IZ)*MeanTimeZ-SQZ;
MeanTimeZ= MeanTimeZ*0.0031941;
VarianceZ= VarianceZ*0.0031941^2;
FZ= zeros(1,n);
%% calculate mean variance and get F- the density function
for i=2:n
    FZ (i-1) = ( BZ(i)-BZ(i-1) )/ (0.0031941);
end;
%% test that sum of f(t)* 0.0031941=1
sum=zeros(1,1);
for i=1:n
    sum = FZ(i)* 0.0031941+sum;
end;

```

```

sum
%% sum=1
meanfZ=0;
for i=1:n
    meanfZ= FZ(i)*(i+3)*0.0031941+ meanfZ;
end;
meanfZ =meanfZ*0.0031941;
%% calculate variance
vfZ=0;
for i=1:n
    vfZ= FZ(i)*((i+3)*0.0031941)^2*0.0031941 + vfZ;
end;
VarZ =vfZ- meanfZ^2;
VarZ
%% 2x3 omega has 42x42 elements
A=[
0.99603695      0.001981525      0      0      0      0      0      0
      0      0      0      0      0      0.001981525      0      0
      0      0      0      0      0      0      0      0
      0      0      0      0      0      0      0      0
      0      0      0      0      0      0      0      0;
0      0.988382744      0.011617256      0      0      0      0      0
      0      0      0      0      0      0      0      0
      0      0      0      0      0      0      0      0
      0      0      0      0      0      0      0      0
      0      0      0      0      0      0      0      0;
0      0      0.9968059      0.0031941      0      0      0      0
      0      0      0      0      0      0      0      0
      0      0      0      0      0      0      0      0
      0      0      0      0      0      0      0      0
      0      0      0      0      0      0      0      0;
0      0      0      0.989960396      0.010039604      0      0      0
      0      0      0      0      0      0      0      0
      0      0      0      0      0      0      0      0
      0      0      0      0      0      0      0      0
      0      0      0      0      0      0      0      0;
0      0      0      0.994410325      0.002794838      0      0
      0      0      0      0      0      0      0      0
      0.002794838      0      0      0      0      0      0      0
      0      0      0      0      0      0      0      0
      0      0      0      0      0      0      0      0;
0      0      0      0      0.988382744      0.011617256      0
      0      0      0      0      0      0      0      0
      0      0      0      0      0      0      0      0
      0      0      0      0      0      0      0      0
      0      0      0      0      0      0      0      0
      0      0      0      0      0      0      0      0;

```

0	0	0	0	0	0	0.9968059	0.0031941		
	0	0	0	0	0	0	0	0	0
	0	0	0	0	0	0	0	0	0
	0	0	0	0	0	0	0	0	0
	0	0	0	0	0	0	0;		
0	0	0	0	0	0	0	0.989960396		
	0.010039604	0	0	0	0	0	0	0	0
	0	0	0	0	0	0	0	0	0
	0	0	0	0	0	0	0	0	0
	0	0	0	0	0	0	0	0;	
0	0	0	0	0	0	0	0	0.99603695	
	0.001981525	0	0	0	0	0	0	0	0
	0	0	0.001981525	0	0	0	0	0	0
	0	0	0	0	0	0	0	0	0
	0	0	0	0	0	0	0	0;	
0	0	0	0	0	0	0	0	0	
	0.988382744	0.011617256	0	0	0	0	0	0	0
	0	0	0	0	0	0	0	0	0
	0	0	0	0	0	0	0	0	0
	0	0	0	0	0	0	0	0;	
0	0	0	0	0	0	0	0	0	0
	0.9968059	0.0031941	0	0	0	0	0	0	0
	0	0	0	0	0	0	0	0	0
	0	0	0	0	0	0	0	0	0
	0	0	0	0	0	0	0;		
0	0	0	0	0	0	0	0	0	0
	0	0.997205163	0.002794838	0	0	0	0	0	0
	0	0	0	0	0	0	0	0	0
	0	0	0	0	0	0	0	0	0
	0	0	0	0	0	0	0;		
0	0	0	0	0	0	0	0	0	0
	0	0	0.997205163	0	0	0	0	0	0
	0	0	0	0	0	0	0	0	0
	0	0	0	0	0	0	0	0	0
	0	0	0	0	0	0.002794838;			
0	0	0	0	0	0	0	0	0	0
	0	0	0	0.988382744	0.011617256	0	0	0	0
	0	0	0	0	0	0	0	0	0
	0	0	0	0	0	0	0	0	0
	0	0	0	0	0	0	0;		
0	0	0	0	0	0	0	0	0	0
	0	0	0	0	0.9936118	0.0031941			0
	0	0	0	0	0	0	0	0	0
	0.0031941	0	0	0	0	0	0	0	0
	0	0	0	0	0	0	0	0;	

0	0	0	0	0.010039604	0	0	0	0
	0	0	0	0	0	0	0.989960396	0
	0	0	0	0	0	0	0	0
	0	0	0	0	0	0	0	0
	0	0	0	0	0	0	0;	0
0	0	0	0	0	0	0	0	0
	0	0	0	0	0	0	0.988382744	0
	0.011617256	0	0	0	0	0	0	0
	0	0	0	0	0	0	0	0
	0	0	0	0	0	0	0	0;
0	0	0	0	0	0	0	0	0
	0	0	0	0	0	0	0	0.9936118
	0.0031941	0	0	0	0	0	0	0
	0	0	0	0	0	0	0.0031941	0
	0	0	0	0	0	0	0	0;
0	0	0	0	0	0	0	0	0.010039604
0	0	0	0	0	0	0		
	0	0	0.989960396	0	0	0	0	0
	0	0	0	0	0	0	0	0
	0	0	0	0	0	0	0	0;
0	0	0	0	0	0	0	0	0
	0	0	0	0	0	0	0	0
	0.988382744	0.011617256	0	0	0	0	0	0
	0	0	0	0	0	0	0	0
	0	0	0	0	0	0	0;	
0	0	0	0	0	0	0	0	0
	0	0	0	0	0	0	0	0
	0	0.9936118	0.0031941	0	0	0	0	0
	0	0	0	0	0	0	0	0
	0	0	0	0.0031941	0	0	0;	
0	0	0	0	0	0	0	0	0
	0	0	0.02509901	0	0	0	0	0
	0	0	0	0.97490099	0	0	0	0
	0	0	0	0	0	0	0	0
	0	0	0	0	0	0	0;	
0	0	0	0	0	0	0	0	0
	0	0	0	0	0	0	0	0
	0	0	0	0.99603695	0.001981525	0.001981525		
0	0	0	0	0	0	0		
	0	0	0	0	0	0	0	0
	0;							
0	0	0	0	0	0	0	0	0
	0	0	0	0	0.011617256	0	0	0
	0	0	0	0	0	0.988382744	0	0
	0	0	0	0	0	0	0	0
	0	0	0	0	0	0	0;	

0	0	0	0	0	0	0	0	0	0
	0	0	0	0	0	0	0	0	0
	0	0	0	0	0	0.988382744	0.011617256		
0	0	0	0	0	0	0			
	0	0	0	0	0	0	0	0	0;
0	0	0	0	0	0	0	0	0	0
	0	0	0	0	0	0	0	0	0
	0	0	0	0	0	0	0.9968059		0
	0.0031941		0	0	0	0	0	0	0
	0	0	0	0	0	0	0;		
0	0	0	0	0	0	0	0	0	0
	0	0	0	0	0	0	0	0	0
	0	0	0	0	0	0	0	0.997205163	
0	0.002794838		0	0	0	0			
	0	0	0	0	0	0	0	0	0;
0	0	0	0	0	0	0	0	0	0
	0	0	0	0	0	0	0	0	0
	0	0	0	0	0	0	0	0	0
	0.997205163		0.002794838		0	0	0	0	0
	0	0	0	0	0	0	0	0;	
0	0	0	0	0	0	0	0	0	0
	0	0	0	0	0	0	0	0	0
	0	0	0	0	0	0	0	0	0
	0.99603695		0.001981525		0.001981525		0	0	0
	0	0	0	0	0	0	0	0;	
0	0	0	0	0	0	0	0	0	0
	0	0	0	0	0	0	0	0	0.011617256
0	0	0	0	0	0	0			
	0	0	0	0	0.988382744		0	0	0
	0	0	0	0	0	0	0	0	0;
0	0	0	0	0	0	0	0	0	0
	0	0	0	0	0	0	0	0	0
	0	0	0	0	0	0	0	0	0
	0	0	0.988382744		0.011617256		0	0	0
	0	0	0	0	0	0	0;		
0	0	0	0	0	0	0	0	0	0
	0	0	0	0	0	0	0	0	0
	0	0	0	0	0	0	0	0	0
	0	0	0	0.9968059		0	0.0031941		0
	0	0	0	0	0	0	0;		
0	0	0	0	0	0	0	0	0	0
	0	0	0	0	0	0	0	0	0
	0	0	0	0	0	0	0	0	0
	0	0	0	0	0.989960396		0	0.010039604	
0	0	0	0	0	0	0;			
0	0	0	0	0	0	0	0	0	0

	0	0	0	0	0	0	0	0	0
	0	0	0	0	0	0	0	0	0
	0	0	0	0	0	0.989960396	0.010039604		
0	0	0	0	0	0	0;			
0	0	0	0	0	0	0	0	0	0
	0	0	0	0	0	0	0	0	0
	0	0	0	0	0	0	0	0	0
	0	0	0	0	0	0	0.99603695		
	0.001981525		0.001981525	0	0	0	0	0;	
0	0	0	0	0	0	0	0	0	0
	0	0	0	0	0	0	0	0	0
	0	0.011617256	0	0	0	0	0	0	0
	0	0	0	0	0	0	0	0	0
	0.988382744	0	0	0	0	0	0	0;	
0	0	0	0	0	0	0	0	0	0
	0	0	0	0	0	0	0	0	0
	0	0	0	0	0	0	0	0	0
	0	0	0	0	0	0	0	0	0
	0.988382744		0.011617256	0	0	0	0	0;	
0	0	0	0	0	0	0	0	0	0
0	0	0	0	0	0	0	0	0	0
	0	0	0	0	0	0	0	0	0
	0	0	0	0	0	0	0	0	0
	0.989960396	0	0.010039604	0	0	0;			
0	0	0	0	0	0	0	0	0	0
	0	0	0	0	0	0	0	0	0
	0	0	0	0	0	0	0	0	0
	0	0	0	0	0	0	0	0	0
	0	0.989960396	0	0.010039604	0;				
0	0	0	0	0	0	0	0	0	0
	0	0	0	0	0	0	0	0	0
	0	0	0	0	0	0	0	0	0
	0	0	0	0	0	0	0	0	0
	0	0	0.989960396	0.010039604	0;				
0	0	0	0	0	0	0	0	0	0
	0	0	0	0	0	0	0	0	0
	0	0	0	0	0	0	0	0	0
	0	0	0	0	0	0	0	0	0
	0	0	0	0.997205163	0.002794838;				
0	0	0	0	0	0	0	0	0	0
	0	0	0	0	0	0	0	0	0
	0	0	0	0	0	0	0	0	0
	0	0	0	0	0	0	0	0	0
	0	0	0	0	1				

```

];
n=7000;
B= zeros(1,n);
C =A*A;
for i=1:n
    C =C*A;
    B(i) = (C(1, 42)) ;
end;
%% calculate mean and variance
QH=A;
QH(:,42)=[];
QH(42,:)=[];
IH=eye(41);
NH=inv(IH-QH);
EH=zeros(41,1);
for i=1:41
    EH(i)=1
end;
MeanTimeH=NH*EH;
SQH=MeanTimeH.^2;
VarianceH =(2*NH-IH)*MeanTimeH-SQH;
MeanTimeH= MeanTimeH*0.0031941;
VarianceH= VarianceH*0.0031941^2;
FH= zeros(1,n);
%% calculate mean variance and get F- the density function
for i=2:n
    FH (i-1) = ( B(i)-B(i-1) )/ (0.0031941);
    end;
%% test that sum of f(t)* 0.0031941=1
sum=zeros(1,1);
for i=1:n
    sum = FH(i)* 0.0031941+sum;
    end;
sum
%% sum=1
meanfH=0;
for i=1:n
    meanfH= FH(i)*(i+3)*0.0031941+ meanfH;
end;
meanfH =meanfH*0.0031941;
%% calculate variance
vfH=0;
for i=1:n
    vfH= FH(i)*((i+3)*0.0031941)^2*0.0031941 + vfH;
end;

```

```

        VarH =vfH- meanfH^2;
VarH
%%% set x asix as n*delta T
xx=zeros(1,n);
ax=zeros(1,n);
for i=1:n
    xx(i)=i;
    ax(i)=xx(i)*0.0031941;
end;
xaxis=ax;
%%% set x asix as n*delta T
xx=zeros(1,n);
ax=zeros(1,n);
%%%%%%%%%%%%%%%%%%%%%%%%%%%%%%%%%%%%%%%%%%%%%%%%%%%%%%%%%%%%%%%%%%%%%%%%
AlphaS=1.2393^2/ 0.12023 ; LambdaS= 1.2393/ 0.12023 ;
YS=gamma(AlphaS);
FF=zeros(1,n);
for i=1:n
    xx(i)=i;
    ax(i)=xx(i)*0.0031941;
    FFS(i)=( LambdaS*exp((-1)*LambdaS*ax(i))*( LambdaS*ax(i))^(AlphaS-1))/YS;
end;
%%%%%%%%%%%%%%%%%%%%%%%%%%%%%%%%%%%%%%%%%%%%%%%%%%%%%%%%%%%%%%%%%%%%%%%%
AlphaZ= 1.3919^2/ 0.10981; LambdaZ= 1.3919/ 0.10981;
YZ=gamma(AlphaZ);
FFZ=zeros(1,n);
for i=1:n
    xx(i)=i;
    ax(i)=xx(i)*0.0031941;
    FFZ(i)=( LambdaZ*exp((-1)*LambdaZ*ax(i))*( LambdaZ*ax(i))^(AlphaZ-1))/YZ;
end;
%%%%%%%%%%%%%%%%%%%%%%%%%%%%%%%%%%%%%%%%%%%%%%%%%%%%%%%%%%%%%%%%%%%%%%%%
AlphaH= 2.3374^2/ 0.47365; LambdaH= 2.3374/ 0.47365;
YH=gamma(AlphaH);
FFH=zeros(1,n);
for i=1:n
    xx(i)=i;
    ax(i)=xx(i)*0.0031941;
    FFH(i)=( LambdaH*exp((-1)*LambdaH*ax(i))*( LambdaH*ax(i))^(AlphaH-1))/YH;
end;
xaxis=ax;
% FS is the value from deltaP/deltat, FFS is the value from % lambda function
plot (xaxis, FS, xaxis, FZ, '-.b', xaxis, FH, '-ro' );
%%% Plot Figures with different line properties-line style
%plot(xaxis, BS , xaxis, FS , xaxis, BZ, '-.b', xaxis, FZ, xaxis, B, '-ro' , xaxis, FH);

```

```
h=legend('Straight Channel Microreactor','Zigzag Channel Microreactor','Omega  
Channel Microreactor ',3);  
xlabel(' t ' )  
ylabel(' f(t)')  
title(' Resident Time Distribution Function for Compartment 2x3 ' )  
%text(1,-1/3,'\itNote the difference among each reactor set')
```

REFERENCES

- [1].S.K. Ajmera, C. Delattre, M. A. Schmidt, and K. F. Jensen, "A novel cross-flow microreactor for kinetic studies of catalytic processes," Fifth International Conference on Microreaction Technology (IMRET5), May2001.
- [2].Stroock, A.D. et al., "Chaotic Mixer for Microchannels," *Science*, 295 (2002) 647~651.
- [3].Ajmera, Sameer K; Delattre, Cyril; Schmidt, Martin A; Jensen, Klavs F. "Microreactors for measuring catalyst activity and determining reaction kinetics," *Stud. Surf. Sci. Catal. (Tokyo Conference on Advanced Catalytic Science and Technology)*. 2002.
- [4].De Mas, Nuria; Günther, Axel; Schmidt, Martin A; Jensen, Klavs F. "Microfabricated Multiphase Reactors for the Selective Direct Fluorination of Aromatics," *Ind. Eng. Chem. Res.* 2003. 42: 698-710.
- [5].Yeong, kay Kin, Gavrielidis, Asterios, Zapf, Ralf, Hessel, Volker. "Catalytic preparation and deactivation issues for nitrobenzene hydrogenation in a microstructured falling film reactor," *Catalysis Today*, 2003, 81: 641-651.
- [6]. *J. of Microelectromechanical Systems*, Vol. 13, No. 1, Feb, 2004.
- [7]. Stroock, A.D., Dertinger, S.K.W., Ajdari, A., Mezic, I., Stone, H.A., Whitesides, G.M., 2002. "Chaotic mixer for microchannels," *Science* 295, 647.
- [8].Adam Reppond, Yu Liang, Ji Fang, and Tianhong Cui, "Integrated Microreactor and Its Components for Dehydrogenation of Cyclohexane to Benzene," *SPIE*, 2001, pp. 17-19.
- [9].Campbell, Stephen. "The Science and engineering of Microelectronics Fabrication," Oxford University Press, 1996. pp 15-64.
- [10]. <http://www.epigem.co.uk/microfluidics-intro.htm>
- [11]. <http://www.azonano.com/details.asp?ArticleID=867>

- [12]. H.Surangalika and R.S.Besser, "Study of Cyclohexene Hydrogenation and Dehydrogenation in a Microreactor," AIChE, 2002, Proceedings of the 6 International Conference on Microreaction Technology (IMRET VI), New Orleans, LA.
- [13]. Srinivasan R, Hsing IM, Berger PE, Jensen KF, Firebaugh SL, Schmidt MA, Harold MP, Lerou JJ, Ryley JF. "Micromachined Reactors for catalytic partial oxidation reactions," AIChE Journal, 1997, Vol. 43, No. 11, pp. 3059-3068.
- [14]. R.S. Besser, X. Ouyang, H. Surangalika, "Hydrogenation and Dehydrogenation in a Microfabricated Catalytic Reactor," Chemical Engineering Science, 2003, 58 (1) 19-26.
- [15]. Shihui Zhao, Dissertation "Nano-scale platinum and ion-cobalt catalysis deposited in microchannel microreactors for use in hydrogenation and dehydrogenation of cyclohexene, selective of oxidation of carbon monoxide and Syn-Gasprocess to higher alkanes," Louisiana Tech University, 2003.
- [16]. Wolfgang Ehrfeld, Volker Hessel, Holger Löwe, Microreactors: New Technology for Modern Chemistry, 1st edition, 2000.
- [17]. A.P Steynberg, R.L Espinoza, B. Jager, A.C. Volsoo, "High temperature Syn-Gassynthesis in commercial practice," Applied Catalysis A: General 1999, 186, 41-54.
- [18]. S. Ouyang, M.Prevot, H. Surangalika, W. Yang, and R.S. Besser, Abstracts of the Materials "Experimental System to Study Catalysis in Micro-Geometry," Research Society Fall Meeting, 2000, MRS.
- [19]. Schwalbe, V.Autze, G. Wille, "Chemical Synthesis in Microreactors," Chimia, 2002, vol.56, pp. 636-646.
- [20]. IUPAC MANUAL IUPAC: Manual of symbols and terminology for physico-chemical quantities and units. Pure Appl. Chem. 1979, 51, 1-41.
- [21]. G. L.-T. Chiu and J. M. Shaw, Optical lithography: Introduction, Guest editors
- [22]. W. M. Moreau, Semiconductor Lithography, Plenum Publishing Co., New York, 1988.
- [23]. D. J. Elliott, Integrated Circuit Fabrication Technology, 2nd edition, McGraw-Hill Book Co., Inc., New York, 1989.

- [24]. L. F. Thompson, C. G. Willson, and M. J. Bowden, "Introduction to Microlithography" American Chemical Society 1983, Washington, DC.
- [25]. M.A. Reed and W. P. Kirk "Nanostructure Physics and Fabrication," Academic Press, 1989.
- [26]. C.L. Tien, A Majumdar and F.M. Gerner "Microscale Energy Transport," Taylor & Francis pub, 1998.
- [27]. http://dot.che.gatech.edu/henderson/introduction_to_electron_beam_lithography.htm.
- [28]. Thompson, Larry; Wilson, Grant; Bowden, Murrae; "Introduction to Microlithography," Second Edition, Oxford University Press, 1994.
- [29]. Deng, Qing. "Design, fabrication, and simulation of microreaction devices for the Louisiana Tech universal testing system" Thesis, Louisiana Tech University, 2000.
- [30]. <http://www.cfm.brown.edu/people/beskok/muflow.html>
- [31]. Kuttayan Annamalai, Microreactor "Design and Simulation in the Slip Flow Regime," Thesis, Louisiana Tech University 1999.
- [32]. C.S.Yih "Fluid Mechanics, a concise introductory to the theory" West River Press, Ann Arbor, Mich, 1988.
- [33]. G.K.Batchelo "Introduction to Fluid Dynamics," Cambridge University Press 1967
- [34]. Virginie MENGEAUD, "Design And Characterisation Of Basic Units For An Electrochemical Processing Plant At The Microscale," Ph.D Thesis, LEPA, 2003.
- [35]. <http://scienceworld.wolfram.com/physics/Navier-StokesEquations.html>
- [36]. Trebinski, R.; Wlodarczyk, E. "Application of S. K. Godunov's method for solving the problem of quasi-one-dimensional gas flow with a shock wave" Journal of Technical Physics (ISSN 0324-8313), 1983 vol. 24, no. 1, 1983, p. 105-120.
- [37]. Martin Rhodes, "Fluidization of Particles by Fluids," Monash University, Melbourne, Australia April, 2001.
- [38]. http://web.mit.edu/fluids-modules/www/basic_laws/1-7vorti.pdf
- [39]. John D Anderson," Computational Fluid Dynamics – The Basics with Applications," West Nyack, New York, USA: Cambridge Univ.

- [40]. D. Therriault, S.R. White, and J.A. Lewis, "Chaotic mixing in three-dimensional microvascular networks fabricated by direct-write assembly," *Nature Materials*, 2003, 2(4), pp. 265-271.
- [41]. <http://www.coventor.com/>
- [42]. Dhoble, A.V. and Zumbrunnen, D. A., "Controllable Morphology Development by Chaotic Advection in PP-LDPE Blends with a Smart Blender Prototype," ANTEC Vol. L, Chicago, Illinois, May 16-20. Society of Plastics Engineers, pp. 2803-2808, 2004.
- [43]. Wong, S. H., Bryant, P., Ward, M. and Wharton, C. (2003). "Investigation of mixing in a cross-shaped micromixer with static mixing elements for reaction kinetics studies," *Sensors and Actuators B*. (In Press).
- [44]. Gillespie, D J., "A general method for numerically simulating the stochastic time evolution of coupled chemical reaction," *comp Phys*. 22, 4.3-434.
- [45]. van Kampen, "Stochastic processes in physics and chemistry," 180-208 Elsevier, New York.
- [46]. Chin long Chiang, "An Introduction to stochastic processes and their application," Rober E Krieger Publishing Company, Hungtington, NY,1975.
- [47]. John G. Kemeny and J. Laurie Snell. "Finite markov chains," Princeton, N.J. : Van Nostrand, [c1960].
- [48]. <http://www.ece.gatech.edu/research/labs/vc/theory/photolith.html>
- [49]. Deepak Bose (Thermosciences Institute), T.R. Govindan, M. Meyyappan, "ICP Reactor Modeling: CF4 Discharges," (NASA Ames Research Center).
- [50]. A. E. Wendt, S.-B. Wang, "Modulated Discharges in Processing Applications," (Univ. of Wisconsin - Madison), J. Werking (SEMATECH).
- [51]. Soumitra R. Deshmukh, Dionisios G. Vlachos, "Microkinetic Modeling and CFD simulations," AIChE meeting, San Francisco, CA, Nov.16-21, 2003.
- [52]. F.L. Rmer and P.Schilp, German Patent DE 4241045, 1994.
- [53]. Hyongsok T. Soh, Kathryn Wilder Guarini, Calvin F. Quate "Scanning Probe Lithography," Imperial College Press; October 1999, ISBN: 1860941990.

- [54]. Gray B L, Jaeggi D, Mourlas N J, van Drie"enhuizen B P, Williams K R, Maluf N I and Kovacs G T "Novel interconnection technologies for integrated microfluidic systems," *Sensors Actuators A* 77 57–65 1999.
- [55]. D. Kuila, S. Zhao, V. S. Nagineni, A. Potluri, H. Indukuri, Y. Liang, W. Cao, J. Hu, J.Fang, K. Varahramyan, R. Nassar, J. Palmer, U. Siriwardane and S. Naidu "Microreactors for Catalysis using Nano-catalysts," Invited talk - presented at the 227th ACS National Meeting, Anaheim, CA, COLL 473, March 28 –April 1, 2004.
- [56]. D. Kuila, V.S.Nagineni, S. Zhao, H. Indukuri, Y. Liang, A. Potluri, U. Siriwardane, N.Seetala, and J. Fang "Characterization of Alumina and Silica Sol-Gel Encapsulated Fe/Co/Ru Nanocatalysts in Microchannel Microreactors for Fischer-Tropsch Synthesis of Higher Alaknes," *MRS Symposium in San Francisco*, April 13-16, 2004, O3.4, p303.
- [57]. D. Kuila.; V.S. Nagineni; S. Zhao; H. Indukuri; Y. Liang; A. Potluri; U. Siriwardane; N. Seetala; J. Fang. "Characterization of Alumina and Silica Sol-Gel Encapsulated Fe/Co/Ru Nanocatalysts in Microchannel Reactors for F-T Synthesis of Higher Alkanes," *MRS Proceedings 2004* in press.
- [58]. Akundi, M.A.; Zhang, J.; Gibbs, M.; *J IEEE Trans on Magnetics* 2002, 37, 2929.
- [59]. A.A. Belhekar, S.Ayyappan. and A.V. Ramaswamy, *J. Chem. Tech Biotechnol.*, 1994, 59,. 395.
- [60]. M.R. Sun-Kou, A. Mendioronz, J.L.G. Fierro, and J. M. Palacios, *Journal of Materials Science*, vol.30, P.496, 1995.
- [61]. Mi, X.-B. and Chwang, A.T. (2003), "Molecular dynamics simulations of nanochannel flows at low Reynolds numbers," *Molecules*, Vol. 8, pp. 193-206.
- [62]. Basset, A.B., "A Treatise on Hydrodynamics", Cambridge University Press, 1888.
- [63]. Robert W. Barber, Warrington, "Numerical Simulation of Low Reynolds Number Slip Flow Past a Confined Microsphere," Cheshire, WA4 4AD, UK Presented at the 23rd International Symposium on Rarefied Gas Dynamics, Whistler, Canada, 20-25 July 2002.
- [64]. <http://www.ecn.nl/biomassa/research/poly/ftsynthesis.en.html>
- [65]. <http://www.engineeringatboeing.com/fluids/equations.html>

- [66]. H. Scott Fogler "Elements of Chemical Reaction Engineering," (3rd ed.), Prentice Hall, Upper Saddle River, NJ (1998).
- [67]. Martin Chaplin and Christopher Bucke, "Enzyme Technology" Cambridge University Press, 1990.
- [68]. Jesse Fowler, Hyejin Moon, and Chang-Jin "CJ" Kim "Enhancement of mixing by droplet-based microfluidics," IEEE Conf. MEMS, Las Vegas, NV, Jan. 2002, pp. 97-100.
- [69]. White, F. M. (1994). Fluid Mechanics. McGraw-Hill, 3rd Edition.
- [70]. TeGrotenhuis WE, RJ Cameron, MG Butcher, PM Martin, and RS Wegeng. 1999. "Micro-Channel Devices for Efficient Contact of Liquids in Solvent Extraction." Separation Science and Technology 34(6-7):951-974.
- [71]. Mughis Naqvi and Chris Meyer Sulzer, "Gas-Gas Mixing Applied to SCR Systems," 2003 Conference on Selective Catalytic Reduction and Non-Catalytic Reduction for NOx Control October, 2003.
- [72]. http://www.engineeringtoolbox.com/21_623qframed.html
- [73]. André Bakker, Ahmad H. Haidari and Elizabeth M. Marshall, "Design Reactor Vias CFD," Fluent Inc. December 2000.